

2 Accelerator

2.1 Accelerator physics

2.1.1 Introduction

Energy Recovery Linacs (ERLs), proposed already in [1], have received much attention during the last decade because they have the potential to accelerate currents much larger than those of non-recovering Linacs and to provide emittances smaller than those in x-ray storage rings at similar energies and for similar beam currents. The first potential is due to the fact that the current in Linacs is limited by the available electric power if the energy of the accelerated particles is not recovered. In that case, accelerating a 100 mA beam to 5 GeV would require a beam power of 0.5 GW, which is technically not feasible. We therefore propose to use an ERL for these large currents of Linac quality beams. The second potential is due to the fact that the emittances in an ERL are those of the electron source if emittance increase during acceleration can be avoided. Once high-current, ultra-low-emittance electron sources become available, beams accelerated in an ERL will have a brightness significantly larger than that of high-energy storage rings.

Energy Recovery Linacs for x-ray light sources have particular challenges that are related to four properties of the beam they are to deliver: small transverse emittances, low energy spread, short bunches, and large currents. In this chapter, the design of the proposed ERL is explained and how it meets these particular challenges is discussed. It is shown that computer models of the accelerator indicate that the design parameters are suitably chosen, limiting emittance growth from Incoherent Synchrotron Radiation (ISR), Coherent Synchrotron Radiation (CSR) and other sources. The design also limits emittance growth from beam-breakup (BBU) and ion instabilities as well as keeping energy spread from short-range wakefields tolerable, collimating beam halo, and holding other detrimental effects in check.

Small transverse emittances

The design of an injector that would produce the required small emittances by overcoming destructive effects of the space-charge forces that dominate beam motion at low energy and high beam density is described, along with how the beam is to be accelerated to high energies with little emittance growth. At higher energy, space charge becomes less important, but deviations from a cylindrically-symmetric accelerating fields in a Linac, e.g. due to cavity misalignments and coupler kicks, can continue to increase the emittance and must therefore be limited. The accelerated beam is then sent through bends of the accelerator until it reaches the x-ray users. In these bends, emittance excitation from incoherent synchrotron radiation occurs, just as in storage rings, and we show how linear and nonlinear low-emittance-growth optics can limit this excitation. In storage rings, this leads to an equilibrium emittance after a few damping times, typically during several hundred revolutions. In an ERL, the horizontal

emittance can consequently be several hundred times smaller than in rings. In fact, it can become so small and the electron beam so narrow that it is nearly indistinguishable from a point source for hard x-rays, producing waves that are coherent in both transverse directions. The vertical emittance in a storage ring can already be made very small, sometimes even smaller than in an ERL. However, often this emittance is then smaller than required for a coherent hard x-ray beam so that the advantage of reducing the horizontal emittance in an ERL is much larger than that of further reduction in the vertical emittance.

Low energy spread

Bunches that are accelerated in a Linac can have a very low energy spread compared to a storage ring. The energy spread in a ring is due to the stochastic nature of synchrotron-radiation emission accumulated over hundreds of turns, as discussed for the horizontal emittance. In an ERL, however, the energy spread is determined by the bunch length because the accelerating field in a Linac changes with time over the duration of the bunch. An ERL's short bunch length produces low energy spread, and therefore low x-ray frequency spread, which allows longer undulators to be used more efficiently in an ERL than typical for a storage ring. However, short bunch length also increases wakefields and coherent synchrotron radiation. The presented design takes these effects into account.

Short bunches

The electron source of an ERL can produce bunches that are much shorter than those in storage rings. While this allows for time-resolved x-ray experiments, it also poses challenges for the beam dynamics; and those were taken into account for the presented design. For example, the strong wakefields that short bunches create can lead to an energy spread after deceleration too large for simple beam transport into the beam stop. A bunch compressor can further reduce the bunch length in an ERL significantly, and we therefore present a bunch compression at high energy that takes effects like CSR and nonlinear time-of-flight into account.

Large currents

Large currents of short bunches produce significant wakefield heating in all beam pipe components and excite Higher-Order Modes (HOMs) in the superconducting RF cavities. The ERL's cavities are designed with cooled HOM absorbers that reduce the quality factor of these modes sufficiently to avoid recirculative beam-breakup instabilities up to the desired current of 100 mA. Because large beam currents can produce large radiation background rates from beam-halo scraping or from component failures, a beam-abort and beam-collimation system is part of the presented ERL design.

State of the art

In Fig. 1.3.3 the spectral brightness and coherent fraction of the ERL have been compared to ring-based light sources, and in Tab. 1.3.1 the primary operating modes A) High Flux B) High Coherence and C) Short Pulse have been defined. Comparisons with state of the art storage rings are shown in Tab. 2.1.1.

Table 2.1.1: Electron beam parameters in the ERL's high-brightness and high-current modes as compared to leading storage rings for each parameter. The ERL furthermore has a mode for bunch durations as short as 100 fs described in Tab. 1.3.1.

Parameter	ERL	Ring	Ring name
Horizontal emittance ϵ_x	8 pm/30 pm	1 nm	PETRA-3
Vertical emittance ϵ_y	8 pm/30 pm	1.2 pm	Australian LS
Bunch duration σ_t	2 ps	16 ps	ESRF
Energy spread σ_δ	2×10^{-4}	1×10^{-3}	typical
Current I	25 mA/100 mA	500 mA	SPring-8

The fact that several of the ERL's critical beam parameters are comparable to those of the leading storage rings shows that many diagnostic techniques can be adopted from these rings, e.g. for high-precision transverse beam position stabilization, ultra-low emittance measurements, bunch length measurements, beam-loss measurements, etc. Other diagnostics techniques can be adopted from Linacs or from the JLAB-FEL, the only operating SRF ERL. At that accelerator, 9.2 mA have been accelerated in ERL mode and its Beam-Breakup (BBU) diagnostics, bunch-charge stabilization, electric field and amplitude stabilization can be adopted to Cornell's hard x-ray ERL.



Figure 2.1.1: The Cornell ERL on the campus map

2.1.2 Layout

The development of an ERL at Cornell presents unique opportunities. Cornell has significant infrastructure and an existing 5 GeV particle accelerator. Therefore, the ERL example makes as much use as possible of the existing facilities at the Wilson Synchrotron Laboratory, which include CESR, the CHESG G-line beamline, and the Wilson Lab building. Because the CESR components were designed to sustain 8 GeV electrons, this section can comprise part of the 5 GeV return arc of the ERL.

The location of Wilson Lab lies on a hillside between the Cornell campus and Cascadilla creek. The CESR tunnel is approximately 15 m below the athletic field to the north of this hillside. This terrain is used in the ERL design by having the accelerator housed mostly in an underground tunnel, while the x-ray beamline section is located outside the hill where a new x-ray science building is to be located.

The current design is shown in Fig. 2.1.1. The logic in choosing this design is discussed in the following section. The layout is divided into nine discrete sections, shown in Fig. 2.1.2, roughly in accordance with their function: The injector (IN) delivers a 15 MeV beam into Linac A (LA), which accelerates the beam 2.7 GeV. This beam feeds into Turnaround A (TA), which bends it around to connect to Linac B (LB). The beam is accelerated through LB to 5 GeV into the South Arc (SA) containing nine undulators, which connects to part of CESR (CE), which connects to the North Arc (NA) containing five more undulators. The NA connects back into LA, which decelerates the beam to 2.3 GeV, recovering 2.7 GeV. A demerging dipole separates this beam from the 2.7 GeV accelerating beam into TB. Thereafter a merging dipole combines this decelerating beam with the accelerating beam from TA and directs it into LB, where it is decelerated to 10 MeV, recovering 2.3 GeV. Finally the beam is sent to the Beam Stop (BS).

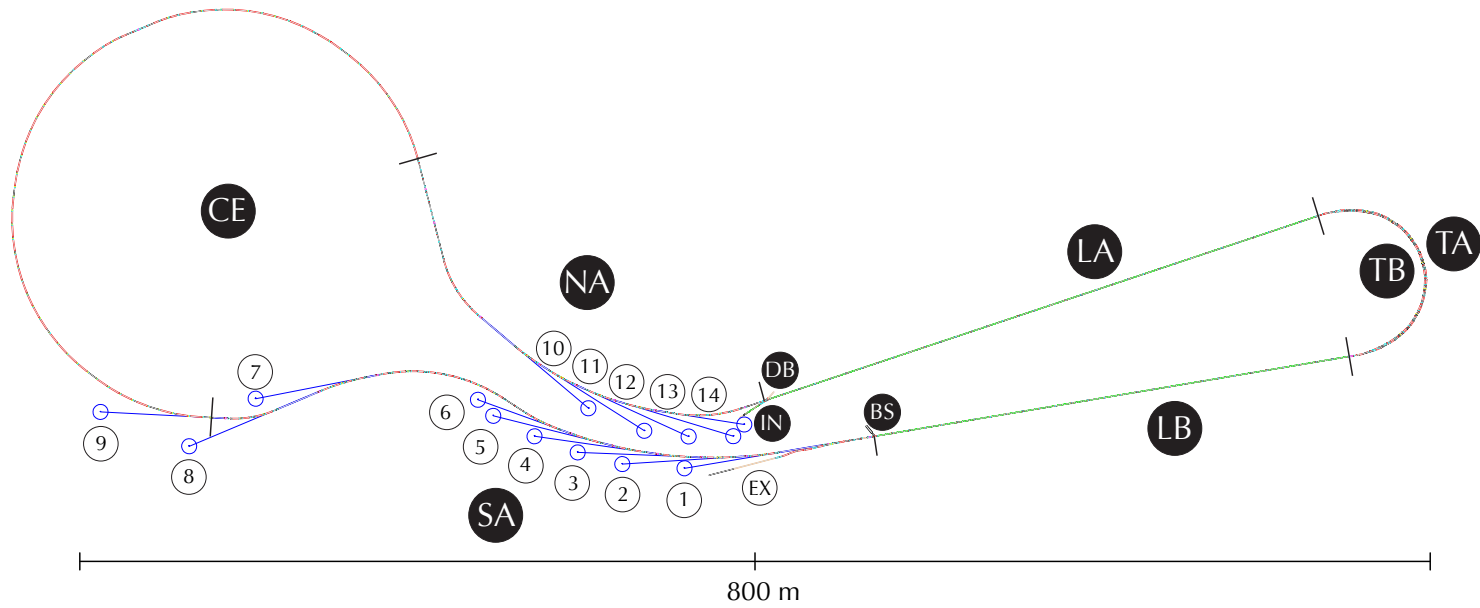


Figure 2.1.2: The ERL layout with section labels. A bunch is accelerated to 15 MeV in the injector (IN), and merged into the beginning of Linac A (LA), which accelerates it to 2.7 GeV. The bunch traverses Turnaround A (TA), and gains another 2.3 GeV through Linac B (LB). Now at 5 GeV, the bunch travels through undulators in the South Arc (SA), the CESR tunnel (CE), and undulators in the North Arc (NA). It then reenters LA off phase, which decelerates it to 2.3 GeV, enters Turnaround B (TB), and is decelerated to 10 MeV through LB. Finally it is extracted and sent to the beam stop (BS). To optimize the emittance out of the injector, a diagnostic beamline (DB) is used before the main Linac.

In order to be a competitive and cost-effective light source, the ERL must

- Utilize as much of CESR as possible.
- Provide at least 14 x-ray beamlines with easy access.
- Have a single building to house all x-ray beamlines outside of Wilson Lab, as well as the the injector.
- Accommodate at least two 25 m long undulators.
- Include the CHESS G-line beamline.

As mentioned, the natural extension of the ERL from CESR is to the east. Taking advantage of the curved hillside in this direction, the South Arc and the North Arc are shaped to conform to the terrain. The curvature is suitable for housing 70 m long x-ray beamlines with reasonably large experimental hutches. In this manner, beamlines from both arcs are housed in a single new x-ray science building. Furthermore, space has been allotted for three x-ray beamlines in Wilson lab, including G-line and one from a 25 m long undulator. The new building alone will contain up to eleven beamlines. Of these beamlines, up to six are from the South Arc and up to five from the North Arc, with each Arc containing one 25 m long undulator. The ERL design thus accommodates three 25 m undulators and eleven 5 m undulators.

The radius of curvature of the tunnel housing TA and TB is fixed at 40 m to limit the linear synchrotron-radiation-power density on the vacuum-chamber wall to not much above 1 kW/m. The bends and the beginning of the SA and the end of the NA are adjusted so that the two Linacs connect tangentially to the circular arc of the turnaround loop. The Linacs then have a relative angle of approximately 9° , and therefore TA and TB bend the beam by approximately 189° . The high-energy sections SA, CE, and NA bend the beam by approximately 125° , 253° , and 100° respectively, for a total of approximately 2.6π rad.

In the following, the design process is described using scaling laws for 9 critical performance values. If a preliminary design produces unreasonable values, it can be improved following the scaling laws. These are written with design parameters normalized to values of the ERL so that setting all fractions in parentheses to 1 leads to its critical performance values. It will be seen that these 9 values are all reasonable for the presented design.

In order to transport the beam through this geometry, the dipole magnets need to be of reasonable strength. Their fields scale as

$$B \approx 0.6 \text{ T} \left(\frac{28 \text{ m}}{\rho} \right) \left(\frac{\mathcal{E}}{5 \text{ GeV}} \right) \quad (2.1.1)$$

for a bending radius ρ and particle energy \mathcal{E} . This design has a reasonable field strength of no more than 0.6 T.

$$\Delta\mathcal{E}_{\text{ISR}} \approx -2.6 \text{ MeV} \left(\frac{\theta}{2.6\pi} \right) \left(\frac{28 \text{ m}}{\rho} \right) \left(\frac{\mathcal{E}}{5 \text{ GeV}} \right)^4 \quad \text{and} \quad (2.1.2)$$

$$\Delta\mathcal{E}_{\text{u}} \approx -2.1 \text{ MeV} \left(\frac{L_{\text{u}}}{130 \text{ m}} \right) \left(\frac{B_{\text{max}}}{1 \text{ T}} \right)^2 \left(\frac{\mathcal{E}}{5 \text{ GeV}} \right)^2 \quad (2.1.3)$$

show that for the total length L_u of undulators in the ERL, the energy loss during one pass is about 5 MeV when all undulators are turned on. With an energy of 15 MeV after the injector, the beam is stopped at 10 MeV, which we show to be a reasonable value.

Additionally, it has to be checked that coherent synchrotron radiation does not add a significant loss for a bunch charge Q and bunch duration σ_t . This loss is given by [2]

$$\Delta\mathcal{E}_{\text{CSR}} \approx -119 \text{ keV} \left(\frac{Q}{77 \text{ pC}} \right)^3 \left(\frac{\rho}{28 \text{ m}} \right)^{1/3} \left(\frac{2 \text{ ps}}{\sigma_t} \right)^{4/3} \left(\frac{\theta}{2.6 \pi} \right) \quad (2.1.4)$$

and with approximately 0.1 MeV per electron it clearly does not.

Furthermore, it has to be checked that the power deposition on the vacuum-chamber wall by ISR near dipole magnets is not too large,

$$\frac{dP}{dL} \approx 1.1 \text{ kW/m} \left(\frac{I}{100 \text{ mA}} \right) \left(\frac{28 \text{ m}}{\rho} \right)^2 \left(\frac{\mathcal{E}}{5 \text{ GeV}} \right)^4. \quad (2.1.5)$$

A linear power density of 1.1 kW/m is large but not untypical for storage rings.

Further, taking into account the vertical beam size, the maximum power per unit area on the vacuum-chamber wall near dipole magnets should be limited for a typical vertical beta function β_y and normalized vertical emittance $\epsilon_{N,y}$,

$$\frac{dP}{dA} \approx 37 \text{ W/mm}^2 \left(\frac{I}{100 \text{ mA}} \right) \left(\frac{28 \text{ m}}{\rho} \right)^2 \left(\frac{\mathcal{E}}{5 \text{ GeV}} \right)^{9/2} \sqrt{\frac{30 \text{ m} \cdot 0.3 \mu\text{m} \cdot \text{rad}}{\beta_y \epsilon_{N,y}}}, \quad (2.1.6)$$

and 37 W/mm² is a manageable value.

Preserving the low emittance of the injected bunches is of prime importance in the ERL. One source of emittance growth is emission of ISR, and the normalized emittance growth scales as

$$\Delta\epsilon_N \approx 0.034 \mu\text{m} \cdot \text{rad} \left(\frac{16}{N_b} \right)^3 \left(\frac{\theta_{\text{tot}}}{\pi} \right)^4 \left(\frac{28 \text{ m}}{\rho} \right) \left(\frac{\mathcal{E}}{5 \text{ GeV}} \right)^6 \quad (2.1.7)$$

where N_b is the number of bends in an arc with total angle θ_{tot} . This formula assumes close to ideal beam optics [3], and shows that the emittance growth during a full pass around the ERL can be less than the small emittance of the high-spectral-brightness mode B.

This ISR also increases the energy spread in the bunch, scaling as

$$\frac{\Delta\sigma_{\mathcal{E}}}{\mathcal{E}} \approx 3.7 \cdot 10^{-5} \left(\frac{\theta_{\text{tot}}}{2.6 \pi} \right)^{1/2} \left(\frac{28 \text{ m}}{\rho} \right) \left(\frac{\mathcal{E}}{5 \text{ GeV}} \right)^{5/2} \quad (2.1.8)$$

which is reasonably small for the ERL's design, and the beam's total energy spread of 2×10^{-4} . Note again that the 5 GeV sections SA, CE, and NA together bend the beam by an angle 2.6π .

However, the relative energy spread increases during deceleration but has to remain small enough to steer the full beam into the beam stop (BS). There, the ISR energy spread

$$\frac{\Delta\sigma_{\mathcal{E}}}{\mathcal{E}_{BS}} \approx 1.8 \cdot 10^{-2} \left(\frac{10 \text{ MeV}}{\mathcal{E}_{BS}} \right) \left(\frac{\theta_{\text{tot}}}{2.6 \pi} \right)^{1/2} \left(\frac{28 \text{ m}}{\rho} \right) \left(\frac{\mathcal{E}}{5 \text{ GeV}} \right)^{7/2} \quad (2.1.9)$$

is still only 1.8% and therefore reasonably small.

2.1.3 Optics overview

Linear optics-design criteria

In order to deliver a high-quality beam to the undulators and perform energy recovery, the optics in the ERL must overall

- Accommodate simultaneously accelerating and decelerating beams in the LA and LB sections.
- Accommodate one high-energy beam in the SA, CE, and NA sections.
- Limit radiative emittance growth as much as possible prior to undulators.

Since TA and TB maneuver the accelerating and decelerating beams separately, and the SA, CE, and NA sections only manage the high-energy beam, the only sections that must handle both beams are LA and LB, and the demerger and merger sections at the entrances and exits of the turnarounds. The optimization of these sections is challenging. Emittance growth occurs in every bending magnet due to the quantum nature of synchrotron radiation. It must be controlled everywhere, especially in TA and between the SA undulators. Unfortunately, the CESR magnet arrangement reused in CE does not admit a low-emittance solution, and therefore the emittance in the NA is relatively large compared to SA. For this reason, an upgrade option to CE is also given.

In order to provide the desired transverse beam size and length to undulators, the linear optics must provide

- Flexible time of flight terms r_{56} for each turnaround loop.
- $r_{56} = 0$ for the return arc (SA, CE, NA).
- Tunable r_{56} within some subsections.
- Flexible beta functions and zero dispersion in all undulators.
- Beta functions less than 200 m almost everywhere.

In general, the time of flight terms r_{56} for different sections and the phases of the accelerating cavities are used to manipulate the longitudinal phase space. In particular, r_{56} must be zero from the end of LB to the beginning in LA in order for the energy spread profile to correctly match the decelerating RF voltage and therefore allow full energy recovery. The beta functions in all undulators are flexible in order to satisfy the requirements of individual users of these devices. The dispersion is zero in undulators to avoid an apparent increase in beam size. As a rule of thumb, the beta functions are also kept below 200 m as much as possible to limit sensitivity to field errors in magnets, and it is generally advantageous to keep them small in dipoles in order to limit emittance growth from ISR.

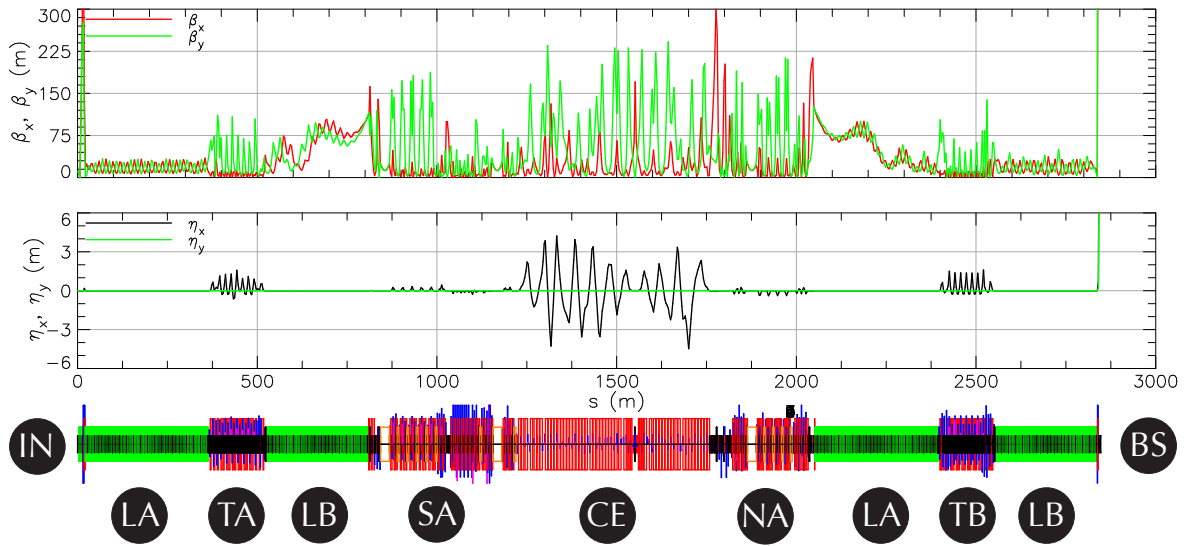


Figure 2.1.3: Linear optics for the full ERL, including the energy recovery pass.

Second-order optics-design criteria

For further refinement of the transverse beam size and of the bunch duration, the nonlinear optics must provide

- Zero second-order dispersion t_{566} in all undulators.
- Second-order achromatic sections, i.e. $t_{166} = 0$ and $t_{266} = 0$ from the beginning to end of each section.
- Flexible second-order time of flight term t_{566} in all sections (typically close to zero).

Similar to the first-order dispersion, the zero second-order dispersion in undulators avoids an apparent increase in beam size. As a rule of thumb, it is often easiest to control second-order dispersion when $t_{166} = 0$ and $t_{266} = 0$ for every subsection.

System optimization

The design and optimization of the ERL lattice is detailed through the following sections. Nearly all of the beam optics, with the notable exception of the injector in §2.1.4, are designed, simulated, and optimized using the Bmad and Tao software tools developed at Cornell [4]. The injector modeling has been performed using state-of-the-art 3D space-charge codes experimentally benchmarked as a part of Cornell ERL Phase 1a project [5].

The general strategy is to design first-order optics, including dispersion and time-of-flight, by optimizing the placement and strengths of dipole and quadrupole magnets section by section. Adjacent sections are spliced together by relaxing and matching Twiss parameters and dispersion functions. Second-order optics are manipulated by strategic placement of sextupole magnets, and further optimizing their fields.

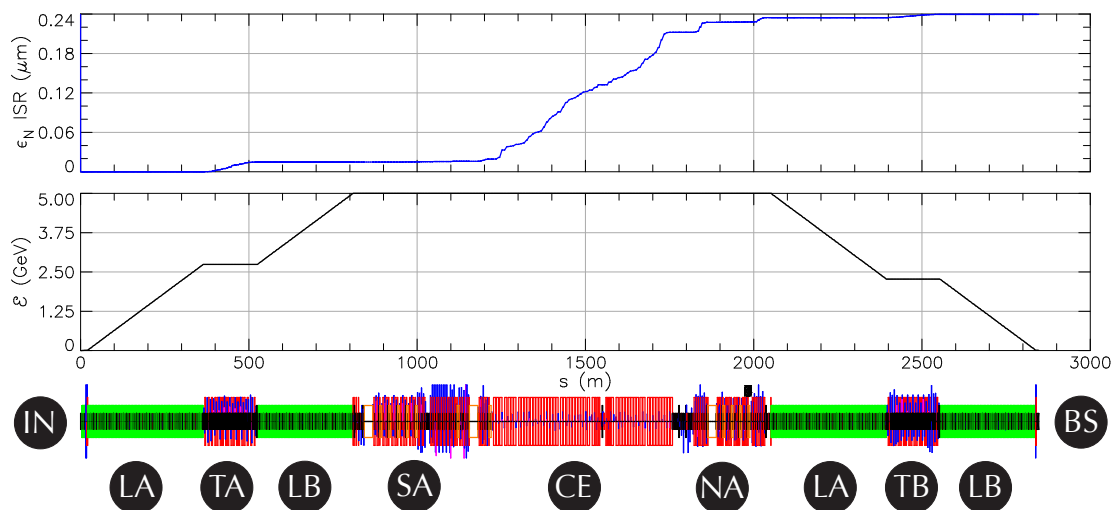


Figure 2.1.4: Emittance growth due to ISR, and the design energy \mathcal{E} , through the entire ERL.

The full linear optics for the ERL, including the second pass through the Linacs, are shown in Fig. 2.1.3. Emittance growth due to ISR, as well as the beam energy, are shown in Fig. 2.1.4. The relative energy spread is dominated by the accelerating RF curvature and remains at approximately 2×10^{-4} in the 5 GeV region.

2.1.4 Injector and merger (IN)

Design criteria

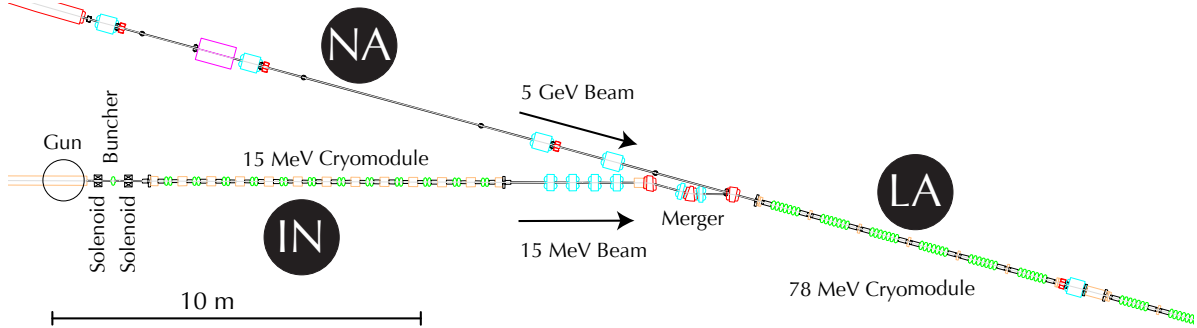


Figure 2.1.5: Layout for the injector section IN. The diagnostic beamline section DB, which mirrors the merger section, is not shown.

The injector section IN, described in technical details in §2.3, is a critical part of the ERL. It must

- Provide beams for all of the operating modes listed in Tab. 1.3.1.
- Have a layout that completely fits in the new building.
- Merge its 15 MeV beam with the returning 5 GeV beam.

The layout for IN is shown in Fig. 2.1.5.

Beam brightness from photoinjectors

In order to achieve high-brightness x rays, an injector of very low emittances is critical. Given the importance of the low-emittance beams, a considerable research and development effort in the accelerator community is presently devoted to the development and demonstration of both high average current (100 mA) and ultra-low emittance beams from the electron sources, photoinjectors in particular. Here we present the current understanding of the limiting factors to beam emittance and supporting simulations showing how the parameters suitable for the ERL x-ray source can be achieved using the photoinjector based on a high-voltage DC gun.

On a fundamental level, the maximum beam brightness and hence the smallest electron beam emittance is determined by the maximum accelerating field at the photocathode during the laser pulse illumination and the mean transverse energy (MTE) of the electrons leaving the surface of the cathode. In particular, for a laser pulse that assumes a pancake shape near the cathode, the minimum normalized rms emittance is given by [6]

$$\epsilon_n = \sqrt{\frac{3q \cdot \text{MTE}}{10\pi\epsilon_0 m c^2 E_{\text{cath}}}}, \text{ or } \epsilon_n(\mu\text{m}) = 0.145 \sqrt{\frac{q(\text{pC}) \cdot \text{MTE}(\text{eV})}{E_{\text{cath}}(\text{MV/m})}} \quad (2.1.10)$$

relating the charge per bunch q , cathode field E_{cath} , and mean transverse energy MTE of the photocathode (e.g., MTE ~ 1 eV for metal and ~ 0.1 eV for semiconductor negative electron affinity photocathodes). Using $E_{\text{cath}} = 5$ MV/m as typical for high-voltage DC guns, and MTE = 0.12 eV as measured for GaAs illuminated with 520 nm laser light [7], one finds that 0.2 μm rms normalized emittance should be achievable in principle for 77 pC/bunch operation.

Many practical matters must be addressed before the emittance can approach the limit given by Eq. (2.1.10). A very high degree of emittance space charge compensation needs to be realized [8], something which is achieved though a combination of appropriate electron beam optics and laser pulse shaping; geometric and chromatic aberrations need to be kept in check, particularly in the DC gun vicinity where the beam tends to occupy a large volume; time dependent effects of RF-focusing and RF input coupler kicks in accelerating structures need to be considered and their degrading effect on the beam emittance addressed. Much of the beam physics phenomena under consideration can be properly accounted for in detailed beam dynamics simulations using state-of-the-art space-charge codes. e.g. several 3D space-charge codes have been benchmarked with experimental data in the ERL photoinjector prototype and found to be in excellent agreement with the measurements [5]. We use the same numerical tools for the design of the ERL photoinjector.

To better understand the mechanisms of emittance growth, the problem has been divided into two largely independent parts:

- optimization of the high-voltage DC photoemission gun geometry followed by the straight section accelerating the beam to about 15 MeV.
- study of various merger design options and their evaluation for transport of an ultra-low emittance beam that is matched to the main Linac.

Presented below are 3D space-charge simulations of the baseline injector design as depicted in Fig. 2.1.5, taking the beam through one full cryomodule section of the main Linac to high enough energy (about 100 MeV), where the effects of the space charge on beam emittance become negligible.

Gun and injector optimizations

In this section, the results of multi-objective genetic algorithm optimizations are presented for the purpose of studying the optimal performance in a photoinjector that could be used for the ERL. The general layout of the accelerator under investigation is tested by Cornell's prototype ERL injector shown in Fig. 2.1.6 (up to the merger section). The injector layout for the full ERL is essentially that of the ERL prototype photoinjector, with 12 instead of 5 two-cell cavities: a DC photoemission gun followed by an RF buncher cavity positioned between the two solenoids; the SRF cryomodule hosting 12 2-cell SRF cavities, each capable of delivering up to 1.25 MeV of energy gain to the beam. Since the beam stays axially symmetric throughout the entire beamline (9.5 m), a faster 2D routine is used in this numerical study [9]. Some 24 parameters were varied in the multi-objective optimizer to map out the optimal front of injector performance following the work that introduced this method [10]. The parameters varied represent the strengths of magnetostatic elements and those of the RF cavities, their phases, as well as the shape of the laser pulse. One important innovation

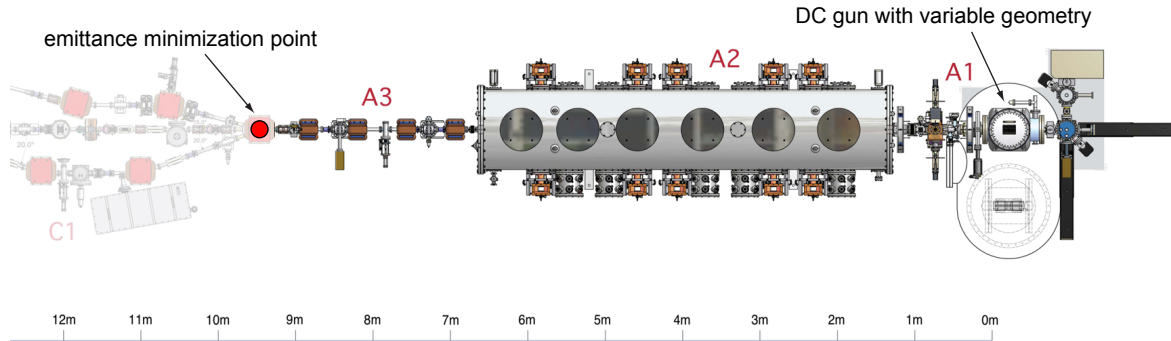


Figure 2.1.6: The layout of the straight section of the injector being optimized. The emittance minimization point is at 9.5m from the photocathode just prior to the entry into the merger. The quadrupoles magnets in A3 section are off. When the merger is included, these quadrupole magnets are used to match the beam through the dipole magnets into the main Linac.

is the introduction of the ability to adjust the DC gun geometry in the genetic algorithm optimizer, e.g. vary the electrode angle that introduces electrostatic focusing at the cathode or change the cathode-anode gap, see Fig. 2.1.7a. A realistic constraint on the maximum voltage vs. the shortest high-voltage gap distance in the gun is imposed following the empirical data obtained from a collection of measurements for large area electrodes as summarized in [11] and depicted in Fig. 2.1.7b. The salient feature of this empirical voltage breakdown condition is that there exists a trade-off between the largest achievable cathode gradient and the maximum gun voltage, both of which would ideally be present for low-emittance generation and preservation. Constraining the gun voltage to be below the empirical breakdown condition allows determination of an optimal and at the same time realistic operating gun point and geometry.

The emittance at the end of the beamline (9.5 m from the cathode) is presented in Fig. 2.1.8, which shows the smallest normalized rms emittance obtained vs. charge per bunch. Here the beamline is straight and the beam dynamics are cylindrically symmetric, so a 2D simulation is sufficient. The typical final energy is 13 MeV, and the final bunch is 3 ps rms (the initial laser pulse duration varies between 20 and 30 ps). Also, Fig. 2.1.8b shows the electric field inside the gun that corresponds to the optimum performance under the voltage breakdown condition (the corresponding gun voltage is about 500 kV). The importance of the photocathode mean transverse energy (MTE) is demonstrated in Fig. 2.1.8a: MTE = 500, 120, and 25 meV cases are plotted for comparison. Here we note that while the values of MTE = 120 meV have been measured for GaAs illuminated with a 520 nm laser [7], and a corresponding prompt response of less than 1 ps [7, 12], more recent advances in the understanding of thermal emittance formation mechanisms from Negative Electron Affinity (NEA) photocathodes have opened up the possibility of achieving sub-thermal MTE values together with a prompt photoemission response (as required for effective laser shaping) [13].

In summary, a realistic high-voltage DC gun in combination with a low thermal emittance photocathode is an excellent choice for delivering an ultralow emittance beam as required for

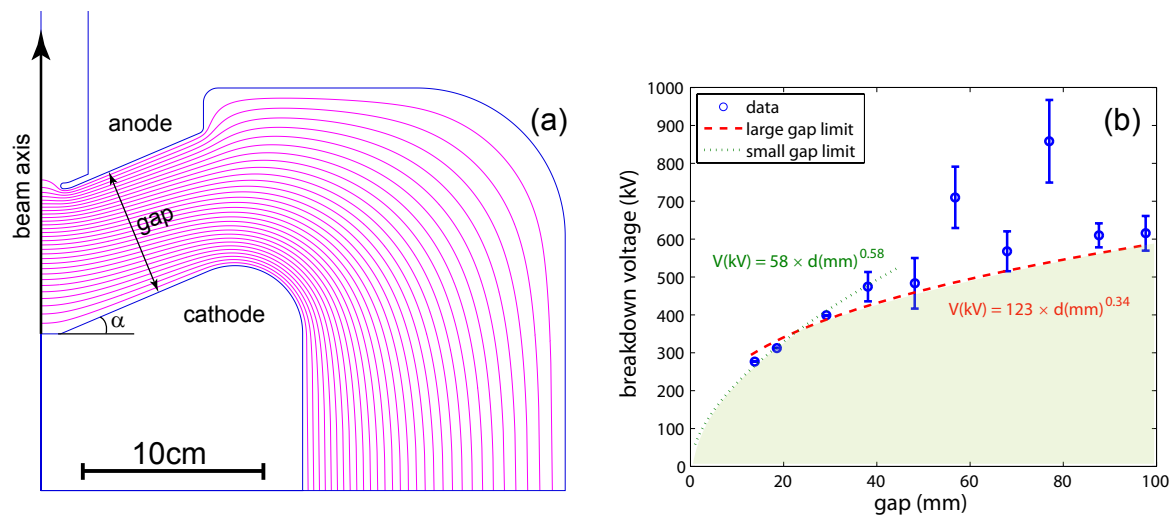


Figure 2.1.7: (a) Parameterized DC gun geometry with variable angle and gap. (b) Empirical voltage breakdown condition (adopted after [11]) used to constrain the gun voltage (the filled area under the curves designates the allowed values).

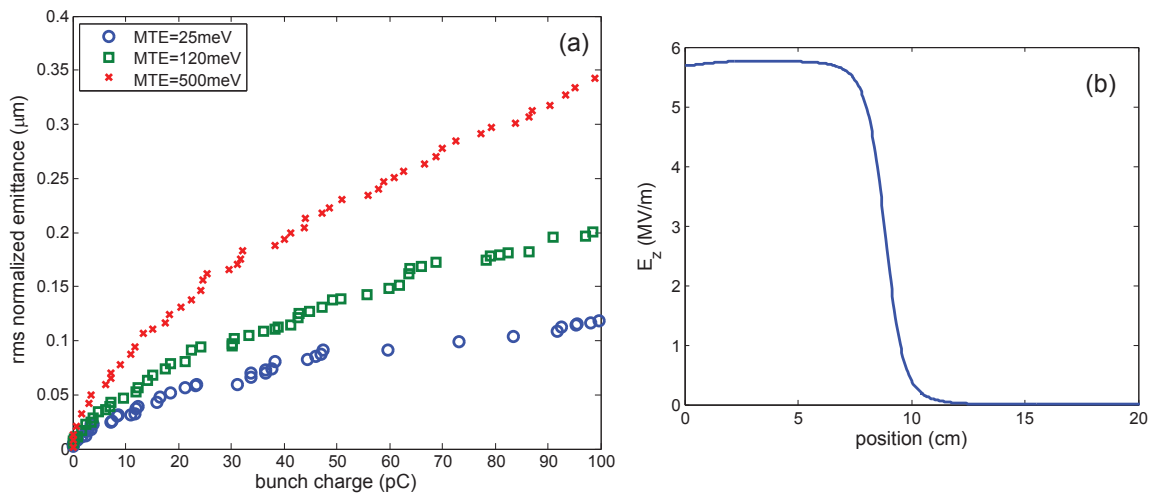


Figure 2.1.8: (a) Optimized 2D simulation results for beam emittance at the end of the straight section (9.5m from the photocathode) of the injector vs. the charge per bunch. The final beam energy is about 12 MeV and the rms bunch length is 3 ps. (b) Electric field inside the gun corresponding to these results. The gun voltage is 508 kV.

the ERL x-ray source. A new DC gun adopting the optimized geometry as well as a variable cathode-anode gap design to allow experimental exploration of the trade-off between gun voltage and electric field at the photocathode is now being constructed at Cornell University. We also remark that the emittance scaling with the bunch charge obtained in the simulations follows closely that of Eq. (2.1.10), deviating slightly mainly due to using of a longer laser

pulse at the photocathode. Fitting the results of Fig. 2.1.8a gives an emittance scaling with charge as $\propto q^\alpha$ where α is 0.5 – 0.6.

Merger studies

This section presents a comparison of different merger designs along with the evaluation of their performance. The importance of the merger section is due to the fact that the beam is not yet ultrarelativistic at this section, and therefore the space-charge forces inside this chromatic section can lead to emittance growth and thereby degrade the performance of the facility. Two merger cases have been considered: a 3-bend achromat similar to the one used in the Cornell ERL photoinjector prototype, and a ‘zig-zag’ merger [14]. Each merger employs 15° bends (with two 30° inside bends as required for the zig-zag design), see Fig. 2.1.9. For the purpose of direct comparison, the two merger types are made of equal length (2.55 m). A drift of the same length is included in the comparison to provide a baseline of the smallest emittance. The overall beamline consists of the merger followed by 5 SRF cavities of the main Linac taking the beam energy to about 80 MeV.

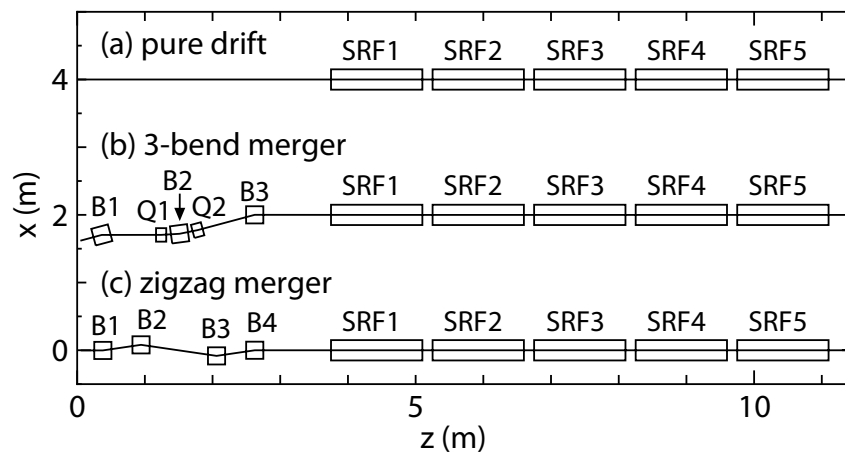


Figure 2.1.9: Merger types compared in simulations. Baseline case (a) with a simple drift, (b) 3-bend merger, and (c) zig-zag merger. The length of each merger is 2.55 m, followed by 5 SRF accelerating cavities.

The initial electron bunch is taken to be of a uniform cylindrical shape, with a given bunch length duration σ_t , energy spread $\sigma_\delta = 10^{-3}$, variable spot size, and divergence in both planes. The initial transverse emittance is set to zero (i.e. all divergence is correlated) to emphasize emittance growth caused by the merger proper.

Fig. 2.1.10a shows the effect of the space charge (80 pC/bunch) induced emittance growth for the case of the two mergers and the drift of identical length. The General Particle Tracer (GPT) code with improvements to the 3D space-charge routine [15] have been used for these simulations. Furthermore, the 3-bend merger case includes two options: quadrupoles set to the achromat condition that corresponds to the no-space-charge case, and adjustable quadrupoles that are used to minimize the emittance due to the space-charge induced beam

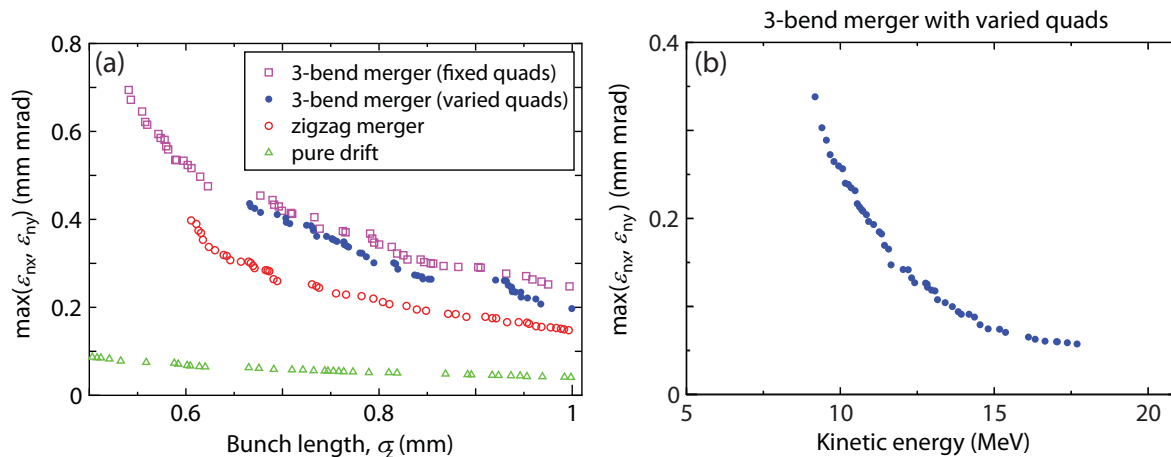


Figure 2.1.10: Merger performance in a 3D simulation with 80 pC bunch charge for (a) varied bunch length and fixed 10 MeV kinetic energy; (b) varied kinetic energy and fixed 0.9 mm rms bunch length.

envelope dispersion [16]. As anticipated, the zig-zag merger shows better emittance preservation characteristics. However, the 3-bend achromat is simplest to implement to merge very high-energy (5 GeV) beam with the injector low energy beamline, and as a result is more appealing from a practical point of view.

Whereas Fig. 2.1.10a shows the emittance growth for a fixed beam (kinetic) energy of 10 MeV going into the merger, Fig. 2.1.10b shows the 3-bend merger performance for different initial kinetic energy while the bunch length stays fixed (0.9 mm rms). It is seen that the emittance growth from the merger is less than $0.1 \mu\text{m}$ at 3 ps rms for 15 MeV beam and about twice that much for a 2 ps rms 80 pC bunch. This fact, along with the anticipated energy loss and induced energy spread in the 5 GeV ERL transport beamline, determined the choice of 15 MeV injector energy.

Another potential emittance-degrading mechanism in the merger is CSR. A new routine has been implemented in GPT to allow simulations of this effect [15] along with the 3D space charge. It was found, however, that the combination of charge per bunch, bunch duration, and beam energy in the ERL merger results in negligible CSR-induced emittance growth [17].

Simulated performance of the baseline design

To deliver 15 MeV energy to the beam, twelve 2-cell SRF cavities were chosen, each delivering (with some overhead) up to 150 kW to the beam. The baseline design includes a 4-quadrupole-telescope section following the injector cryomodule for matching the beam into the merger and the main Linac. Six 7-cell SRF cavities of the main Linac are included in the simulations (done with GPT) to account for the entire region of relevance for beam-emittance growth due to space-charge forces. See Fig. 2.1.5 for the baseline photoinjector layout.

The results of the transverse beam emittance at around 100 MeV beam energy are shown in Fig. 2.1.11 for 77 pC (100 mA average current) and 19 pC (25 mA average current). Gaps in the plots are due to the stochastic nature of the optimizer and limited number of generations.

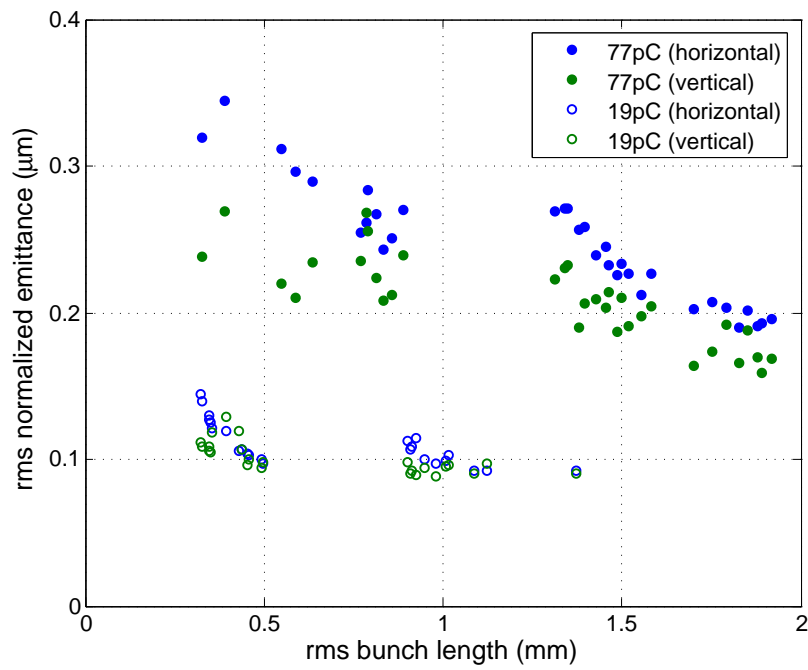


Figure 2.1.11: ERL baseline injector performance: rms normalized emittance at the end of the first cryomodule in the main Linac LA vs. the bunch length for two different bunch charges.

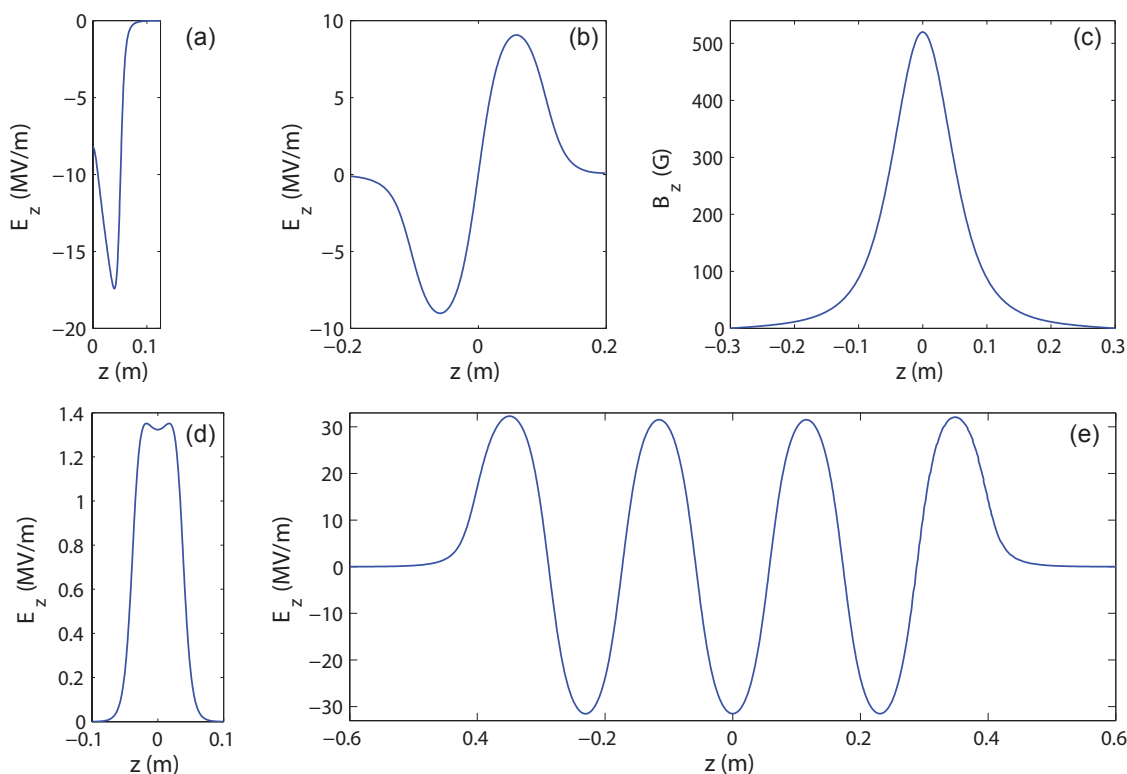


Figure 2.1.12: Typical on-axis fields from the field maps used to model the injector and first LA cryomodule: (a) high-voltage DC gun, (b) 2-cell SRF cavity, (c) solenoid, (d) RF bunching cavity, (e) 7-cell SRF cavity. The longitudinal scale is the same for all the field maps.

The simulations were done with 200,000 macroparticles using 3D field-maps for all elements in the injector section (IN). These injector simulations used a photocathode MTE of 25 meV [13].

Fig. 2.1.12 shows the field maps used in the simulation of the injector. The gun geometry used in these simulations corresponds to the presently operating Cornell gun, and the gun voltage is set at 750 kV. The more recent results presented in a previous §2.1.4 have not yet been included in the optimization of the baseline design, although the cathode field, which is the primary reason for the smallest possible laser spot size (and beam emittance), is comparable in the two cases. (The stronger electrode focusing in the present Cornell gun design leads to about a factor of 2 smaller field at the photocathode than the maximum on-axis electric field in the cathode-anode gap). The newly optimized gun geometry in Fig. 2.1.8b has a field on the cathode for 500 kV that is similar to the field in today’s gun for 750 kV. The new gun should therefore perform similar to simulations of today’s gun at 750 kV.

Fig. 2.1.14 demonstrates the beam envelopes that corresponds to the 77 pC/bunch case with 2.1 ps rms final bunch duration. The transverse phase space at about 90 MeV is shown in Fig. 2.1.13. Overall, we observe that the final minimum emittance is consistent with the

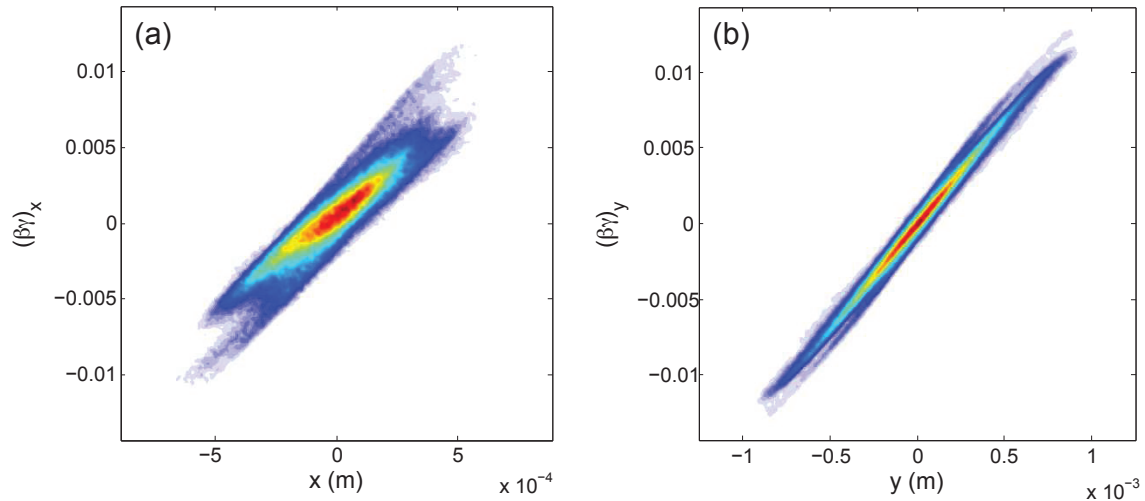


Figure 2.1.13: Computed (a) horizontal and (b) vertical phase space of the beam. Beam emittances are as following: 100% beam $\epsilon_{nx,y}(100\%) = 0.28, 24 \mu\text{m}$, 90% beam $\epsilon_{nx,y}(90\%) = 0.19, 0.16 \mu\text{m}$, beam core fraction $\xi_{x,y} \approx 70\%$ and core emittance $\epsilon_{nx,y,\text{core}} = 0.12, 0.09 \mu\text{m}$ [6].

contributions described in the previous two subsections.

The baseline design of the photoinjector continues to evolve towards obtaining lower beam emittances. Several obvious extensions to the present work are:

- use a higher energy out of the photoinjector to minimize the emittance growth in the merger section. This is particularly relevant for 25 mA operation since the cavity gradients and the RF power in the injector cryomodule are moderate in this case.
- explore an option of using a slightly longer bunch with lower transverse emittance out of the injector and perform energy spread compression [18] in the split Linac and the 2.7 GeV turn-around arc.
- develop a new merger of practical layout configuration and superior emittance preservation characteristics to the present 3-bend merger.

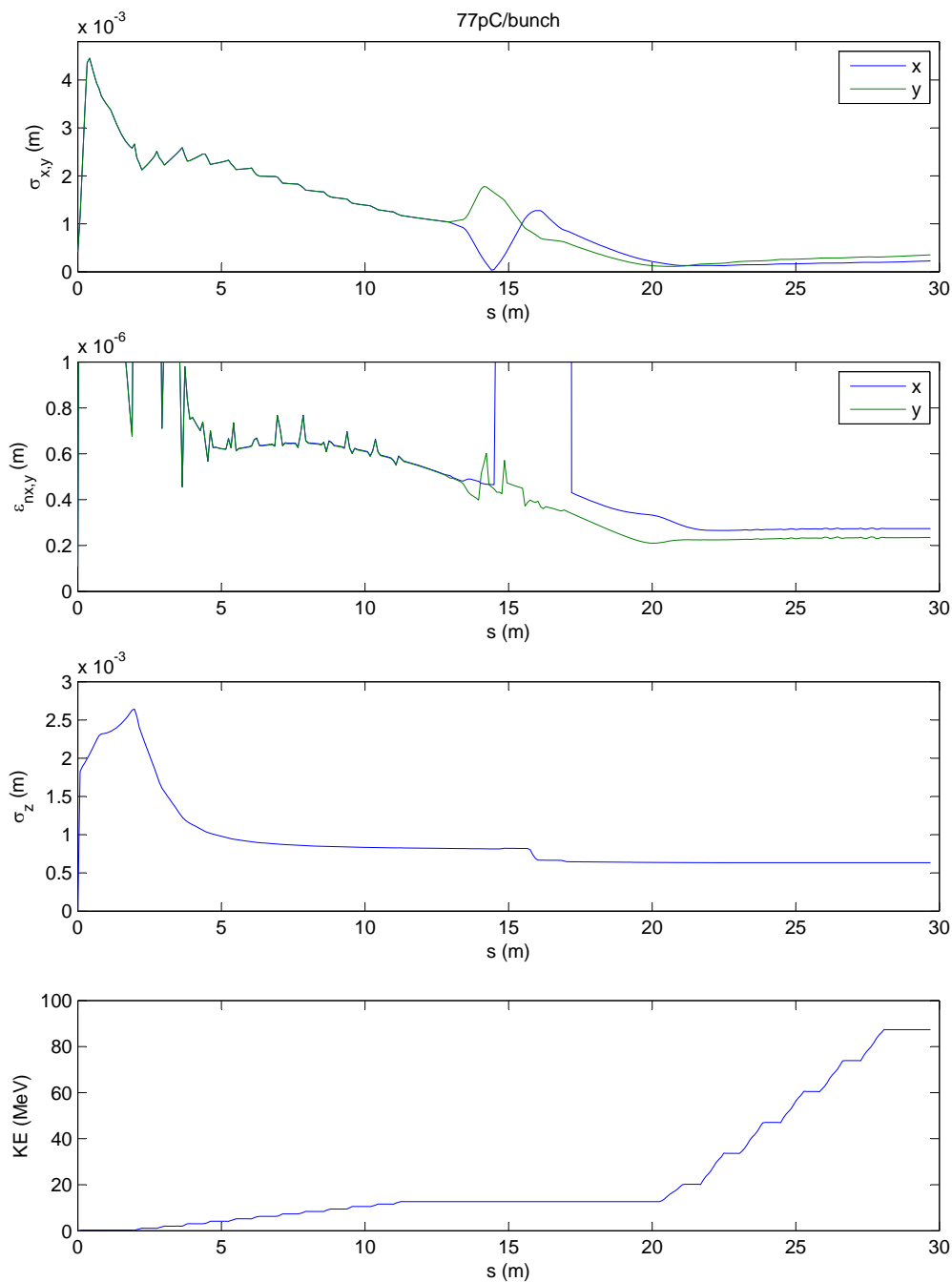


Figure 2.1.14: Rms beam sizes, emittances, bunch length, and kinetic energy in the injector section (IN) through the first cryomodule of the main Linac (LA). The final rms bunch duration $\sigma_t = 2.1$ ps, transverse rms normalized emittances $\epsilon_{nx,y} = 0.28, 0.24 \mu\text{m}$, and longitudinal rms emittance $\epsilon_{nz} = 31$ keV-ps.

2.1.5 Main Linac (LA & LB)

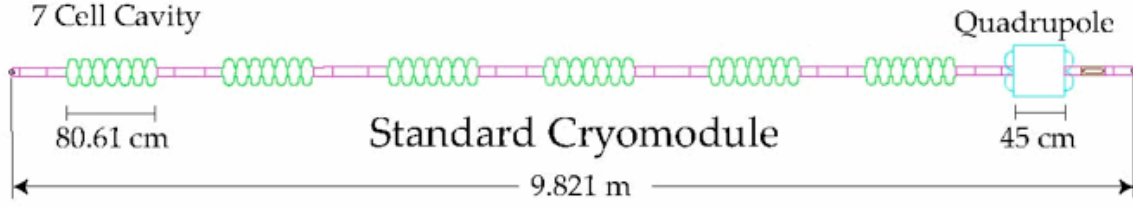


Figure 2.1.15: Layout of the ERL cryomodule with 6 SRF cavities, each having 7 cells, and a superconducting quadrupole and corrector package.

The ERL Linacs consist of 64 identical cryomodule cells divided among LA and LB, with the layout for the standard ERL cryomodule shown in Fig. 2.1.15. Each cryomodule contains six superconducting accelerating cavities and a superconducting-magnet package with a quadrupole and two steering coils, along with other elements, e.g. higher-order mode absorbers, gate valves, and beam position monitors, which can be considered to be drifts for purposes of the beam optics. Using the dimensions in the standard ERL cryomodule, in order to bring a 15 MeV beam to 5 GeV, each cavity must provide an average energy gradient of 16.1 MeV/m and therefore a single cryomodule can give or take 78 MeV to or from a beam.

Because the ERL has two turnaround loops TA and TB operating at different energies, one Linac needs to be longer than the other. In general, for N_A and N_B standard cryomodules in LA and LB, respectively, the changes in energy of the beam in these Linacs are

$$\Delta\mathcal{E}_{LA} = \frac{N_A}{N_A + N_B} (\mathcal{E}_{\max} - \mathcal{E}_{\min}) \quad (2.1.11)$$

$$\Delta\mathcal{E}_{LB} = \mathcal{E}_{\max} - \mathcal{E}_{\min} - \Delta\mathcal{E}_{LA} \quad (2.1.12)$$

where \mathcal{E}_{\min} is the injection energy and \mathcal{E}_{\max} is the full operating energy. For $N_A = 35$ and $N_B = 29$, with energies $\mathcal{E}_{\min} = 15$ MeV and $\mathcal{E}_{\max} = 5$ GeV, we get $\Delta\mathcal{E}_{LA} = 2726.17$ MeV and $\Delta\mathcal{E}_{LB} = 2258.83$ MeV. The beam in TA therefore has an energy of 2741.17 MeV and the beam in TB has an energy of 2268.82 MeV (accounting for a 5 MeV loss in the return arc due to ISR). These will often be abbreviated as 2.7 GeV and 2.3 GeV, respectively.

The beam optics in the Linacs must

- Have zero dispersion.
- Keep beta functions as small as possible for both accelerating and decelerating beams.
- Accept Twiss parameters from the IN for LA.
- Provide the correct Twiss parameters for the BS from LB.

The adjacent sections provide zero dispersion to LA and LB, and because there are no bends (other than corrector coils) within the Linacs there is no creation of dispersion. The beta functions are manipulated by the 35 and 29 quadrupole magnets in LA and LB, respectively.

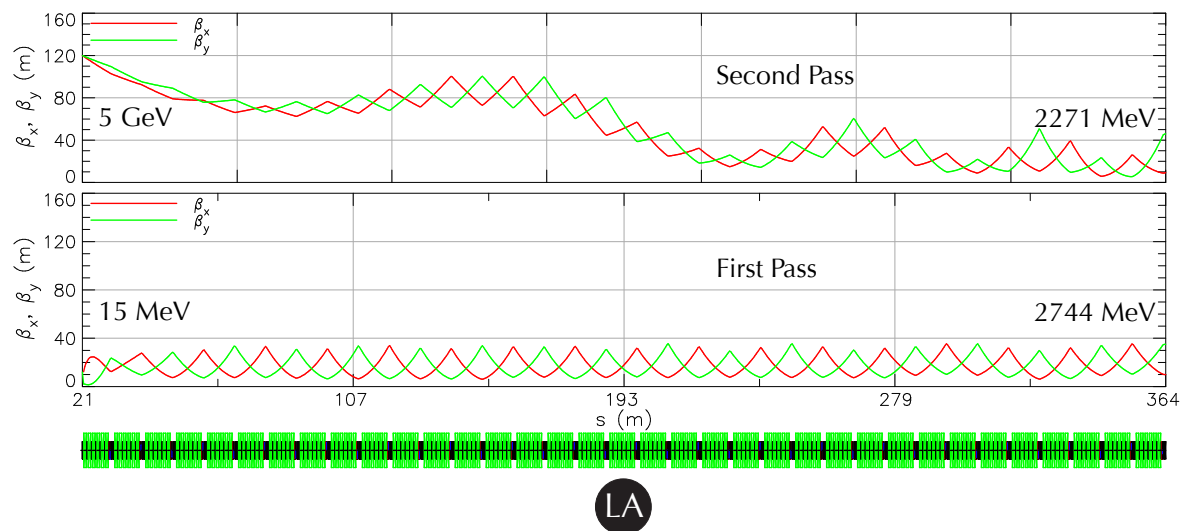


Figure 2.1.16: Beta functions for the first pass (accelerating) beam and energy recovery (decelerating) beam in LA. The optimization criteria are to keep the beta functions as small as possible and to match the low energy beam at $s = 0$ to the Twiss parameters from the IN. It has been found to be efficient to optimize by propagating the beta functions ‘backwards’ from the end of LA by varying β_x and β_y there along with the 35 quadrupole fields.

System optimization

Some optics guidelines for ERL Linacs are discussed in [19] and [20]. The main difficulty in optimization of the beta functions in the Linacs is due to the presence of two beams of different energies. The quadrupole strengths k seen by the two beams are inversely proportional to their reference momenta P , as in

$$k_a = \frac{P_a}{P_d} k_d, \quad (2.1.13)$$

in which the subscripts a and d denote the decelerating and accelerating beams, respectively. For example, in the first quadrupole magnet in the first cryomodule of LA, where the accelerating beam is at $(15 + 78)$ MeV and the decelerating beam is at $(4995 - 78)$ MeV, we have the quadrupole strengths $k_d \approx k_a/53$. Cryomodules are arranged in the opposite orientation in LB, so the quadrupole strength immediately prior to the BS section has the same ratio. Both beams have nearly equal energies around the 32nd quadrupole of LA. Because quadrupole gradients at the beginning of LA and end of LB must be weak enough so as to not over-focus the low energy beam, it becomes difficult for them to focus the high-energy beam.

The results of optimizing the beta functions for the first pass (accelerating) beam and energy recovery (decelerating) beam in LA are shown in Fig. 2.1.16. There it is seen that as the beams approach similar energies, the beta functions become more similar. Likewise, where the beam energies are the most different, so are the beta functions. There is no known rule for finding good solutions in this situation, though in practice it has been found that alternating positive and negative quadrupole strengths similar to a FODO lattice gives a good starting point.

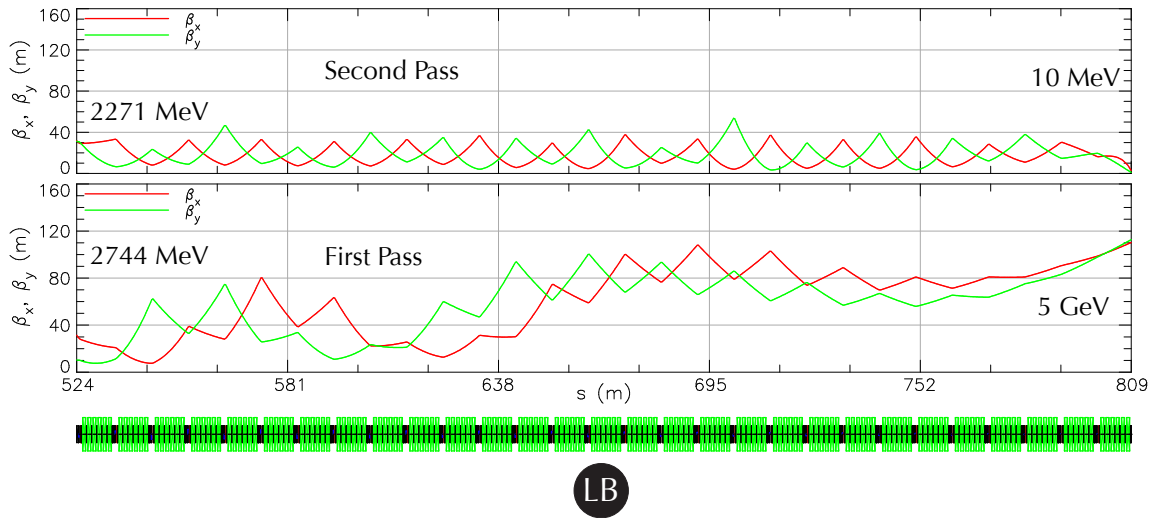


Figure 2.1.17: Beta functions for the first pass (accelerating) beam and energy recovery (decelerating) beam in LB. Optimization is similar to that in LA described in Fig. 2.1.16.

In this solution, we see that the beginning of LA for the first pass beam has very regularly focusing and defocusing beta functions, while the beta functions for the high-energy beam behave similarly to those in a long drift. The optics for LB are shown in Fig. 2.1.17. It is optimized in the same way as LA.

The relative effectiveness of quadrupole magnets on the different beams happens to be a virtue for matching from the IN and to the BS, because quadrupole fields near those sections can be tuned for the low energy beam with little effect on the high-energy beam. Therefore matching from the IN and to the BS is relatively simple compared to the overall optimization. In particular, the Twiss parameters for the first pass beam are matched near the end of the first cryomodule, because space-charge calculations in the IN include the first few cavities in

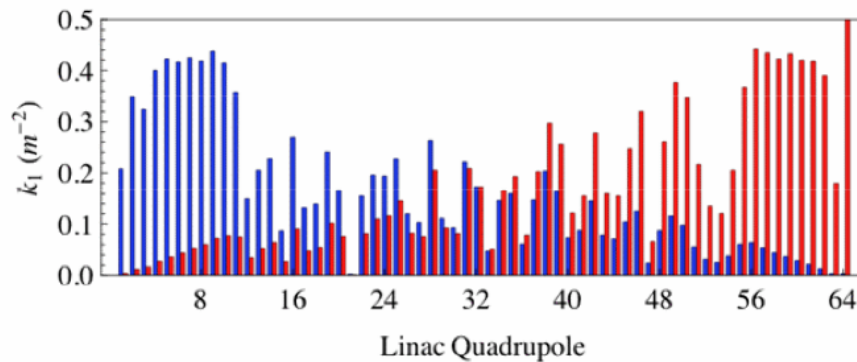


Figure 2.1.18: Quadrupole k_1 strengths seen by the accelerating beam (blue bars) and decelerating beam (red bars) in the Linacs.

LA and fix those values. The resulting quadrupole strengths seen by each beam are shown in Fig. 2.1.18.

2.1.6 Turn-Around loops (TA & TB)

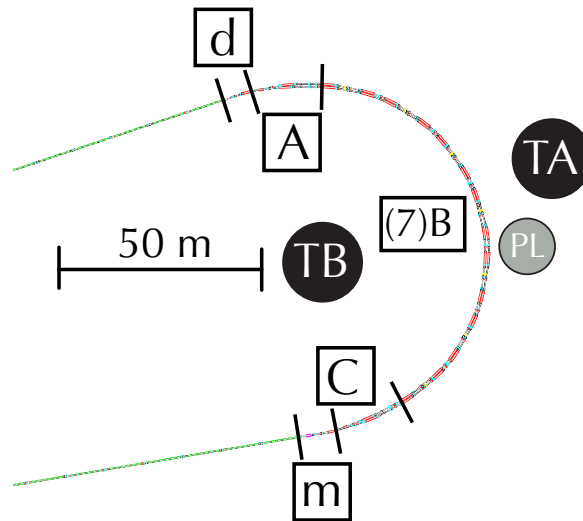


Figure 2.1.19: Layout for TA and TB with cell divisions. PL indicates the path length adjuster section. The demerger and merger section are indicated as d and m, respectively.

Design criteria

Two turnaround arcs provide an additional level of flexibility in the optics relative to single turnarounds in previous designs. In particular, having two turnarounds allows for the compensation of wakefields by tuning time of flight terms, a scheme that reduces the energy spread by up to 80% as described in [21]. This is important because the correlated relative energy spread from wakes at high energy becomes 500 times larger after deceleration and can potentially lead to particle loss before the beam stop.

First pass particles exit LA at 2.7 GeV, and follow TA. The second pass particles exit LA at 2.3 GeV, and follow TB. These sections must

- Demerge first and second pass beams from LA into TA and TB, respectively.
- Have variable r_{56} , close to 0, for both TA and TB.
- Have variable t_{566} , close to 0, for both TA and TB.
- Have the lowest possible radiative emittance growth for TA. Emittance growth is less critical for TB.
- Incorporate a path length adjustment section in TA.
- Keep beta functions as small as possible everywhere.
- Merge TA and TB beams for transport into LB.

Because the accelerating (first pass) and decelerating (second pass) beams enter the turnaround region at different energies, they can be separated by a dipole magnet. The radiative emittance growth must be limited so as not to spoil the excellent emittance bunches prior to acceleration by LB. In order to have the first and second pass bunches arrive in synchrony with LB, the path lengths of TA and TB must differ by an integer number of wavelengths λ_{rf} . Like many sections, the beta functions are kept as small as possible to minimize the effects of alignment errors. Finally, the beams must be rejoined for entry into LB.

System optimization

To achieve these criteria, both TA and TB are divided into five types:

Demerger Separates the first and second pass beams exiting LA. Contains two quadrupole magnets seen by both beams, and a demerging dipole magnet

Cell A Matches Twiss parameters from the demerger section into the appropriate cell B section

Cell B Roughly periodic section containing two dipole magnets and four quadrupole magnets
– occurs seven times

Cell C Matches Twiss parameters from the last cell B into the merging section

Merger Joins the beams in TA and TB to enter LB. Similar to the demerger section in reverse

These sections are shown in Fig. 2.1.19. In the demerging section, the demerging dipole has a 0.6 T magnetic field and is 2 m long. This separates the beams by 26 mm at the magnet's exit end with a relative angle of 27 mrad. Some detail of this section is shown in Fig. 2.1.20. A septum bend aids in the separation of the TB beam.

The bulk of TA (and similarly TB) is built out of cell B sections. For an initial optics solution, a single cell B is highly optimized to provide small periodic beta functions, small radiation integral, and zero r_{56} by varying the four quadrupole strengths. The demerging section, of cell A type for both turnarounds, and the first sections of cell B type for both turnarounds are optimized simultaneously to match into these periodic optics. The cell C and merger sections are similarly optimized.

The resulting linear optics of TA and TB are shown in Fig. 2.1.21 and Fig. 2.1.22. Here the TB optics are very periodic, but the TA optics are slightly irregular. This is because the path length adjustment section, detailed in Fig. 2.1.23, is extended by approximately 10 cm from its normal position, which breaks the symmetry in the optics.

The radiative emittance growth and time of flight terms for TA are shown in Fig. 2.1.24. Here it is seen that the first and second-order dispersion have been manipulated to make both arcs isochronous and achromatic to second-order with the aid of seven sextupole magnets in each arc. This emittance growth for TA accounts for roughly 13% of the mode B emittance in Tab. 1.3.1. The plot for TB is similar, and not shown.

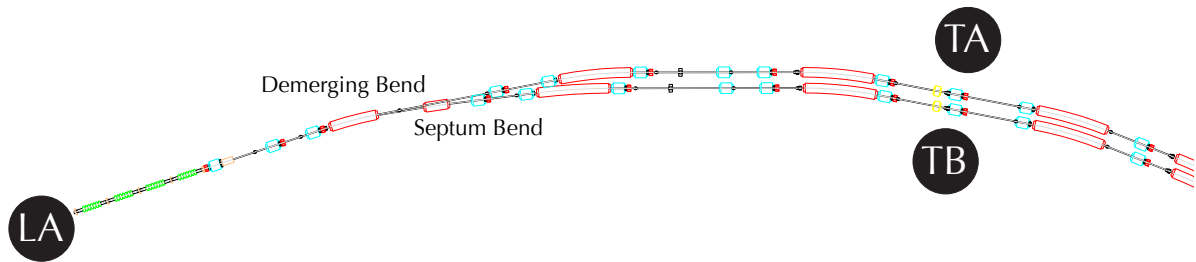


Figure 2.1.20: Demerger section for TA and TB. The merger section downstream is similar.

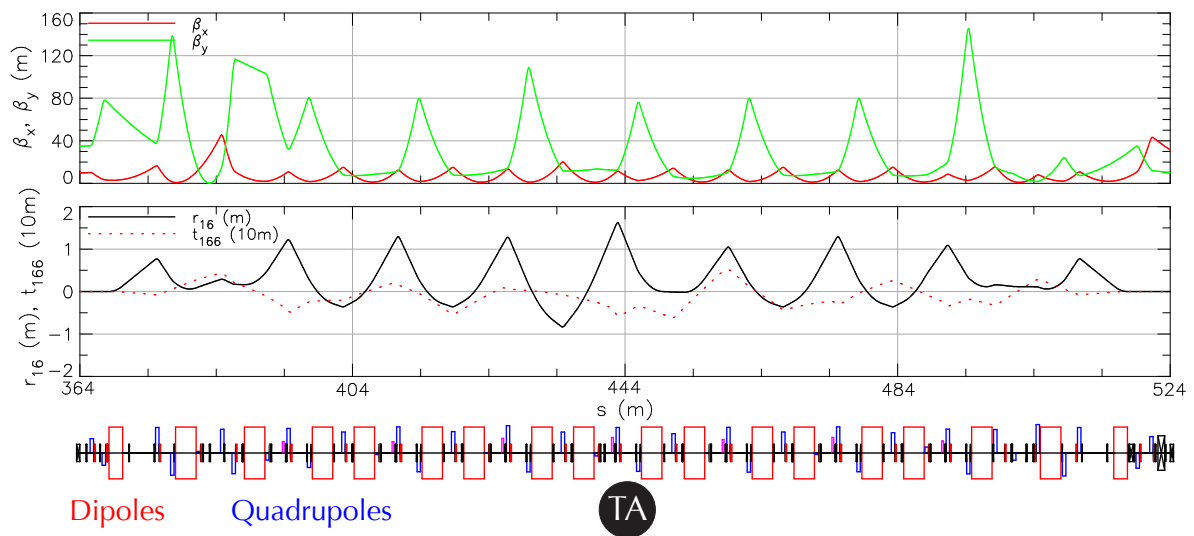


Figure 2.1.21: Linear optics for TA, with second-order dispersion.

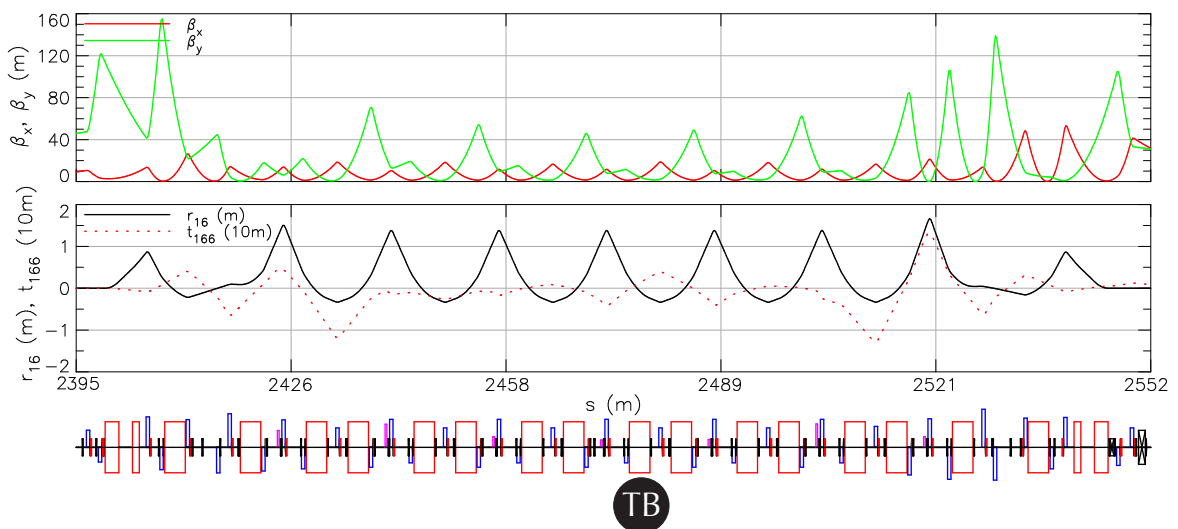


Figure 2.1.22: Linear optics for TB, with second-order dispersion.

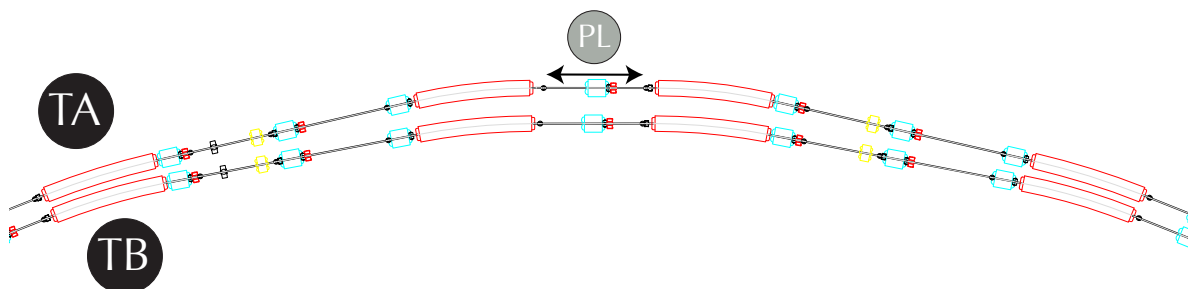


Figure 2.1.23: Path Length adjuster subsection of TA. These four dipoles have variable strength to be able to extend or contract the arrowed section by 10 cm.

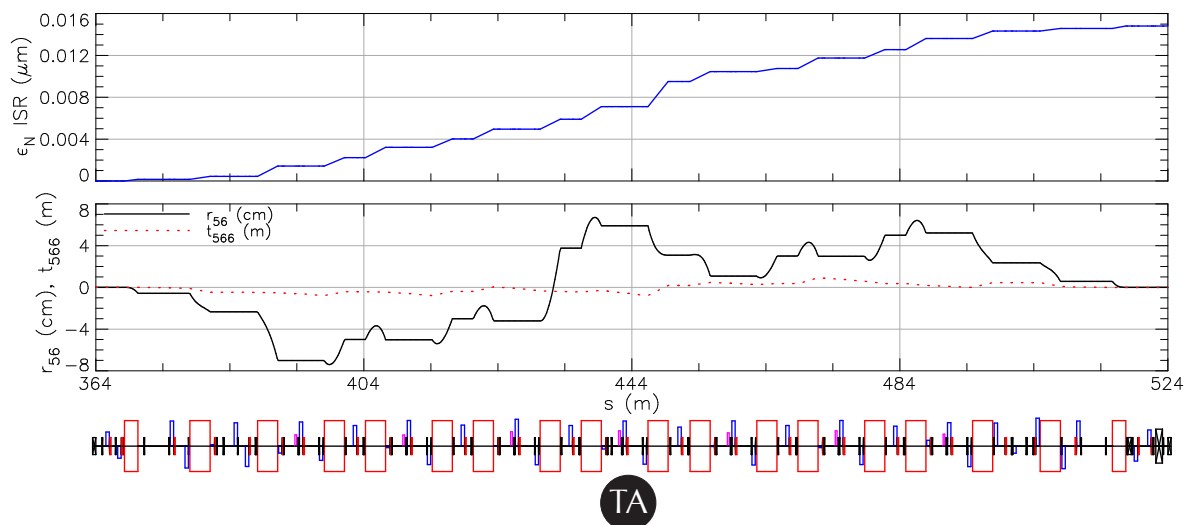


Figure 2.1.24: Normalized emittance growth due to incoherent synchrotron radiation, and time of flight terms r_{56} and t_{566} for TA.

2.1.7 South Arc (SA)

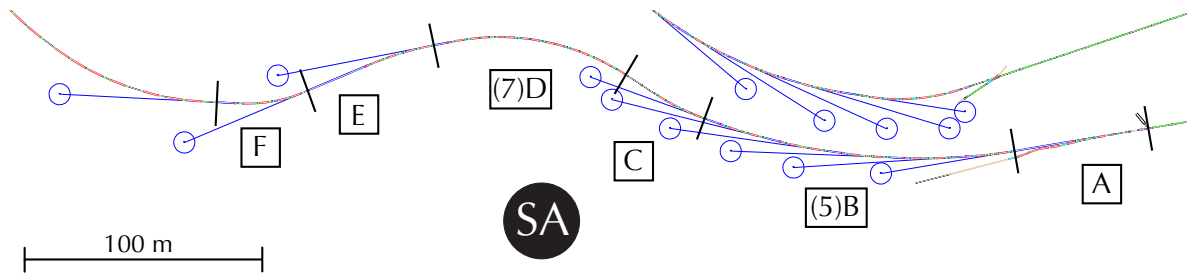


Figure 2.1.25: Layout showing the SA section. The different cell sections are labeled in boxes. For example, (5)B indicates five instances of cell B sections in a row.

Design criteria

The SA contains the first undulators in the ERL that receive the 5 GeV beam. This section must

- Receive the 5 GeV beam from the exit of LB.
- Contain six undulators in the new building, including one that is 25 m long.
- Provide two new undulators in Wilson Laboratory, as well as the G-line undulator.
- Allow for the extraction of the beam to the EX section.
- Collimate the beam halo prior to the first undulator.
- Minimize emittance growth throughout.
- Provide customized beam sizes with zero dispersion in all undulators.
- Control first and second-order time of flight terms r_{56} and t_{566} .

This section lies partially in a new building, and partially in the existing Wilson Laboratory. The new building will also house an extracted beamline EX for accelerator physics studies, and the SA section must provide space for such extraction. Because there are undulators throughout the entire section, emittance growth must be controlled everywhere. Additionally, in order to limit the amount of time of flight term r_{56} contributed by CE and NA in order to make the return arc (SA, CE, NA) isochronous, the r_{56} term for the SA must also be kept as small as possible. Finally, the t_{566} term must be controlled for the bunch compression mode.

System optimization

The SA section, shown in Fig. 2.1.25, is approximately 410 m long and contains the majority of undulators in the ERL. It is the first section after the beam has been accelerated to 5 GeV by LB, and therefore receives bunches with the lowest possible emittance. It is divided into six section types:

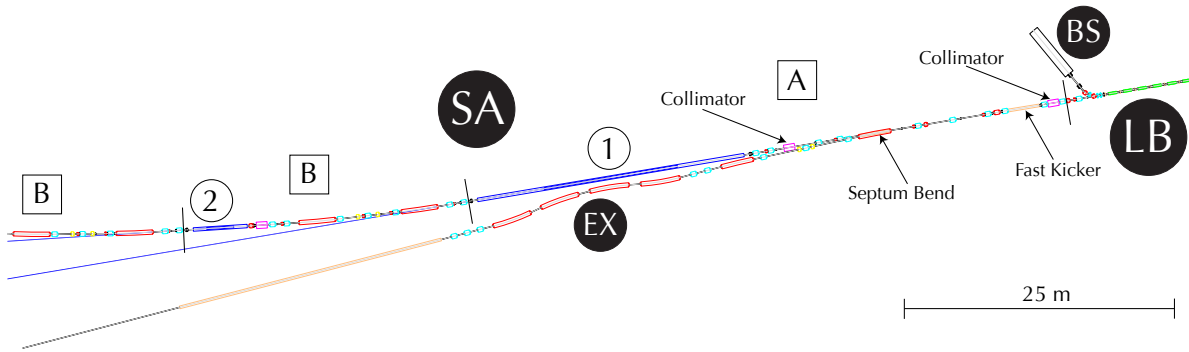


Figure 2.1.26: The layout for the beginning of the SA section, showing cell A with the long undulator and the first cell B sections. Undulator numbers 1 and 2 are indicated in circles. The beam moves from the right at LB to the left. The EX section is described in §2.1.12.

Cell A Matches Twiss parameters from LB into the first 25 m long undulator.

Cell B Periodic section containing a 5 m undulator and a two-bend achromatic section – occurs five times.

Cell C Matches Twiss parameters from the last cell B into the first cell D.

Cell D Periodic section consisting of a two-bend achromat for beam transport, with the last cell containing a 5 m long undulator – occurs seven times.

Cell E Matches Twiss parameters from the last cell D into a 25 m long undulator.

Cell F Matches Twiss parameters from cell E into the G-line undulator just prior to the CE section.

The layout for the beginning of the SA is shown in Fig. 2.1.26 with cell A and the first two cell B sections. There are three bends following the BS demerger magnet that compensate for dispersion and provide a net angle of approximately 1 mrad to protect users of the first undulator from bremsstrahlung originating in LA. A fast kicker, which can create an additional 1 mrad horizontal deflection, can be used in conjunction with a septum bend downstream to extract high-charge bunches for the EX section, which is described in §2.1.12. Two collimators also serve to eliminate the beam halo. The beam halo from Touschek scattering has been simulated in detail in §2.1.17 and has been used to dimension the collimators in §2.1.17. Other halo sources still have to be added to the simulation. The first 25 m undulator follows, and is followed by the first cell B.

The linear optics for cell A are shown in Fig. 2.1.27. Eleven quadrupole magnets manipulate the beam from the end of LA to match $\alpha_x = \alpha_y = 0$ and $\beta_x = \beta_y = 12.5$ m at the center of the 25 m undulator. To use definite values in the optics design, we adjust the beta functions in each undulator to half its length. However, the optics design is very flexible and other beta functions can be employed. Additionally, they provide high β_x in the collimators, which

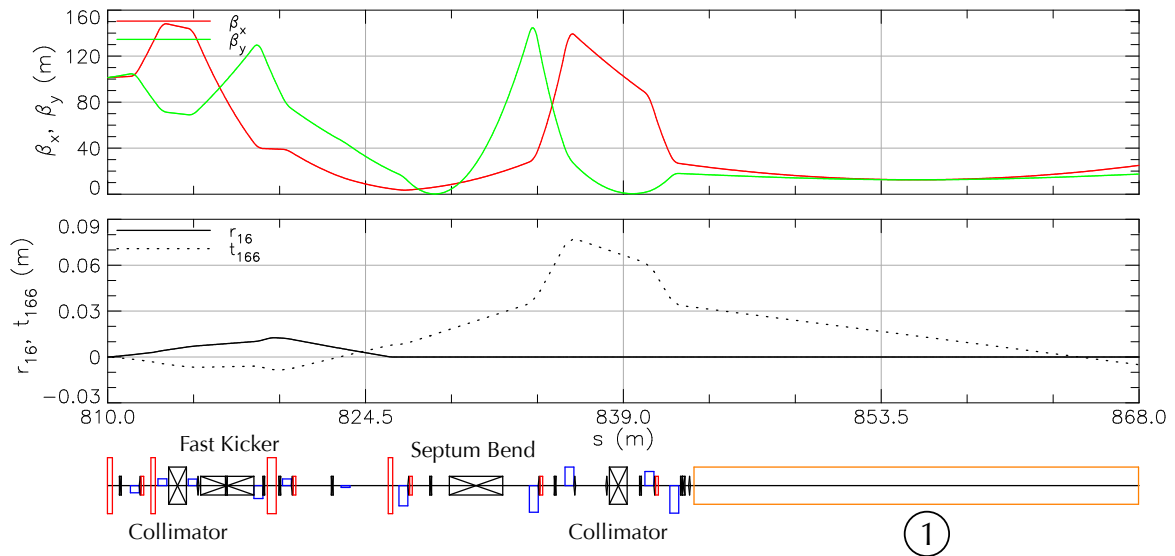


Figure 2.1.27: The optics for cell A in the SA section.

are separated by a 90° horizontal phase advance. The second-order dispersion created here is brought to zero at the end of the following cell B.

The linear optics for the first cell B are shown in Fig. 2.1.28. The cell consists of a two-bend achromat followed by a 5 m undulator. The optics within the undulator are flexible, with this example having $\alpha_x = \alpha_y = 0$ and $\beta_x = \beta_y = 2.5$ m at the center of the undulator. The dispersion and its slope are brought to zero prior to the undulator. Two sextupole magnets placed symmetrically about the center of the achromat provide $t_{166} = 0$ and $t_{266} = 0$ from the prior cell A to the beginning of the undulator. Emittance growth due to ISR is reduced as much as possible while maintaining the Twiss parameter and dispersion requirements in undulators. Additionally, in order to reduce IBS losses, the trajectories of particles scattered in regions of large dispersion are manipulated to pass through insertion devices and undulator protectors. A soft 0.5 mrad bend and a taper protect the undulator from trailing synchrotron radiation from the second bend. This undulator is also protected from beam halo losses by a protector collimator. Four corrector magnets and five BPMs allow for orbit correction.

There are five such cell B sections, with the last containing undulator number 6. The following cell C and the seven cell Ds serve as beam transport lines to undulator number 7, and therefore must primarily limit emittance growth and control the time of flight. The optics for these sections are shown in Fig. 2.1.29. There one can see that linear optics are well contained. The second-order dispersion, while seemingly erratic, is actually optimized to zero at the beginning of undulator number 8, as seen in Fig. 2.1.30.

Cells E and F are shown in this figure. Because the spacings between undulators 7, 8, and 9 are larger than in the previous sections of type cell B, more dipole and quadrupole magnets can be used to make achromatic sections. The 25 m undulator in cell E is very similar to those at the beginning of cell A, so the quadrupole strengths are optimized in the same way to provide $\alpha_x = \alpha_y = 0$ and $\beta_x = \beta_y = 12.5$ m at the center of this undulator. The final four-

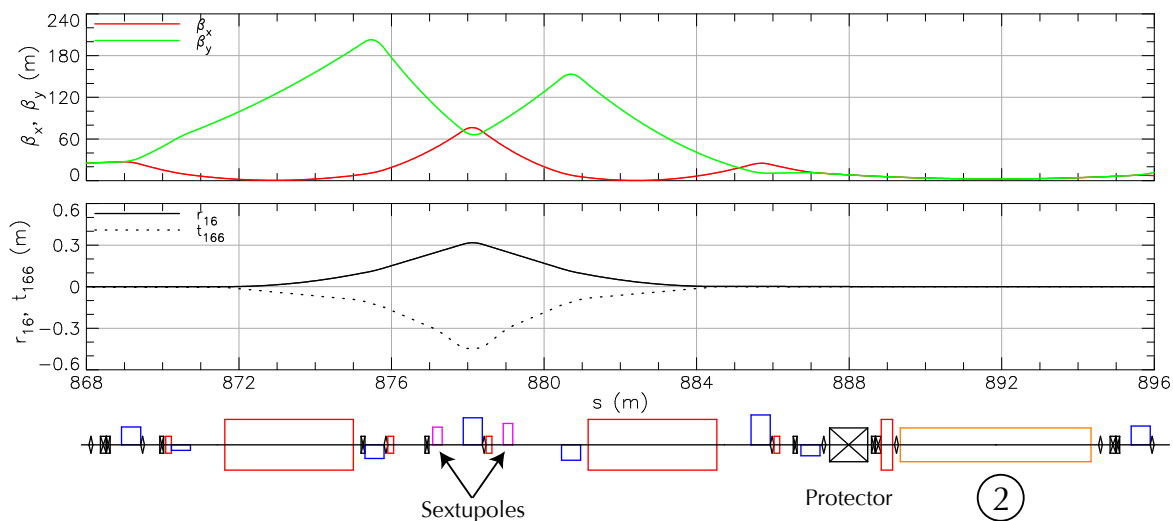


Figure 2.1.28: Optics for the first SA cell B section, which consists of a two-bend achromat followed by a 5 m undulator.

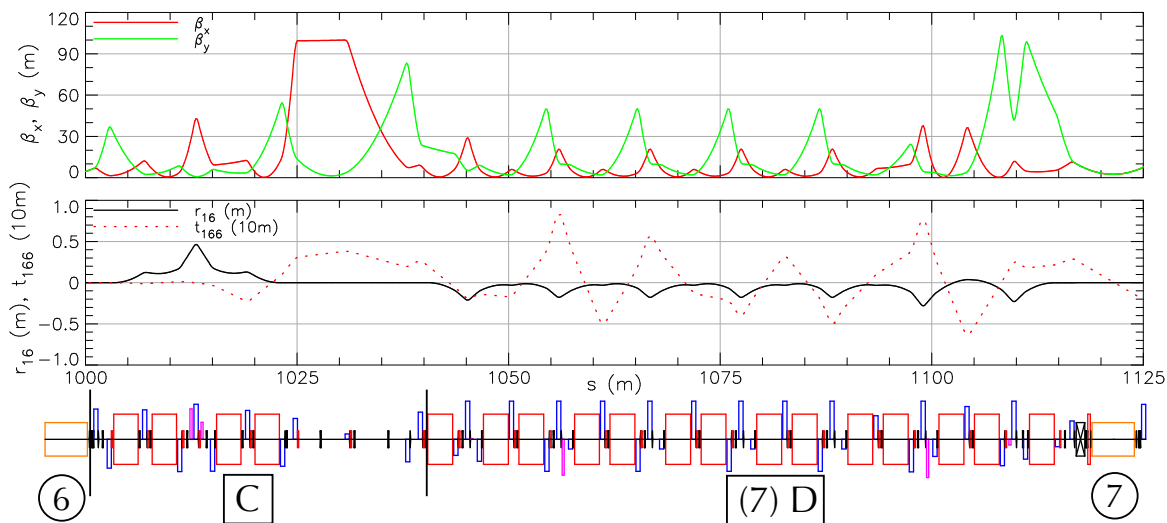


Figure 2.1.29: Optics for the SA cell C and the seven cell D sections.

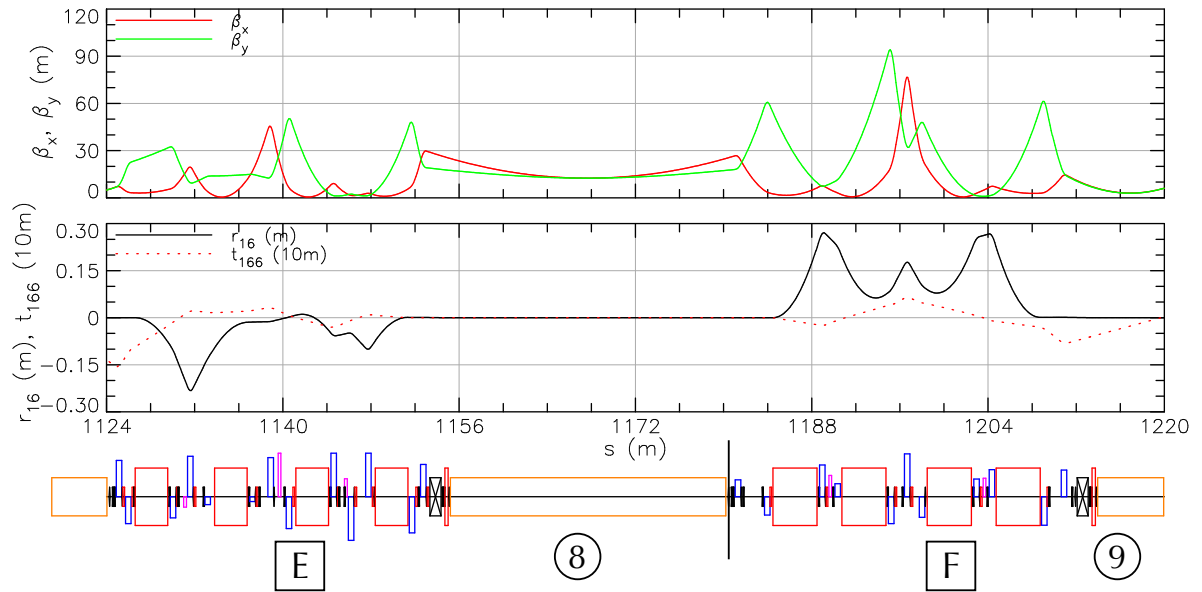


Figure 2.1.30: Optics for the SA cell E and F sections. The quadrupole strengths between the first two undulators are optimized similarly to cell B.

bend achromat focus the beam into the 6 m G-line undulator. The second-order dispersion is controlled by sextupole magnets in the same way as portions of cells A and B.

The optics for the entire SA section are shown in Fig. 2.1.31. Radiative emittance growth and time of flight terms r_{56} and t_{566} are shown in Fig. 2.1.32. One sees that the emittance growth is dominated by portions of cell F. This is due to the relatively strong bends needed to place the undulators in Wilson lab. These bends are among the strongest in the high-energy part of the machine, with bending radii of 36 m and fields of approximately 0.46 T. Note that the total ISR emittance growth at the end of SA amounts to approximately 15% of the mode B emittance in Tab. 1.3.1.

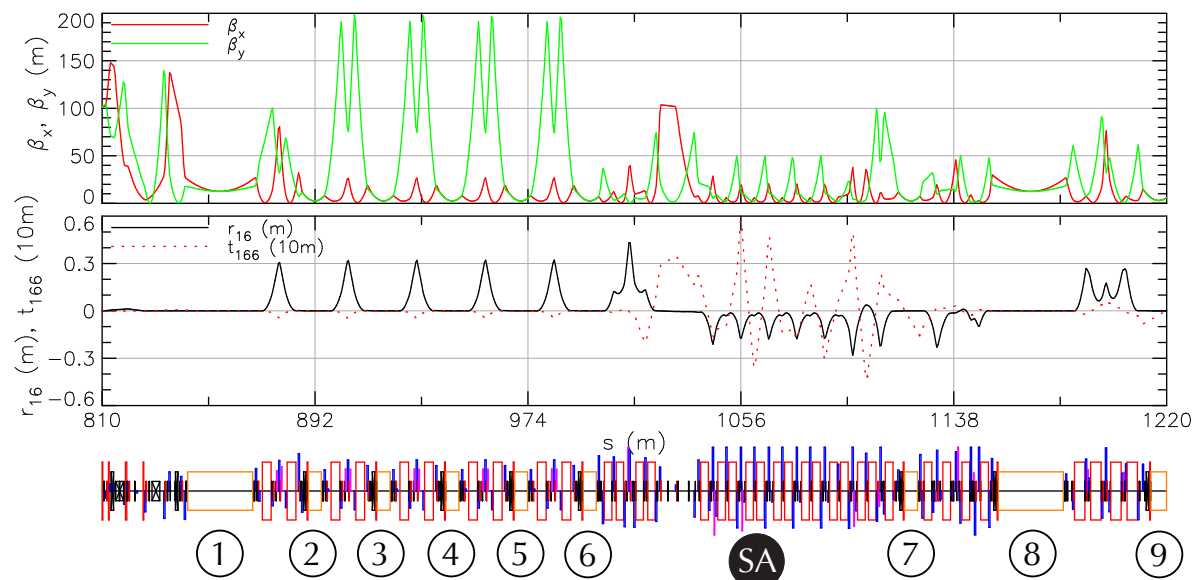


Figure 2.1.31: Optics for the entire SA section.

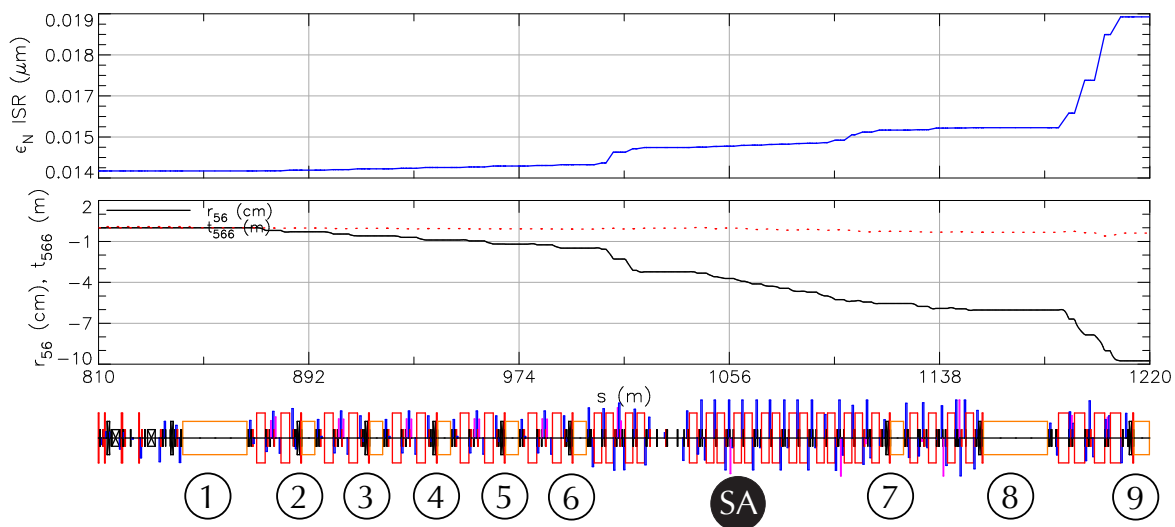


Figure 2.1.32: Normalized radiative emittance growth ϵ_N and time of flight terms r_{56} and t_{566} for the SA. Emittance growth in this section is dominated by relatively strong bends in cell E.

2.1.8 CESR (CE)

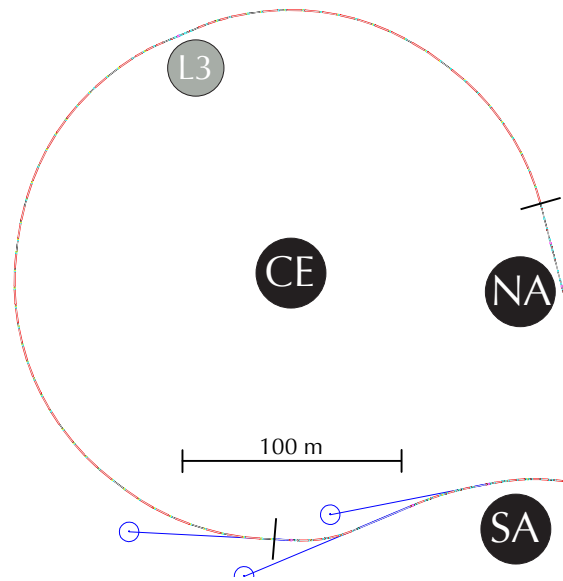


Figure 2.1.33: Layout for the CE section.

Design criteria

The CE section is the only part of the Cornell ERL lattice that already exists. It must

- Accept the SA beam and transport it to the NA section.
- Limit emittance growth.
- Control time of flight terms r_{56} and t_{566} .
- Limit beta functions.
- Be achromatic to second order.
- Provide a collimator for the beam halo.

This section is primarily used for beam transport, but in the bunch-compression mode C it also provides some of the time of flight terms r_{56} and t_{566} needed for compression in the NA section. In order to easily tune the optics of this section with other sections, CE must have $r_{16} = 0$, $r_{26} = 0$, $t_{166} = 0$, and $t_{266} = 0$ as a whole. Finally, it must contain a collimator to remove the beam halo.

System optimization

The CE layout, shown in Fig. 2.1.33, is essentially the current existing layout for a large portion of CESR. The only noteworthy changes are the addition of a collimator in the L3 region around $s = 1550$ m and three additional corrector magnets and BPMs.

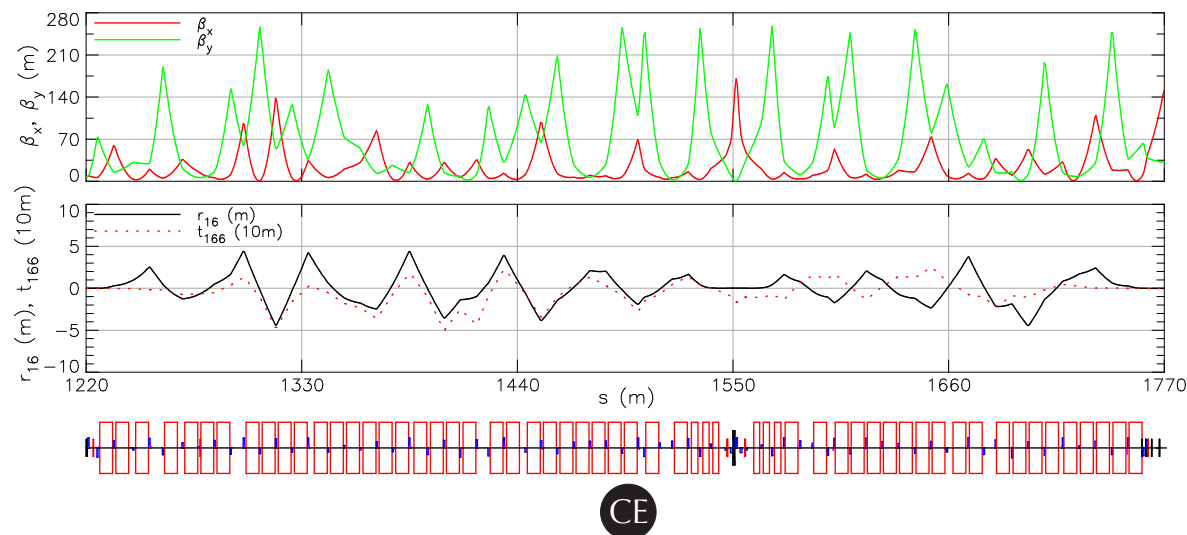


Figure 2.1.34: Optics for the CE section.

The bulk of this section is roughly made up of FODO cells, and therefore does not have the same degree of optics flexibility as the other arcs in the machine. Unfortunately, this configuration is not completely regular, and it does not lend itself to periodic cells as do the other sections. Therefore it is optimized as a whole for controlled beta functions and emittance growth, as well as controlled time of flight terms, by varying all quadrupole strengths for the linear optics and all sextupole strengths for the second-order optics. Special care is also taken that the r_{56} term does not vary too wildly, so that in the bunch compression mode the bunches do not get over-compressed. The resulting optimized optics are shown in Fig. 2.1.34. The radiative emittance grown and time of flight terms are shown in Fig. 2.1.35.

Upgrade optics

The CESR magnets can effectively transport the beam from the SA to the NA, but they contribute to most of the emittance growth in the ERL. Here an upgrade option for the CE section is presented that provides very low emittance growth. It uses the same 6.57 m long dipole magnets as in the CESR as well as the same sextupole magnets, and with about 80 additional quadrupole magnets. The dipoles will produce more bend angle, which their original 8 GeV design can provide. This upgrade therefore only requires new quadrupole magnets, power supplies, vacuum chambers, girders, and stands. In an effort of quality engineering, the baseline ERL design does not contain this upgrade, and therefore the NA x-ray beam lines have significantly larger emittance.

The CESR tunnel is a mixture of pure arcs connected by straight sections. In this upgrade, the CESR dipole magnets are rearranged to span the arcs by periodic cells containing two bends. The straight sections are drifts with three quadrupole magnets. For optimization, CE is divided into seven cell types:

Cell P Periodic cell with two bends – occurs twenty times.

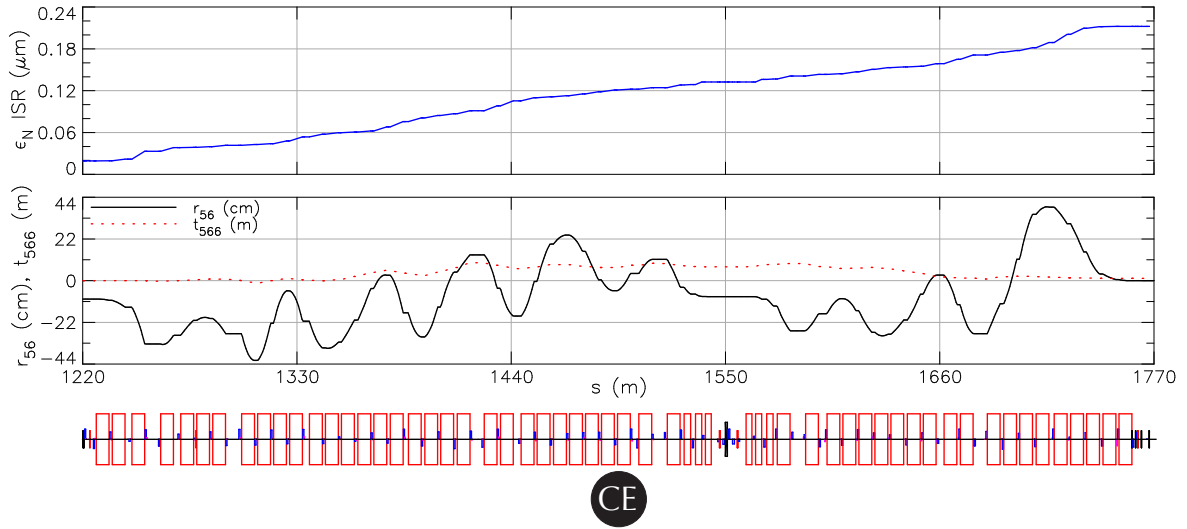


Figure 2.1.35: Normalized radiative emittance growth and time of flight terms for CE for modes A and B. Note that the emittance growth in this section dominates that in the entire 5 GeV arc.

Cell A Matches optics from the SA into the first cell P.

Cell B, C, D, E Matches optics from a cell P to a cell P.

Cell F Matches optics from the last cell P into the NA.

The positions of these cells are shown in Fig. 2.1.38. Essentially multiple cell P sections comprise most of CE, with matching cells A and F for connecting to the SA and the NA, respectively. Cells B, C, D, and E account for the straight sections in the tunnel. Each is similar to two cell P sections, with an extended drift and extra quadrupole magnets between the third and fourth bends.

In a cell P, the four quadrupole strengths are optimized to produce periodic beta functions and first-order dispersion that yield a specified value for the r_{56} contribution and low radiative emittance growth. Next the two sextupole strengths are optimized to produce a specified value for the t_{566} contribution.

The optics for cell B are shown in Fig. 2.1.37. Due to symmetry, it is sufficient to optimize the section by setting the Twiss parameters and dispersion at the entrance to those of the end of cell P, and vary quadrupole strengths symmetrically about the center quadrupole magnet in the straight section to produce $\alpha_x(s_c) = 0$, $\alpha_y(s_c) = 0$, and $D'(s_c) = 0$, with $s = s_c$ at the center of that magnet. The value of $D(s_c)$ can be chosen freely, and therefore the r_{56} contribution by the section is adjustable. The two sextupole strengths are optimized symmetrically to match $t_{266}(s_c) = 0$.

Cells C and E are practically identical to cell B, all having a 6.3 m straight section. Cell D has a longer straight section of 12.2 m, but the optimization strategy is the same as that of cell B. Finally, there are enough quadrupole and sextupole magnets in cell A and cell F to match Twiss parameters between the adjacent sections, and to fine tune the total r_{56} and t_{566}

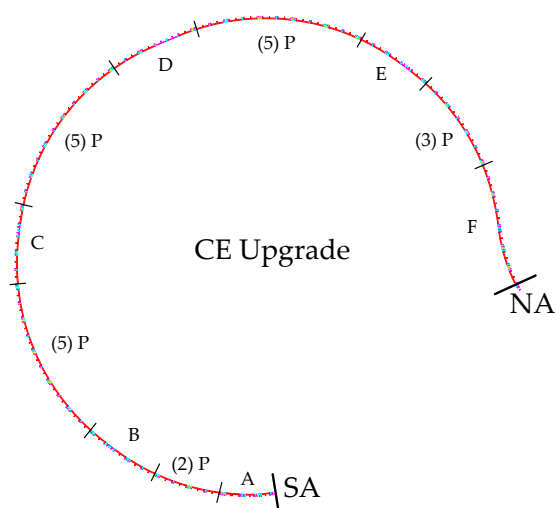


Figure 2.1.36: Layout for an upgrade to the CE section

contributions by CE. The resulting emittance growth and dispersion functions for all of CE are shown in Fig. 2.1.38. There it is seen that, due to the similarity of all the cells, both the emittance growth and dispersion functions are very regular and relatively small in the bulk CE.

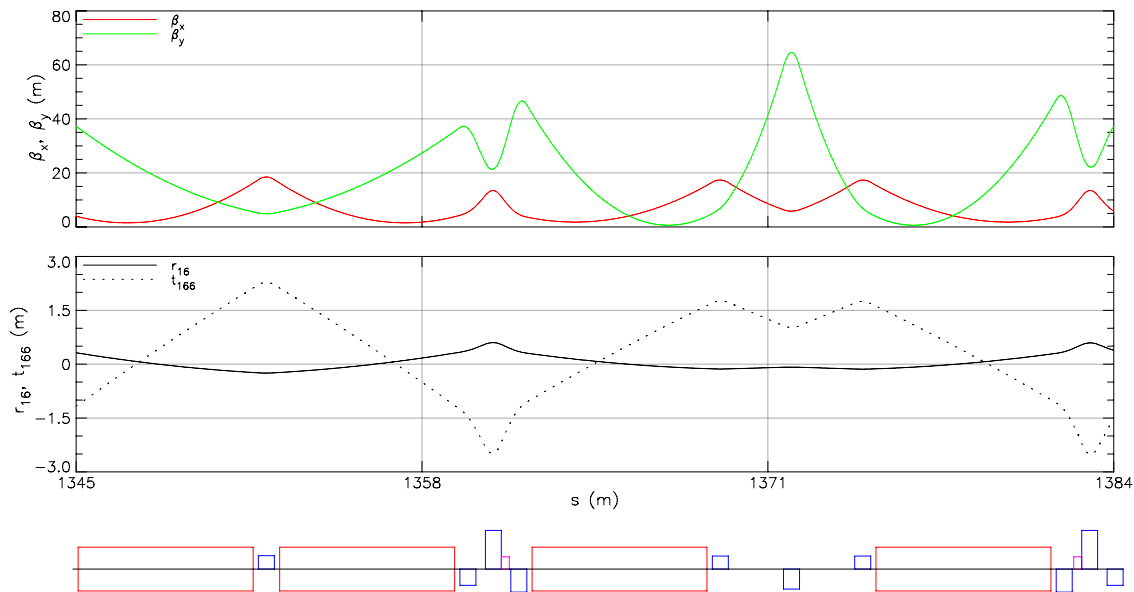


Figure 2.1.37: Optics for the upgrade CE cell B

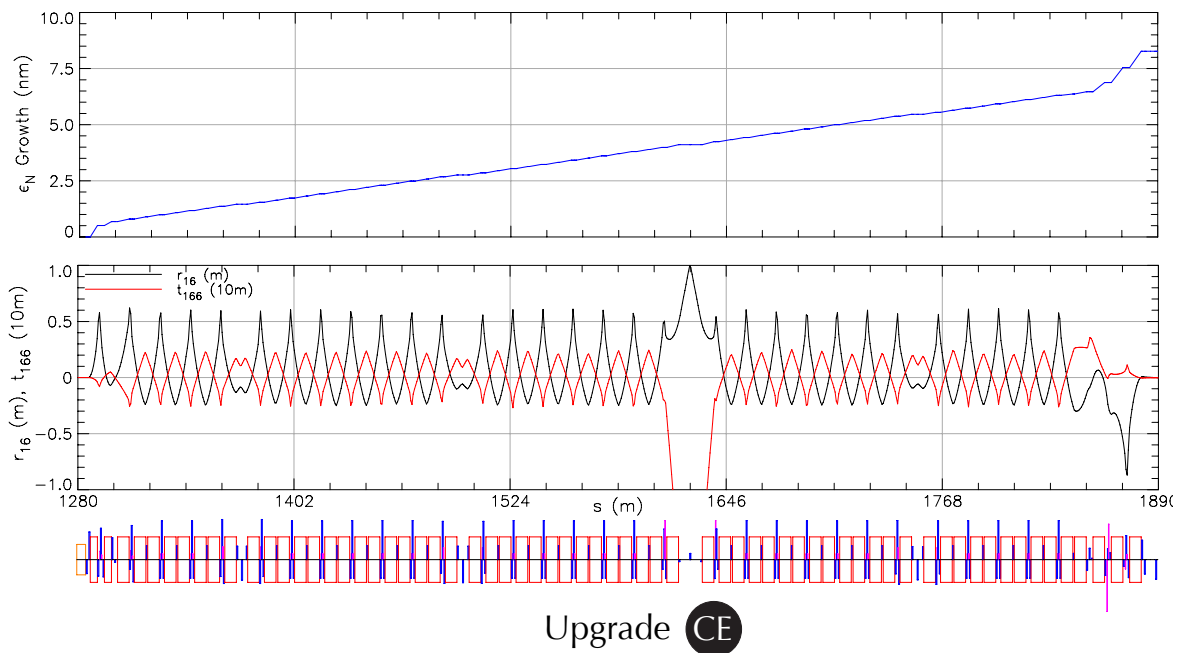


Figure 2.1.38: Optics for the CE upgrade section.

2.1.9 North Arc (NA)

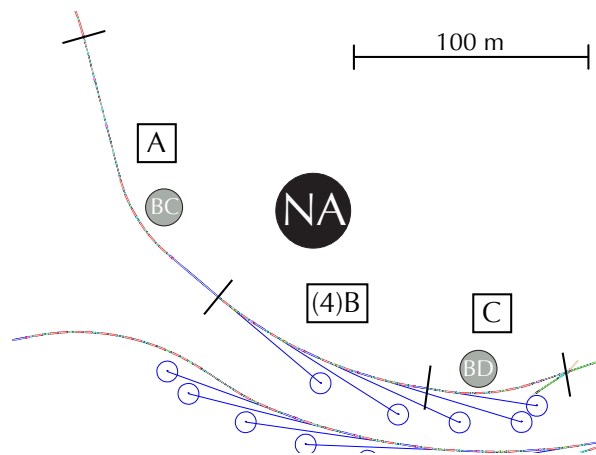


Figure 2.1.39: B.1 26: Layout for the NA section. Part of the SA is shown for reference.

Design criteria

The NA contains the last five undulators in the ERL. This section must

- Receive the beam from CE.
- Contain five undulators in the new building, including one that is 25 m long.
- Collimate the beam halo prior to the first undulator.
- Provide customized beam sizes with zero dispersion in all NA undulators.
- Include a bunch compression section, and be able to maintain short bunches through all undulators.
- Include a bunch decompression section after all undulators, at the end of the NA.
- Merge the high-energy beam into LA for energy recovery.

These criteria are similar to those for the SA described in §2.1.7. Notably the NA contains bunch compression and decompression sections, which are further detailed in §2.1.10.

System optimization

The NA is approximately 290 m long. It is divided into four cell types:

Cell A Matches optics from CE into undulator number 10, and contains a bunch compression subsection BC.

Cell B Periodic section containing a three-bend isochronous achromat and a 5 m undulator – occurs four times.

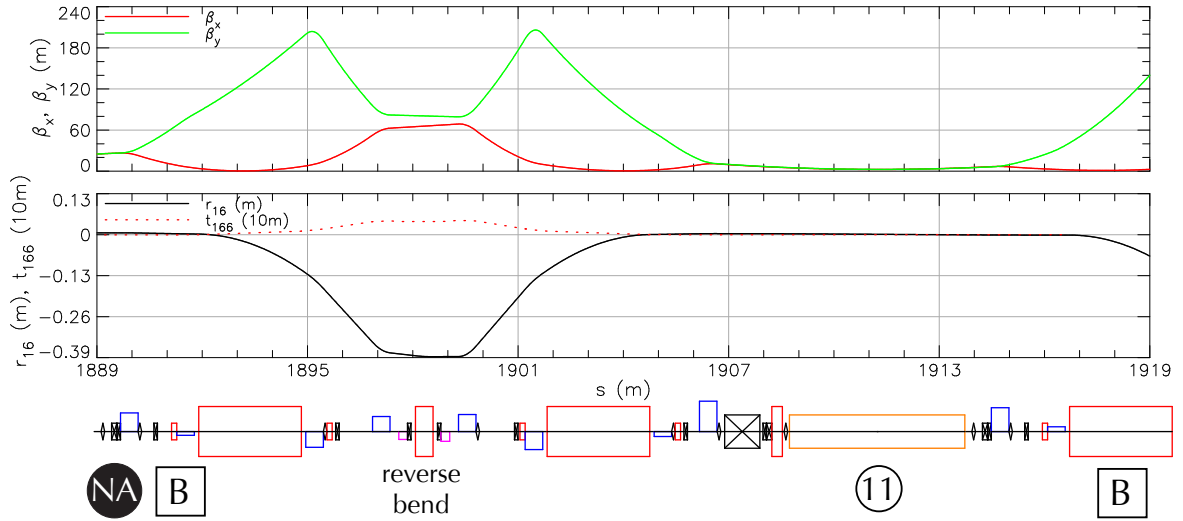


Figure 2.1.40: B.1 27: Optics for the first NA cell B section.

Cell C Matches optics from the last cell B into LB for energy recovery, and contains a bunch decompression subsection BD.

The layout for these cells is shown in Fig. 2.1.39.

In the bunch compression modes, where the BC subsection compresses the bunch, it is necessary to keep the bunch short in all undulators. Therefore, in addition to being achromatic, the arcs between all undulators are also isochronous. This is achieved by adding a short ‘negative’ bend between the two long bends in an achromat, which can be seen in all cell B sections. Besides this short bend, all NA cell B sections are similar to the layout of the SA cell B sections. Cell C is similar to a cell B section, except with a longer 25 m undulator.

Optimization for these cells is therefore similar to the method described in §2.1.7 for the SA cell B, with the additional constraint that $r_{56} = 0$ through a cell. Two sextupole magnets make the section achromatic to second order. The resulting optics for cell B are shown in Fig. 2.1.40.

The NA cell A section matches Twiss parameters and dispersion from CE into undulator number 10. The optics for this cell are shown in Fig. 2.1.41. These optics are for mode A (non-compression), so the bunch compressor section is just an isochronous achromat. The first and second-order dispersion are fine tuned to give the desired r_{56} and t_{566} terms from the beginning of CE to the beginning of the first NA undulator.

This section accepts Twiss parameters and dispersion from the end of CE, and matches them to the first NA cell B section. Additionally, the time of flight terms r_{56} and t_{566} are fine tuned when the ERL is operating in bunch compression mode. All quadrupole and sextupole strengths are varied independently to satisfy these constraints.

After the last 5 m undulator, the NA ends with cell C, containing an arc with 6 bends that connects the beam back into LA for energy recovery. In the mode where the bunch arrives compressed, this section serves to decompress the bunch by providing rather large dispersion through the central bends and a correspondingly large r_{56} compensation. It also contains a

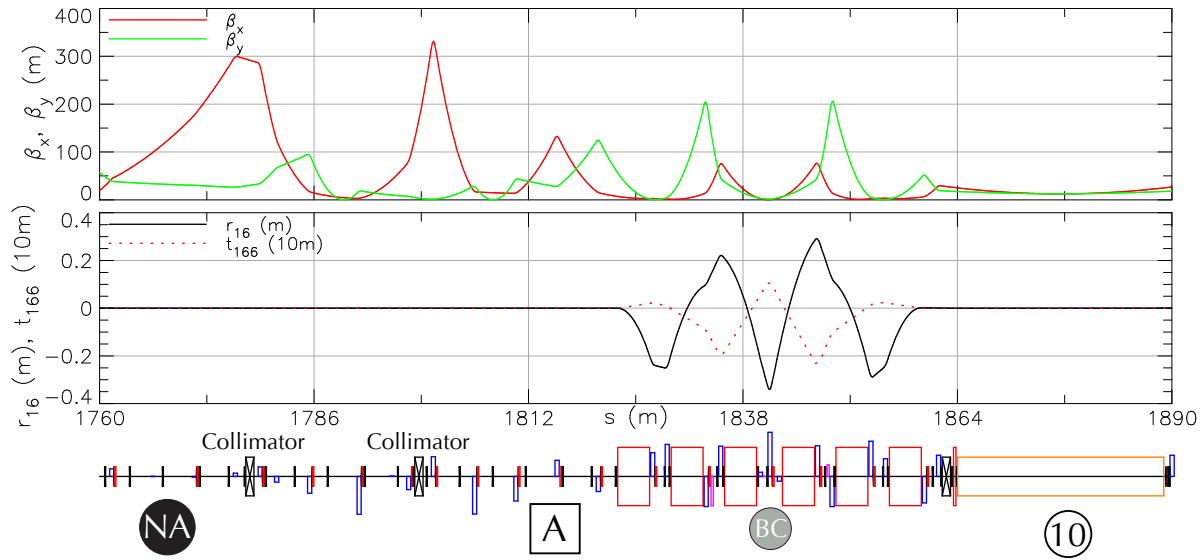


Figure 2.1.41: Optics for the NA cell A section, for mode A.

collimator for the beam halo.

Optics for the entire NA section are shown in Fig. 2.1.42, with radiative emittance growth and time of flight terms shown in Fig. 2.1.43. Because the time of flight terms are calculated starting at the beginning of the SA, one sees that they indeed go to zero at the end of the NA and thus the SA-CE-NA sections together are achromatic and isochronous to second order.

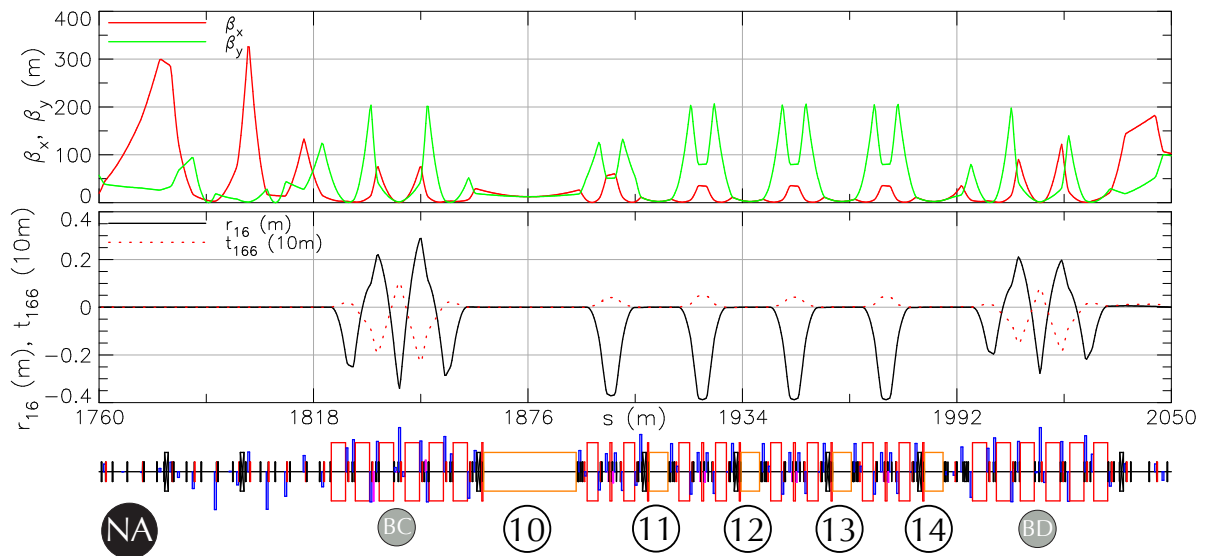
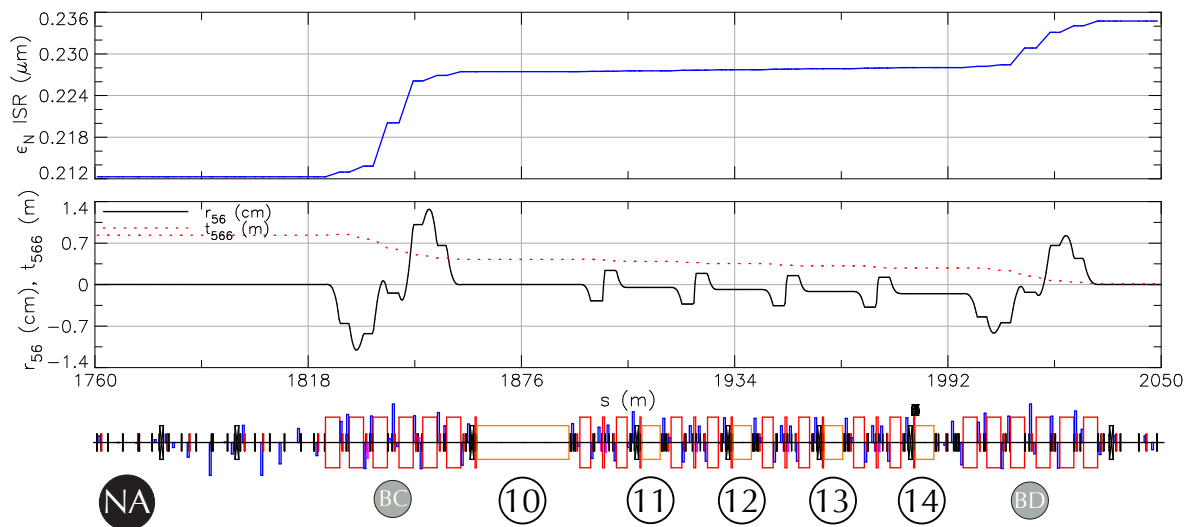


Figure 2.1.42: Optics for the entire NA section.

Figure 2.1.43: Normalized radiative emittance growth ϵ_N and time of flight terms r_{56} and t_{566} for the NA.

2.1.10 Bunch-compression optics in the ERL

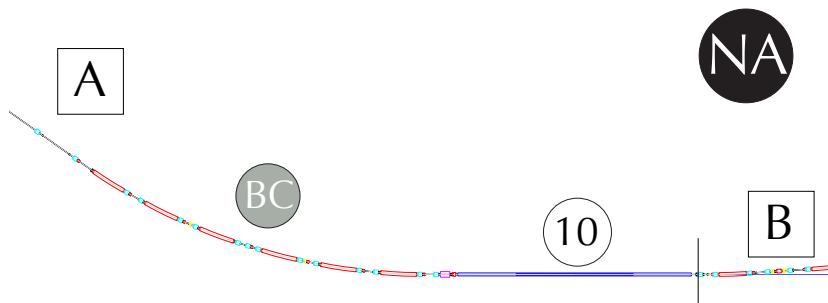


Figure 2.1.44: Layout for the bunch compressor BC in the NA.

Design criteria

The operation mode C in Tab. 1.3.1 calls for compressed bunches in the NA section. The bunch compression scheme for this mode must

- compress bunches to 100 fs prior to all NA undulators. Shorter bunches are possible, but require larger energy spread as shown in Fig. 2.1.45.
- ensure that all undulators see these short bunches.
- decompress these bunches for energy recovery.

In particular, the bunches should undergo final compression in the BC section shown in Fig. 2.1.44. This mode utilizes off-crest acceleration to perform this compression, which greatly increases the full energy spread of the bunch, and can potentially lead to beam losses in regions with large dispersion. Therefore, the initial bunch duration from the injector is chosen to be 1 ps instead of the 2 ps duration of mode A. This leads to relatively higher HOM powers in the Linacs, so mode C operates with a reduced bunch charge of 19 pC, leading to 25 mA average current at 1.3 GHz. This lower bunch charge also reduces the detrimental effect of CSR.

System optimization

Manipulation of the first- and second-order time-of-flight terms r_{56} and t_{566} in the CE and NA sections, combined with off-crest acceleration in LA and LB at phase ϕ , allow bunches to be compressed in the BC section just prior to undulators 10–14. This works as follows: bunches with 1 ps durations are accelerated with $\phi \approx 6.6^\circ$ through LA and LB and enter SA at 5 GeV. The time-of-flight terms r_{56} and t_{566} are controlled throughout the CE region, which partially compresses these bunches, and the six-dipole arc, just prior to undulator 10, performs the final compression to 100 fs. The achromatic arcs between the subsequent undulators each incorporate a ‘reverse’ bend to make them isochronous, and thereby maintain this short bunch length for each undulator. Following the final undulator 14, the bunches are decompressed in

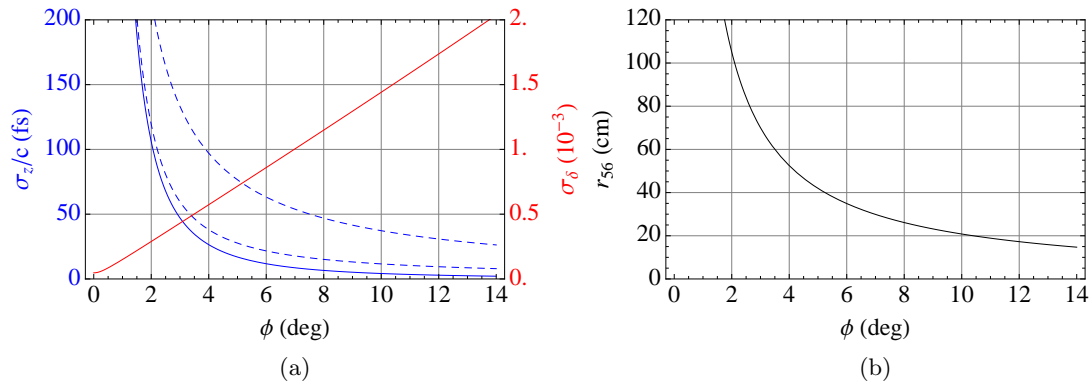


Figure 2.1.45: Estimates of the minimum bunch length from second-order bunch compression at high energy. The blue curve in Fig. 2.1.45a assumes an initial bunch length of 1 ps. The upper dashed line incorporates the expected slice energy spread increase due to ISR in dipole and undulator magnets by $\Delta\sigma_\delta = 5.33 \times 10^{-5}$. If undulator magnets are turned off in the SA section this becomes $\Delta\sigma_\delta = 1.56 \times 10^{-5}$, shown in the lower dashed line. The red line shows the correlated rms energy spread. Figure 2.1.45b shows the required r_{56} term to provide this compression.

a similar six-dipole arc to 1 ps, after which their energy is recovered in a second pass through LA and LB.

There is some freedom in choosing r_{56} , t_{566} , and ϕ to produce the 100 fs bunches. Roughly speaking, using a larger ϕ implies that a smaller r_{56} term is needed to fully compress the bunch, at the cost of a larger relative energy spread σ_δ . In addition, the bunch must be decompressed in a relatively short section at the end of NA, with an r_{56} of approximately the same value and opposite sign as that from the beginning of SA through the BC section. Generally, in order to accommodate all of the other linear optics constraints, it is easiest to make the necessary $|r_{56}|$ as small as possible. With all of these considerations, the baseline mode C lattice has been designed to provide $r_{56} \approx 30$ cm and $t_{566} \approx -1$ m from the beginning of SA through the end of the bunch compressor BC using $\phi \approx -6.6^\circ$.

To estimate what is further possible with second-order compression in the system, the minimum bunch length, along with the energy spread, as a function of accelerating phase ϕ are shown in Fig. 2.1.45a, calculated with formulas that can be found in, for example, [18]. The corresponding r_{56} needed are shown in Fig. 2.1.45b. An important consideration is the energy spread induced by ISR in dipole and undulator magnets, which limits the compression process.

To simulate this bunch compression process, it is also important to consider CSR, which is described in §2.1.14. Depending on the bunch charge and length, CSR can be a limiting factor in the compression process. Fortunately, the bunch parameters in mode C are such that CSR does not hinder our compression or decompression, as shown by particle tracking simulations in Fig. 2.1.46.

Figure 2.1.46 shows that the time-of-flight term r_{56} varies wildly through CE. This is due

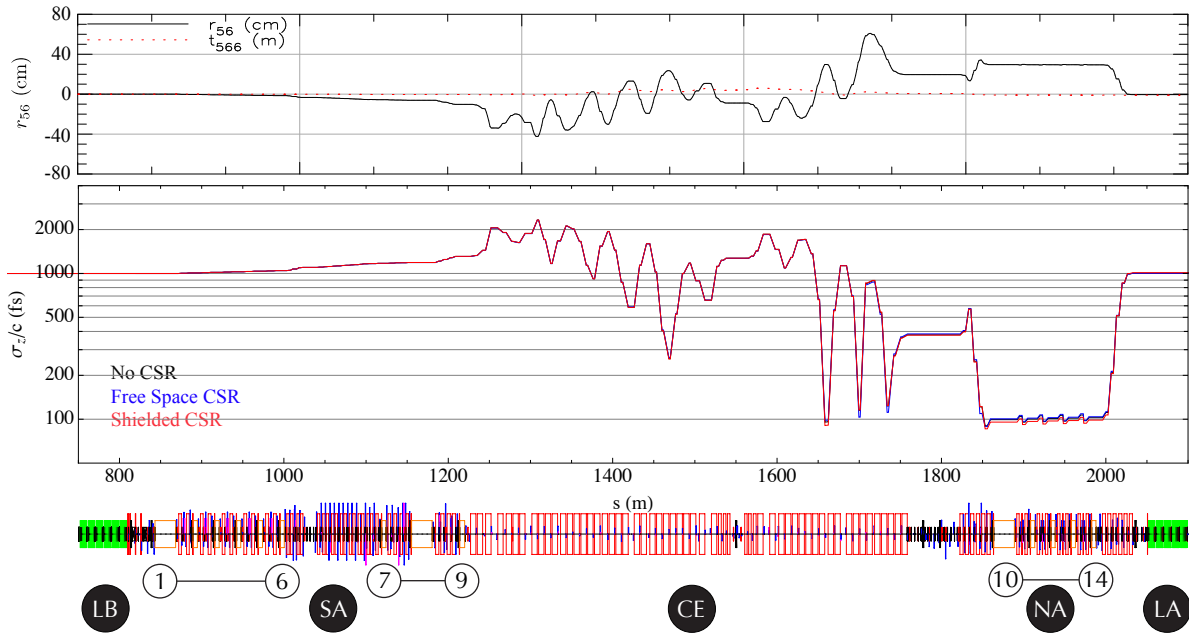


Figure 2.1.46: Bunch length and time-of-flight terms for the bunch-compression mode C through the high-energy arc SA-CE-NA. These simulations track 100,000 particles. Simulations with and without CSR show that our design limits this effect, as described in §2.1.14.

to the relatively fewer quadrupoles in CE compared to other sections, which makes it more difficult to control both the dispersion (the integral of which affects r_{56}) and the beta functions simultaneously. Care is taken, however, to limit the number of times that r_{56} crosses the 30 cm mark, which highly compresses the bunch.

2.1.11 Demerger and Beam Stop (BS)

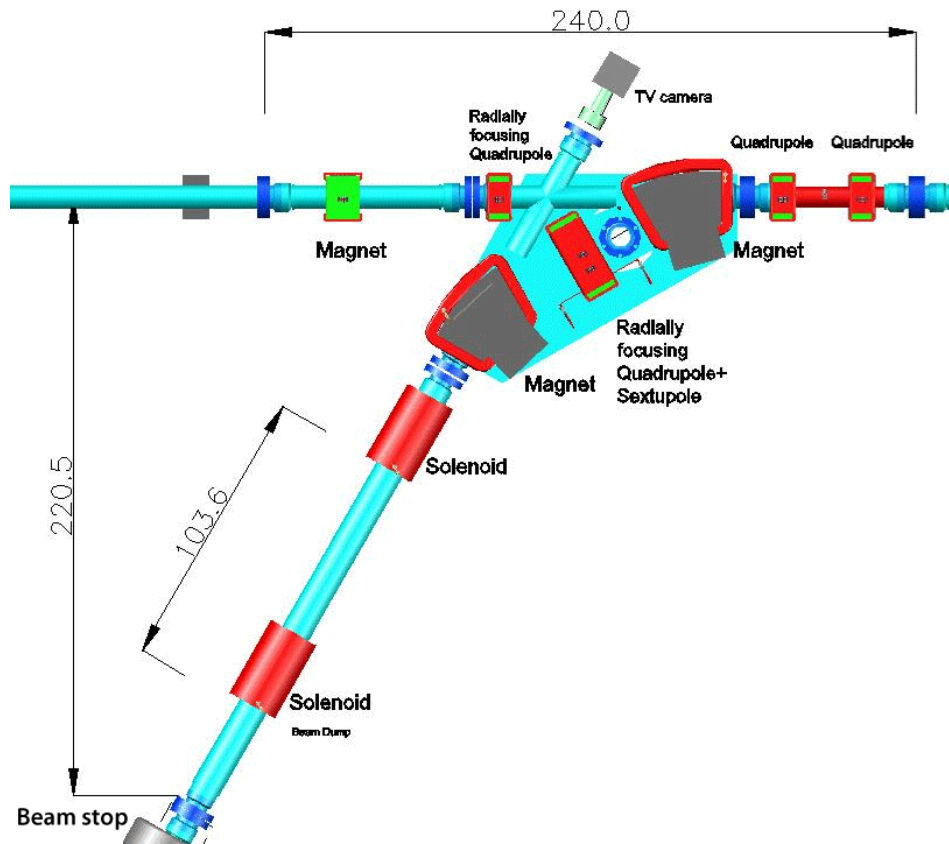


Figure 2.1.47: The achromatic section of bends used to separate high- and low-energy beams. It uses two bending magnets and a quadrupole in between. This quadrupole is equipped with a sextupole corrector. Dimensions are given in cm.

Design criteria

The demerger and beam stop are located directly after LB, the south string of SRF structures. Together these sections must

- demerge the second-pass 10 MeV beam from the first-pass 5 GeV beam.
- have an energy acceptance of ± 2.5 MeV.
- expand the low energy beam as much as possible for absorption at the beam stop.

The demerger serves to separate the low-energy from the high-energy beams. It is located directly after LB, the south string of SRF structures. The high-energy beam has an average energy of $\langle \mathcal{E} \rangle \approx 5$ GeV and a small rms energy spread $\sigma_\delta = \delta\mathcal{E}/\mathcal{E} \approx 2 \times 10^{-4}$. The low-energy beam, which has already been used for x-ray production, has an average energy $\langle \mathcal{E} \rangle \approx 10$ MeV

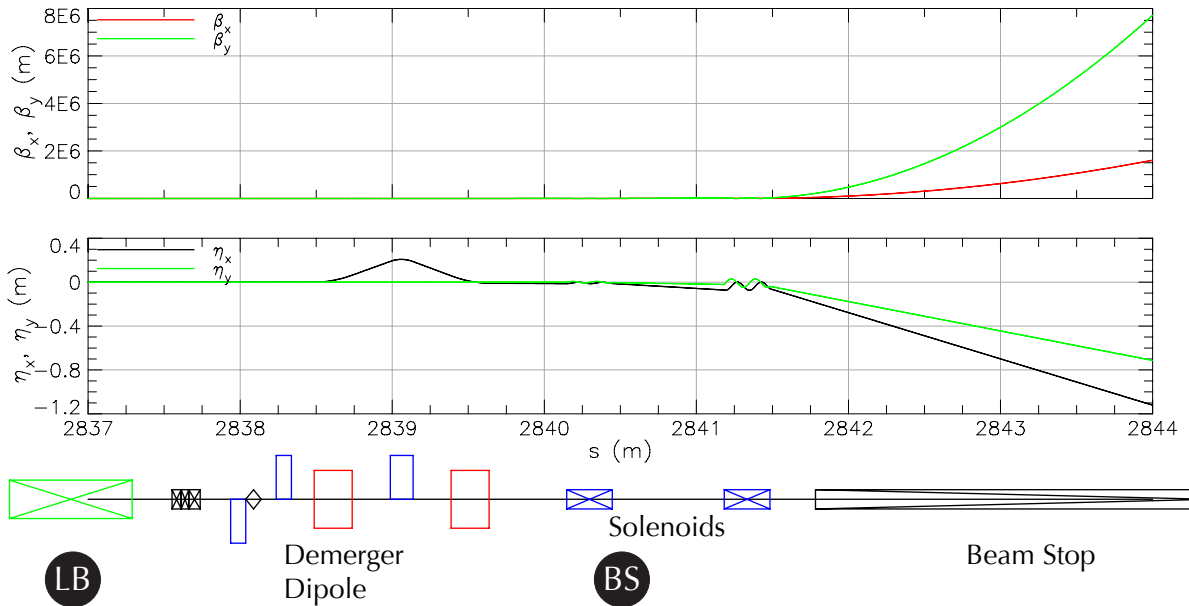


Figure 2.1.48: Envelope functions and dispersion in the beam-stop line. Dipoles are shown as red boxes, quadrupoles as blue boxes and solenoids by blue boxes with a cross. The beam is coming from the left.

and an full energy spread of $\Delta\mathcal{E} \approx \pm 1$ MeV, which can be seen later in Fig. 2.1.62. The line that transfers this beam to the beam stop therefore needs to have very large energy acceptance, and has to be able to accept significant beam loss. Finally, it is crucial to have a large beam size to lower the power density in the beam-stop system.

System optimization

Each dipole magnet in the BS section bends the low-energy beam by $\phi \approx 30^\circ$, with a bending radius of $\rho \approx 0.5$ m. The 5 GeV beam only passes through the first magnet and is bent by only approximately 1 mrad.

To compensate the dispersion generated after the separation magnet, the demerger is equipped with a radially focusing quadrupole and a complementary bending magnet, so that the total BS section bend becomes achromatic. Because the energy of the beam is low, this quadrupole lens can be constructed as a Hand-Panofsky quadrupole. This lens is equipped with sextupole correction windings to compensate the quadrupole's chromaticity contribution. The windings in the rectangular frame are generated by a linear current variation at the top and bottom poles, and by a parabolic current distribution at the side walls of the quadrupole. Another possible solution for the magnets might be a permanent magnet, with a coil for field control. This would provide beam stop protection in the case of power supply failure, a practice that is typical for high-power systems.

The beam in between the two large aperture bends is allowed to be approximately ± 6 cm wide. The wide walls of the chamber are covered in the graphite absorbers to protect against beam loss by energy fluctuations.

In the optics model presented here, a solenoid installed in front of the beam-stop is used as a simplifying model to control the beam size. In reality, an over-focusing quadrupole will be used. This magnet produces horizontal and vertical crossovers near its exit, to allow for rapid expansion of beam dimensions as shown in Fig. 2.1.48. The next magnet provides three corrector coils arranged in form of a sextupole, powered with three-phase 60 Hz AC. These coils will sweep the electron beam in the transverse direction to create a circular sweep with 60 Hz.

2.1.12 Extraction line (EX)

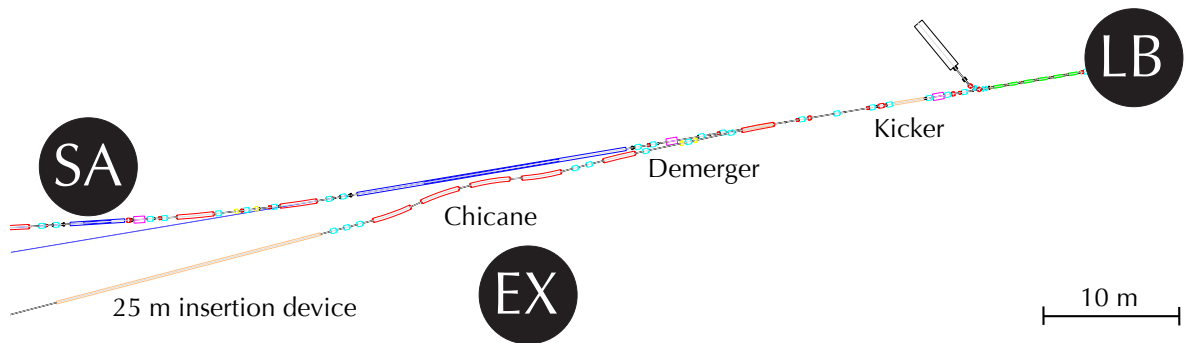


Figure 2.1.49: Layout for the EX section.

Design criteria

The relatively low bunch charge in the bunch compression scheme described in §2.1.10 leads to compression that is not limited by CSR. However, a bunch with a much higher charge of 1 nC would be significantly damaged in this compression process, and it would be difficult to recapture its energy in deceleration. In order to study the use of such bunches, an extraction beamline section EX has been designed that

- extracts high-charge (1 nC) bunches from the exit of LB at a rate of below 100 kHz.
- compresses these bunches to 100 fs duration or less.
- provides space for a 25 m long insertion device.

In order to avoid the detrimental effects of CSR for 1 nC bunches in the TA, this high-charge bunch must remain relatively long (2 ps), and be compressed at high energy (5 GeV). An appropriate bunch compressor must take second-order effects into account, which adds complications to the large energy spread associated with compression to 100 fs or less. We have therefore designed a very simple four dipole bunch compressor without sextuples at high energy that uses second-order time-of-flight terms in the turnaround arc rather than in the bunch compressor. This design was tested using particle tracking simulations that incorporate CSR.

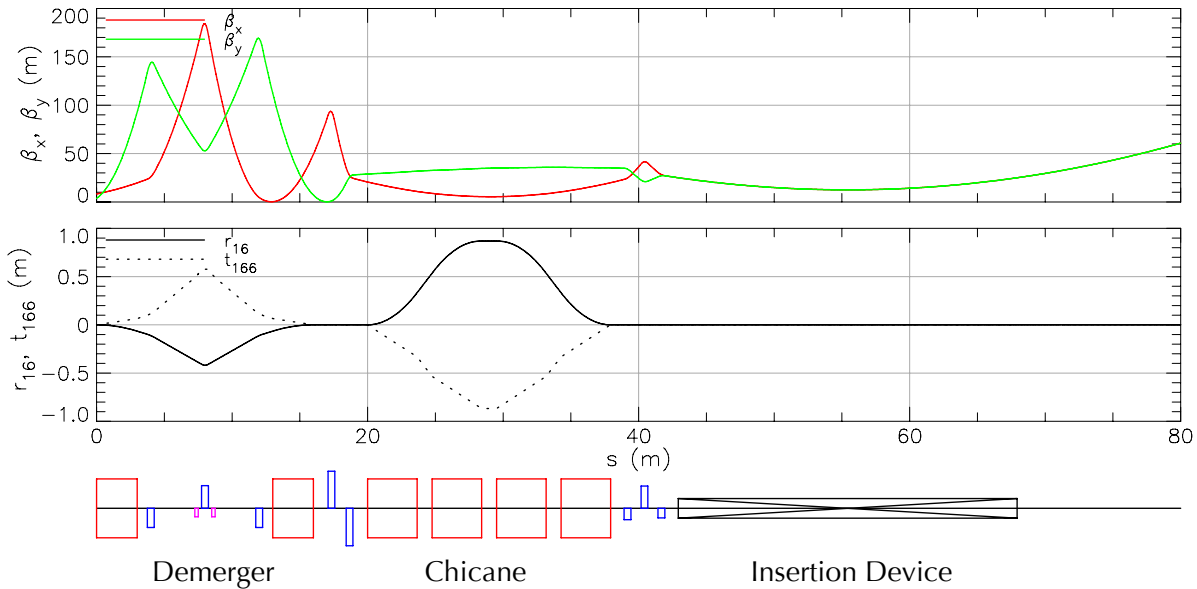


Figure 2.1.50: Optics for the EX section. The chicane and demerger together provide a time-of-flight term $r_{56} = 23.5$ cm to compress the bunch for the 25 m long insertion device.

Table 2.1.2: Beam parameters after the extraction line EX

	77 pC	1 nC	Unit
ϵ_x	280	2300	pm
ϵ_y	33	33	pm
σ_δ	2.6	2.6	10^{-3}

System optimization

The EX compressor lattice consists of three parts: an achromatic demerger section, the chicane compressor, and finally an undulator. Because energy is not recovered in compression, the beam must be extracted from the main line. Extraction is done by kicking the beam by 1 mrad, then demerging the beam with two bending magnets, then bending the beam 2.5° each from the main line. Between these two magnets, a quadrupole triplet with field strengths of approximately 10 T/m is optimized to cancel the dispersion introduced by the demerging bends. Also the aberrations t_{166} and t_{266} are canceled.

Following the demerger, a quadrupole doublet is placed to control the beta functions entering the compressor and undulator. The compressor itself is a simple chicane achromat consisting of four equal and opposite dipoles each bending by 10.5° with a 20 m radius. The optics for the EX section are shown in Fig. 2.1.50.

The demerger lattice in Fig. 2.1.49 is very close to the main line it bends away from, so to avoid overlapping elements the positions of the magnets in this section are limited to the open spaces between the structures in the main line.

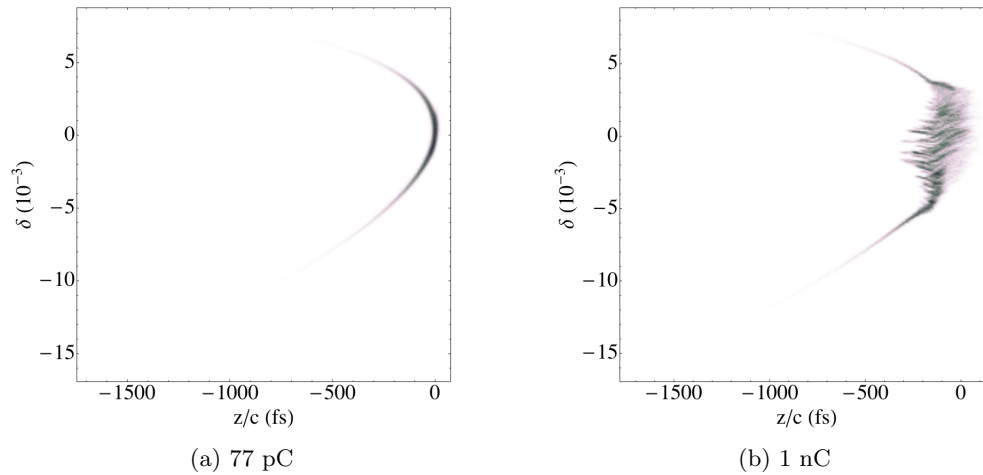


Figure 2.1.51: The longitudinal phase space for particles at the end of the chicane shown in Fig. 2.1.50 for bunches of different charge. These simulations tracked 200,000 particles and used the 1-D shielded CSR method in Bmad [22]. The bunch durations for both situations is approximately 100 fs.

Examples of the CSR damage to bunches in this compressor are shown in Fig. 2.1.51. These simulations were done using the 1-D shielded CSR method in Bmad [22]. Both the 77 pC and 1 nC bunches achieve the desired 100 fs duration, but the 1 nC bunch suffers significantly more emittance growth. Beam parameters after the extraction line for both bunch charges is shown in Tab. 2.1.2. Radiation characteristics from FELs using this extraction line are currently being considered [23].

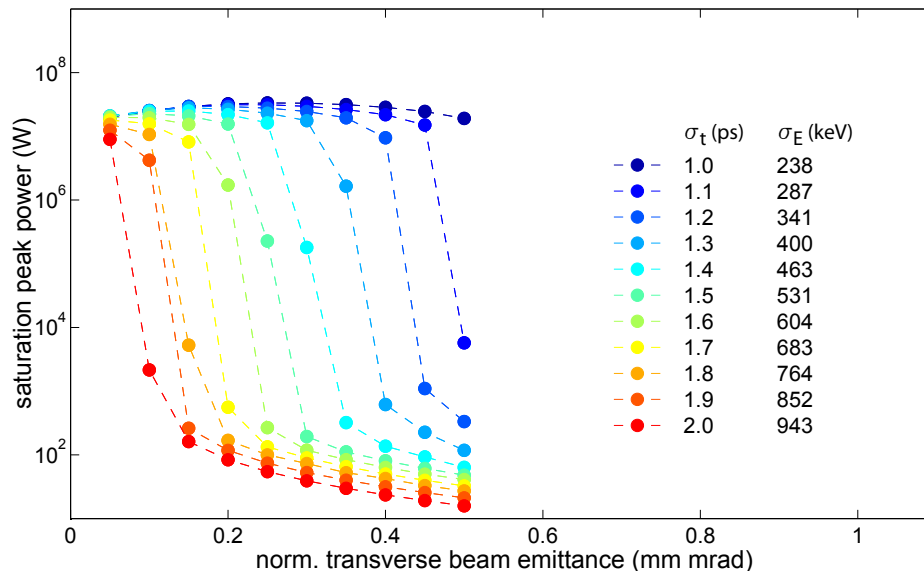


Figure 2.1.52: Simulated intra-cavity power of an XFEL-O driven by the Cornell ERL. Shown is the peak power at saturation as a function of transverse beam emittance and bunch duration generated in the injector. A bunch charge of 25 pC was assumed, as well as an undulator with 3000 periods of $\lambda_U = 15$ mm. The radiation wavelength is 0.103 nm.

2.1.13 Electrons for an XFEL-O

The CW operation of the accelerator, its high repetition rate, as well as the very small beam emittance make the Cornell ERL an superb machine to test and operate future accelerator technologies. A very promising scheme is an FEL oscillator operating in the hard x-ray regime (XFEL-O), which was proposed and analyzed in various references [24–27]. More detailed studies are underway. Here we only show a feasibility study for driving such a light source with beam parameters similar to the ERL high coherence Mode B. The resonator of such an FEL would be composed of high-reflectivity, narrow-bandwidth Bragg mirrors of sapphire or diamond crystals and reasonable resonator dimensions to yield pulse round-trip rates of ~ 1 MHz. Such a device is expected to produce transform limited picosecond x-ray pulses with megawatts of beam power and a resulting narrow bandwidth as small as $\Delta\omega/\omega \sim 10^{-7}$. Due to the very narrow bandwidth, this would be a complementary source of x-rays compared to SASE x-ray FELs, both of which provide comparable peak spectral brightnesses.

We present an initial analysis of the feasibility for an XFEL-O within the Cornell ERL by following up on the work presented in [27]. In that work, a 1D code was developed to simulate the evolution of the light field in the optical resonator and its interaction with the driving electron beam. Comparisons of this 1D code with the 2D code `GINGER` give very good agreement, which is why the studies presented here are based on the faster 1D code. The simulations assume an undulator with 3000 periods of $\lambda_U = 15$ mm, tuned to a fundamental

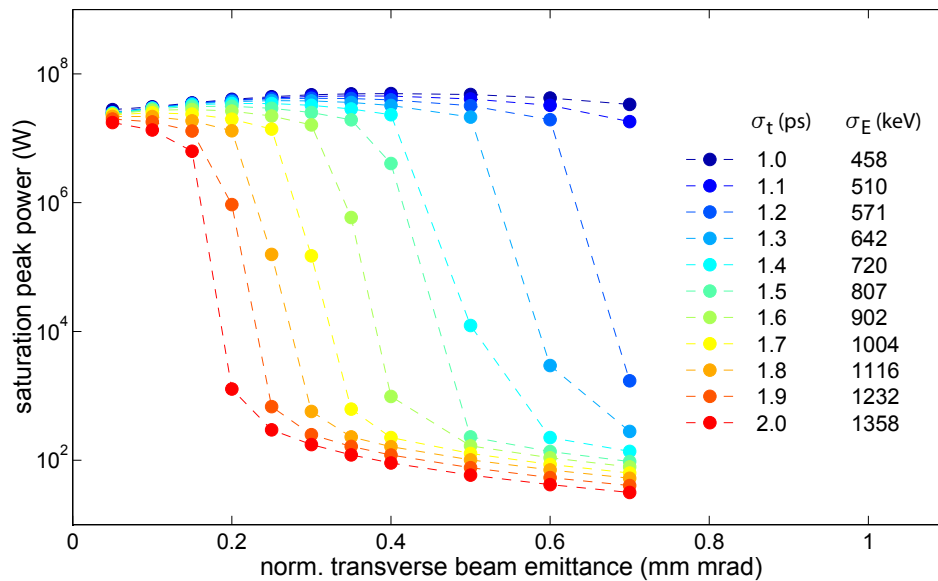


Figure 2.1.53: Simulated intra-cavity power of an XFEL-O driven by the Cornell ERL if operated at 7 GeV, provided by accelerating (rather than decelerating) the beam in the second pass through Linac A. Shown is the peak power at saturation as a function of the transverse beam emittance and the bunch duration generated in the injector. A bunch charge of 25 pC was assumed as well as an undulator with 3000 periods of $\lambda_U = 15$ mm. The radiation wavelength is 0.103 nm.

radiation wavelength of $\lambda_{\text{ph}} = 0.103$ nm for a 5 GeV electron beam. The (spectral) losses in the resonator are the same as in [27] (15% per roundtrip including 4% of the power which is coupled out by a thin Bragg mirror). The radiation is focussed with grazing incidence mirrors to provide a waist within the undulator. The Rayleigh length was used to optimize the linear FEL gain and the electron beam optics was matched to the light beam.

A small transverse beam emittance and a small energy spread are of greatest importance to achieve a sufficiently high FEL gain. Simulations of the expected intra-cavity peak power have been performed for various transverse beam emittances and various bunch durations generated in the injector. As an example, we have adopted a bunch charge of 25 pC in all cases, and a beam energy spread assumed to be normally-distributed and composed of two contributions: curvature of the accelerating fields and incoherent synchrotron radiation. Figure 2.1.52 summarizes the simulation results and indicates that a shorter bunch duration of around 1 ps or less would be favorable, since this relaxes significantly the requirements on the normalized transverse beam emittance. The results also indicate that the expected beam emittances will likely be small enough to allow the operation of an XFEL-O. A higher beam energy would relax the requirements on the beam emittance, which is indicated in Figure 2.1.53 and would relax requirements on the undulator period.

While in principle an XFEL-O could be driven by an electron beam the repetition rate of which is an integer multiple of the fundamental XFEL-O resonator frequency, the thermal load might be a limiting factor.

2.1.14 Wakefield effects

Impedance budget

Wakefields from vacuum-chamber discontinuities can cause (a) component heating, (b) instabilities, (c) correlated energy spread. Component heating and instabilities tend to be the dominant effects in storage rings, whereas the correlated energy spread is the dominant concern in an ERL, where the relative energy spread is amplified by the high- to low-energy ratio during deceleration [28], about a factor of 500 in the Cornell ERL. Care has to be taken that this energy spread is not too large to transport the beam into the beam stop. The total energy loss and component heating also has to be considered. The power loss in a vacuum component with loss parameter k_{loss} for an average circulating current I_{av} at a repetition frequency f_{rep} is

$$P_{\text{loss}} = \frac{I_{\text{av}}^2 \cdot k_{\text{loss}}}{f_{\text{rep}}} = 7.69 \text{ W} \left(\frac{k_{\text{loss}}}{1 \text{ V/pC}} \right), \quad (2.1.14)$$

where the second equality gives the proportionality constant for this ERL design in regions with a single beam for operation mode A. The constant is doubled when two beams pass through the same chamber.

The correlated energy spread is caused by the induced wakevoltage seen by a reference particle traveling with the bunch a distance s behind the bunch center. For a bunch charge q_b , the induced voltage for one traversal of the ERL is

$$V_{\parallel}(s)|_{\text{ERL}} = q_b \cdot W_{\parallel}(s)|_{\text{ERL}} \quad (2.1.15)$$

where $W_{\parallel}(s)$ is the longitudinal wake at the particle's position s . The maximum energy acceptance of the beam stop $\Delta\mathcal{E}_{\text{acc}}$ limits the allowable energy spread of the beam and if the wakefields alone are only permitted to produce 50% of the energy acceptance, the maximum permissible wakefield for $q_b = 77 \text{ pC}$ is

$$\max \left\{ W_{\parallel}(s)|_{\text{ERL}} \right\} \leq 0.5 \frac{1}{q_b} \Delta\mathcal{E}_{\text{acc}} = 0.5 \cdot \frac{5 \text{ MeV}}{77 \text{ pC}} = 32 \text{ kV/pC} \quad (2.1.16)$$

where the beam stop has an energy acceptance of $\pm 2.5 \text{ MeV}$. This places an impedance budget limit on the total ERL wakefield of 32 kV/pC .

The wakefields and loss parameters have been estimated for models of the ERLs vacuum-chamber components with the simulation programs ABCI [29], NOVO [30], MAFIA [31], and with analytic models for surface-roughness and resistive-wall wakefields. The RF accelerator structures were modeled by scaling the wakefield for the TESLA RF structure [32]. Results are summarized in Tab. 2.1.3 for a Gaussian-shaped bunch of length $\sigma_z = 0.6 \text{ mm}$ for the most significant vacuum-chamber components. Accounting for the change in beam-pipe cross-section, calculations for the HOM-load chambers, neglecting ferrite absorber tiles, were undertaken using NOVO. The following vacuum-chamber components were approximated by cylinder-symmetric models using ABCI: 1) The expansion joint is a 4 mm thick tube sliding inside a 35 mm diameter tube with spring-finger contacts breaching the 1 mm gap between the sliding surfaces and 30° tapers at each end, 9 mm apart. 2) The BPM button was modeled as a 15 mm square plate attached to a 1 mm stem with a 1 mm gap between the electrode and the wall. 3) The stripline was modeled as a 2.3 mm thick conducting shell with a 4 mm radial step to

Table 2.1.3: Wakefield and loss-parameter contributions for the total number (or length) of each component in the ERL. If unspecified, the radius of the beam pipe r_{pipe} is 12.7 mm.

Component	Number or length	Neg. Wake (kV/pC)	Pos. Wake (kV/pC)	k_{loss} (kV/pC)
7-cell RF cavity	2×384	-6.47	0	5.81
HOM load ($r_{\text{pipe}} = 110$ mm)	384	-0.50	0	0.36
Expansion Joint	356	-0.74	0.10	0.53
BPM (Button)	664	-0.35	0	0.24
BPM (Stripline)	20	-0.01	0	0.01
Flange joint	356	-0.90	0	0.64
Clearing electrode	150	-0.18	0.14	0.04
Gate valve	68	-0.71	0.69	0.42
Resistive wall ($r_{\text{pipe}} = 12.7$ mm)	2500 m	-4.00	0	2.75
Surf. rough. $3\mu\text{m}$ ($r_{\text{pipe}} = 12.7$ mm)	2500 m	-14.00	0.50	8.75
Undulator taper ($r_{\text{pipe}} = 3$ mm)	18	-0.61	0.37	0.36
Resistive wall ($r_{\text{pipe}} = 3$ mm)	144 m	-0.98	0	0.69
Surf. rough. $0.5\mu\text{m}$ ($r_{\text{pipe}} = 3$ mm)	144 m	-3.60	0.12	2.52

the outer wall and a 1 mm gap at its end. 4) The vacuum-chamber flange is an approximation of a Varian flange with a 2.5 mm outward radial step, a 10 mm long and a 2 mm thick gasket extends 2 mm radially inward from the larger diameter. 5) The gate valve was approximated by a 12 mm diameter tube 5 mm long connected to the beam pipe with 40° tapers. 6) The tapered undulator chambers were simulated by a radially-inward taper to 5 mm radius pipe with the taper length of 25 mm. MAFIA was used to calculate the ion-clearing electrodes as two opposite diamond-shaped plates, 25 mm long and with a 30° taper at their ends. Each undulator is preceded by a protector collimator with a 5 mm aperture. Because this is larger than the 3 mm undulator apertures, the protectors have been neglected in Tab. 2.1.3.

For the full beam traversal, Tab. 2.1.3 gives the number or total length of the components, the maximum excursions of the wakefield within 3σ of the center of the bunch, and the loss parameter. It shows that along with the 7-cell RF Cavity structures, the surface-roughness and resistive-wall wakefield in the standard beam pipes (12.7 mm radius) and surface roughness of the undulator beam pipes (3 mm were used here) are the most important contributors to the ERL wakefield. The surface-roughness parameters for the standard beam pipe and undulator beam pipe were $3\ \mu\text{m}$ and $0.5\ \mu\text{m}$, respectively.

Since in general the maxima and minima of the wakefields for different components do not occur at the same position s , the individual wake functions must be summed to compute the total ERL wakefield, which is seen in Fig. 2.1.54. The peak-to-peak variation of the wakefield over the bunch distribution is 30 kV/pC, just below the impedance limit. The calculations give a value of 24 kV/pC for the ERL loss parameter k_{loss} and a predicted power loss of 180 kW distributed fairly uniformly around the ERL for the 100 mA circulating beam. Note that as our design evolves, these wake estimates will evolve accordingly.

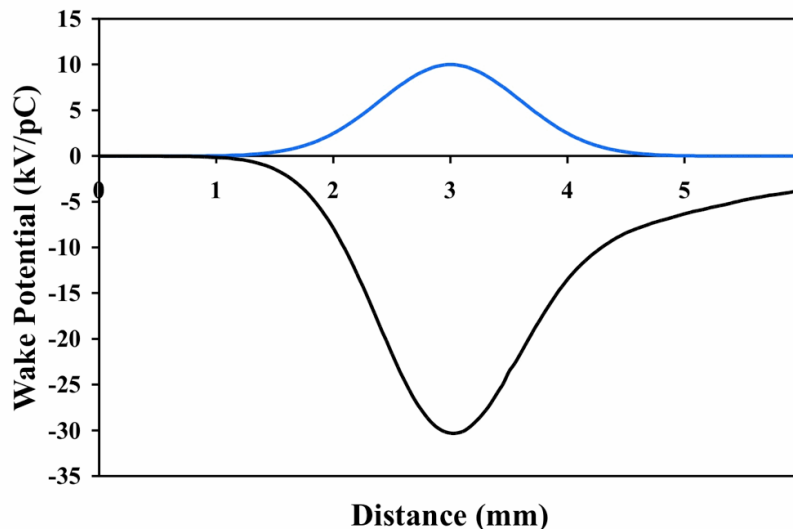


Figure 2.1.54: Total wakefield (lower trace) of the components in Tab. 2.1.3 for a Gaussian-shaped bunch (upper trace.) The peak-to-peak variation of the wakefield is 30 kV/pC.

CSR wakes

When a charged particle is transversely accelerated in a bending magnet, it produces radiation according to the well-known synchrotron radiation spectrum. When N such particles are bunched on a scale of length σ , the power spectrum per particle at frequencies smaller than c/σ in this spectrum is enhanced by roughly a factor N . This results in increased radiation, and hence increased energy losses from the individual particles. This coherent synchrotron radiation was first calculated in a seminal paper by Schwinger [33].

Here the CSR wake $W_{\text{CSR}}(z)$ is the energy change per unit length of a particle with longitudinal position z in a bunch, and it can be shown that for ultra-relativistic particles this $W_{\text{CSR}}(z)$ scales with the factor

$$W_0 = Nr_c m c^2 \left(\frac{\kappa}{\sigma^2} \right)^{2/3} \quad (2.1.17)$$

where m is the mass of a single particle, r_c is its classical electromagnetic radius, and κ is the trajectory curvature (e.g. see [2]).

Additionally, the low frequencies of the radiation spectrum are ‘shielded’ when the particles travel inside a conducting structure. In [33], Schwinger calculated the radiation spectrum for particles traveling in a circle between two infinite conducting parallel plates, and concluded that the lowest frequencies are suppressed depending on the plate separation h , as well as κ and σ . His formulas, however, are difficult to evaluate numerically due to the presence of very high-order Bessel functions, but fortunately an excellent approximation for ultra-relativistic particles can be found in the appendix of [34]. Some manipulation reveals that this suppression depends entirely on the shielding parameter

$$b_s = h \left(\frac{\kappa}{\sigma^2} \right)^{1/3} \quad (2.1.18)$$

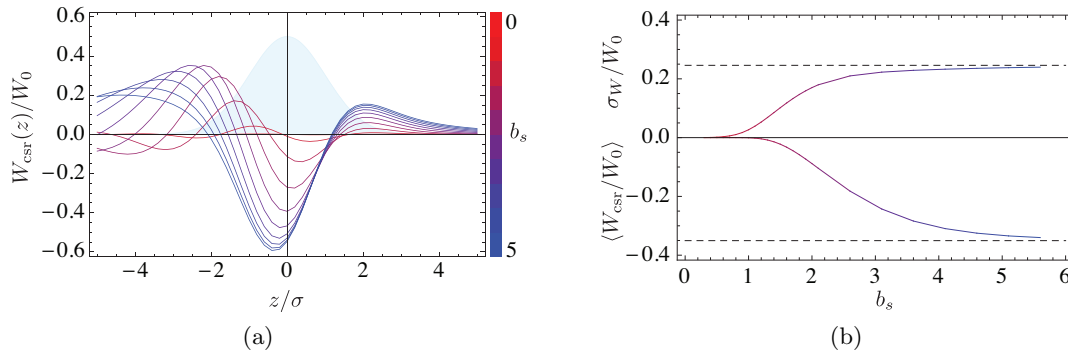


Figure 2.1.55: Normalized shielded steady-state CSR wakes W_{CSR} for a Gaussian bunch of length σ , along with average energy loss and energy spread from these curves for various shielding parameters b_s .

and the longitudinal bunch density (see section 5.2.2 in [35] and a heuristic argument in [22]).

To visualize this suppression, Fig. 2.1.55a shows the CSR wakes for a bunch with Gaussian longitudinal density for various b_s . The averages and standard deviations of these wakes over the distribution are shown in Fig. 2.1.55b and reveal that shielding plays a significant role when $b_s \lesssim 3$. The dashed lines are drawn at the limiting values of these curves, and are approximately -0.35 and 0.25. This is the ‘free-space’ regime.

Using the design bunch lengths, Fig. 2.1.56a show b_s for operating modes A, B, and C in all of the bends in the ERL. This plot suggests that CSR in modes A and B will be strongly shielded, but that mode C will not be, especially in the short pulse region. For a more accurate CSR calculation we use Bmad, which simulates shielding using the image charge method, and is able to calculate all of the entrance and exit transient effects that are not seen in curves like Fig. 2.1.55a. This code has been benchmarked against other codes as well as analytical formulas in [22].

Figure 2.1.56b shows the cumulative energy losses due to CSR by tracking particles through the ERL lattice, along with estimates from the values in Fig. 2.1.56a. As expected, modes A and B are well shielded, but mode C suffers energy loss in the short pulse region. Nevertheless, CSR does not limit the bunch compression process, as shown in Fig. 2.1.57a (also previously suggested in Fig. 2.1.46) with the CSR calculation turned on and off.

Finally, even though CSR does not limit the compressed bunch length, we must check that this bunch can still be decompressed for energy recovery. The relative energy distribution after deceleration to 10 MeV for mode C is shown in Fig. 2.1.57b.

Compensation of wakefield effects

As seen in §2.1.14, the energy spread within the bunch caused by wakefields from the vacuum chamber structures places an important limitation on both the vacuum chamber design via the impedance budget for the ERL and the design of the accelerator in the vicinity of the beam stop. Several methods have been explored for partially compensating the effects of the wakefields in order to relax some of the design constraints and to allow for larger operational

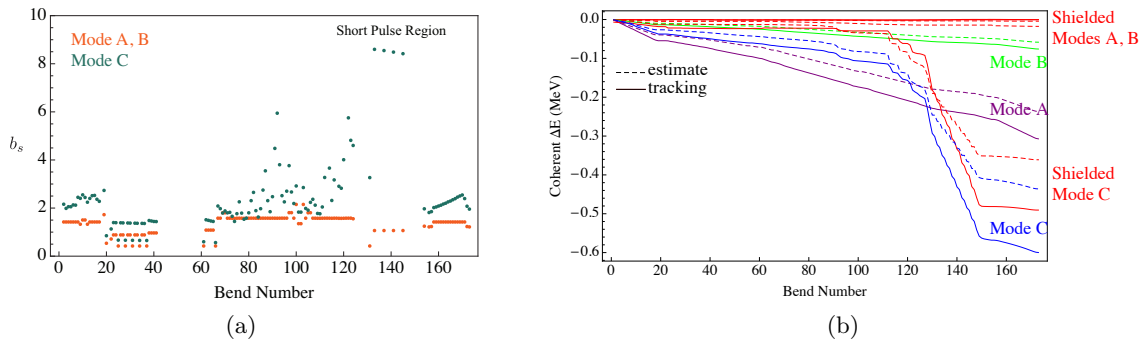


Figure 2.1.56: The shielding parameter b_s at all bends in the Cornell ERL for the different bunch operation modes is shown in Fig. 2.1.56a. Modes A and B use the same optics, and bunches in this mode have durations of $\sigma_z/c \simeq 2$ ps, and mode C compresses the bunches to 100 fs. Figure 2.1.56b shows an estimate for the cumulative coherent energy losses through these bends using the bottom curve in Fig. 2.1.55b, along with particle tracking results from Bmad that take into account all entrance and exit transients for the CSR wake.

margin.

The correlated energy spread of the bunches may be reduced by decreasing its slope and curvature in the time-energy phase space. One class of possible solutions utilizes the acceleration of the bunch off-crest in the Linacs, an energy-dependent time-of-flight transport followed by acceleration of the bunch off-crest in the Linacs. Three options for the location of the time-of-flight transport for this method were explored, 1) in CE, 2) in a single turn-around arc for both accelerated and decelerated beams and 3) two turn-around arcs TA and TB, one for each of the beams [36].

When the necessary time-of-flight transport is added to 1) the CE arc, the beam must be accelerated off-crest and admitted into CE with a first-order phase-space energy correlation, which produces a large energy spread that will broaden the x-ray spectrum undesirably in the experimental regions, making this possibility unfeasible. For solution 2) with the common turn-around loop, it is necessary to operate the two Linacs off the RF field crest by $\Delta\phi$. However, the curvature correlation added to the time-energy phase space in the first pass through the common turn-around arc is removed in the beam's second pass through the arc. This method does not permit the compensation of even-order time-energy correlations.

However, method 3) with two turn-around loops permits different time-energy correlations to be created in the each arc thereby allowing independent reduction of the beam energy spread in the CESR arc and at the beam stop. Simply using the independent phasing of the two Linac sections reduces the energy spread by about a factor of 3 [36]. From these considerations it was concluded that two separate turn-around arcs are necessary to accommodate a reduction in the beam energy spread.

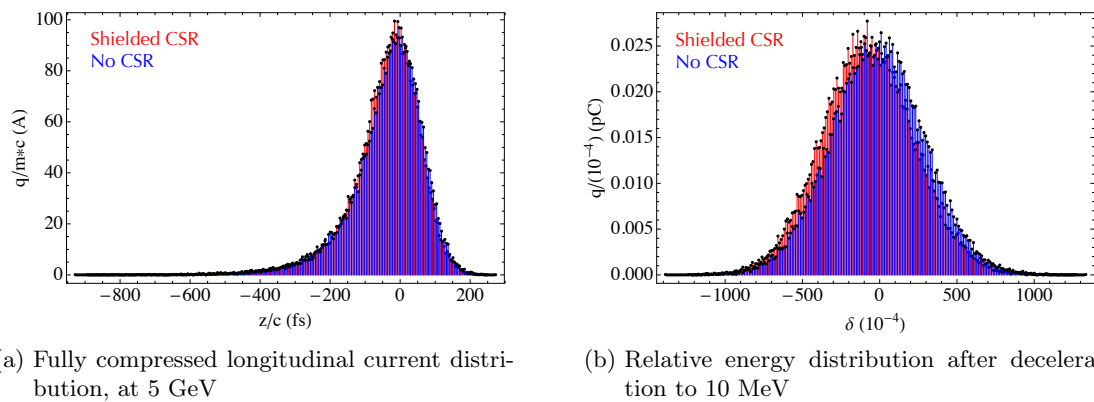


Figure 2.1.57: The longitudinal current distribution in the final undulator for the compressed mode C, as well as the relative energy distribution just prior to the beam stop demerger, from particle tracking in Bmad (with and without the CSR calculation).

2.1.15 Start-to-end simulation

Overview

The ERL lattice is designed assuming perfect alignment and field qualities of all components. Electron bunches injected with the design phase-space distributions will still experience some distortions due to, for example, incoherent synchrotron radiation and geometric optical aberrations, but will do so in predictable ways. Unfortunately the actual machine built will not have such perfect qualities, and furthermore, many of the errors in this machine will not be known *ab initio*. Particles injected into this realistic machine should be kept near the design orbit, and to that end a set of beam position monitors (BPMs) and orbit corrector coils are installed in the lattice. This scheme is described below, along with an analysis of allowable tolerances in the ERL.

Additionally, the collective effects of space charge and CSR influence the bunch distributions in ways that require computationally intensive particle simulations in order to obtain reasonable estimates. Fortunately space charge is only a dominant effect at low energies, and has already been taken into account in large multi-objective optimizations described in §2.1.4 using the code GPT.

Start to end simulations must therefore first deal with errors in the model and their compensation by orbit correction, and then proceed to particle tracking.

Orbit correction

To understand the capabilities of modern orbit correction schemes, consider the following achievements at existing facilities. At the Advanced Photon Source (APS), extensive incremental improvements to orbit stabilization systems have been made since the machine went in operation in 1996. The strategy for achieving true sub-micron orbit stability at the APS has been to study and compensate for multiple systematic effects and noise sources, enhance orbit correction feedback systems, and employ feed-forward methodology where applicable [37]. At the European Synchrotron Radiation Facility (ESRF), in addition to a slow orbit correction (every 5 minutes), a fast global feedback system (4.4 kHz) is implemented to correct, in the vertical direction, the fast orbit distortion caused by quadrupole magnet vibrations [38]. Similarly, a slow correction procedure is used at ELETTRA to counteract slow orbit motions and drifts due to thermal effects, while a number of local fast orbit feedback systems are installed to correct faster orbit disturbances generated by ID gap changes, by vibrations of the quadrupole magnets and by ripple of the magnet power supplies [39]. At SPring-8, sub-micron orbit stability is achieved not by the feedback systems alone, but by thorough source suppression as a first step and some proper feedback correction to push the stability up to the sub-micron level as a second step [40]. In the Swiss Light Source (SLS), long and short term orbit stability of the electron beam is achieved by dynamic alignment systems and by fast closed orbit feedback [41]. The SLS reproduces and stabilizes a previously established reference orbit within $1/10^{\text{th}}$ of the vertical beam size corresponding to $\approx 1 \mu\text{m}$ at the insertion devices (IDs) [42, 43]. Required and achieved orbit stability for these machines are listed in Tab. 2.1.4.

Orbit stabilization requires the maintenance of two different tolerances: uncorrected (jitters) and slower orbit changes that can be compensated by feedback. Here we show a detailed

Table 2.1.4: Orbit stability of third generation synchrotron light sources

Machine	Horizontal Orbit (μm)		Vertical Orbit (μm)	
	Requirement	Achieved	Requirement	Achieved
APS	14.0	12.6	0.45	0.59
ESRF	N/A	1.0	N/A	0.6
ALS	10.3	2	1.2	0.5
ELETTRA	5.0	0.85	5	0.47
Spring-8	28.0	4	0.4	1
SLS	N/A	1.0	0.7	0.6

Table 2.1.5: Counts for BPMs and correctors for all of the sections in the ERL.

	LA	LB	TA	TB	SA	CE	NA	Total
BPM	35	31	38	33	81	70	52	340
Corrector Pair	35	29	30	26	54	1	37	212
Horizontal Correctors	0	0	0	0	6	39	2	47
Vertical Correctors	0	0	0	0	4	37	3	44

analysis of the latter. The former is still under investigation.

An orbit correction scheme based on singular value decomposition (SVD) has been implemented in the Bmad and Tao simulation environments. This scheme minimizes the deviation of the orbit from the design reference, with monitors located at critical locations (such as undulators and collimators) receiving extra emphasis. Additionally, the strengths of the corrector coils are added to this minimization algorithm, so that unreasonably strong fields are not required. Finally, the dispersion is corrected at critical locations. An example of this correction is shown in Fig. 2.1.58. Note that the physical orbit correction system is described in §2.10.2 and §2.10.3.

The number of and placement of monitors and correctors has also been optimized using SVD decomposition techniques on the generalized response matrices from correctors and errors to monitors. See, for example, [44]. Counts of these devices, per section, are shown in Tab. 2.1.5.

Many errors are simulated for the ERL, and are listed in Tab. 2.1.6. For example, magnetic field errors caused by power supply fluctuations can affect both the particle orbit and the optics [45]. Magnetic field fluctuations can cause wrong beam steering that leads to emittance growth and thus increase the beam size at the ID sections. Similarly, quadrupole field errors can affect the beta function and phase advance in both vertical and horizontal directions. Furthermore, a combination of dipole field errors and quadrupole field errors, although a second-order effect, can have a significant impact on the particle's orbit in the insertion devices. In addition to power supply fluctuations, the misalignment of accelerator components can lead to orbit distortions and beam-emittance dilution. A misaligned quadrupole magnet can create, in addition to the quadrupole field for beam focusing, an effective dipole field that will introduce unwanted dispersion. An RF cavity with a pitch angle can accelerate the beam in off-axis directions, and thus produce time-varying transverse deflections that lead to emittance growth.

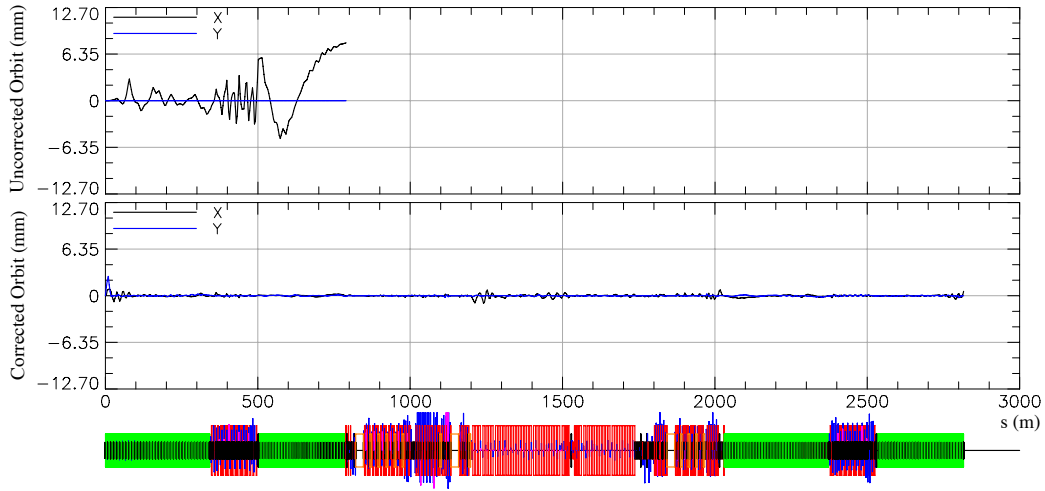


Figure 2.1.58: Examples of the beam orbit before and after correction.

The baseline values listed in Tab. 2.1.6 represent what we estimate is achievable in alignment and field quality of elements in the machine. To further analyze the tolerances of these various errors, we use the procedure in Tab. 2.1.7, which leads to the allowable errors in Tab. 2.1.6. These rms limits are determined by allowing a 10% increase in the projected emittance or beam size, or allowing a 10% of the correctors to have more than 0.5 mrad maximum angles.

For example, we find that *in addition to all of the baseline errors*, if we further misalign all quadrupole horizontal positions by $300 \mu\text{m}$, then the horizontal corrector strengths C_x needed to correct such errors is unacceptably large. Because the baseline quadrupole horizontal offset was already $120 \mu\text{m}$, this means that this unacceptably misaligned machine actually has rms quadrupole offsets of about $\sqrt{120^2 + 300^2} \mu\text{m} \approx 323 \mu\text{m}$.

Statistics for emittance and beam size at all undulators for mode B, from $N = 100$ randomly misaligned ERLs, are shown in Fig. 2.1.59. These values should also apply to mode A, because mode B uses the same optics but has a smaller initial emittance. Note that the jump in horizontal emittance from undulator 9 to undulator 10 is almost entirely due to ISR in the CE section, as previously suggested in Fig. 2.1.35. Analysis of mode C is still in progress.

Table 2.1.6: Errors considered in ERL simulations for the low emittance mode B. Baseline numbers are rms values with a cutoff at 3 times his value. The symbols C_x and C_y denote horizontal and vertical corrector strengths, respectively. The symbol+ indicates the maximum rms error simulated, without significant effect. OC indicates the failure of the orbit correction algorithm.

Error	Unit	Baseline (1σ)	Allowable (1σ)	Primary effect
Quadrupole x offset	μm	120	300	C_x
Quadrupole y offset	μm	100	250	C_y & OC
Sextupole x offset	μm	120	300	σ_y
Sextupole y offset	μm	100	200	ϵ_y & σ_y
Cryomodule quad x & y offset	μm	300	1600	C_x & C_y
Dipole roll	μrad	80	1000	ϵ_y
Quadrupole roll	μrad	80	200	ϵ_y
Dipole x & y pitch	μrad	80	5000+	ϵ_y
Quadrupole x & y pitch	μrad	80	1000+	ϵ_y
Acc cavity x & y offsets	μm	500	2000	σ_y & OC
Acc cavity x & y pitch	μrad	1000	1500	ϵ_x & ϵ_y & OC
Acc cavity gradient	relative	10^{-4}	60×10^{-4}	σ_y
Acc cavity ϕ_{rf}	degree	0.1	1.0+	σ_y
Dipole chain field	relative	10^{-4}	10×10^{-4} +	
Quadrupole k_1	relative	10^{-4}	5×10^{-4}	σ_y
Sextupole k_2	relative	10^{-4}	10^{-3} +	

Table 2.1.7: Tolerance analysis procedure. Typically this procedure is iterated for $N = 100$ times.

Step	Procedure
1	Initialize design lattice
2	Calculate orbit and dispersion response matrices
3	Enable synchrotron radiation losses and fluctuations
4	Perturb the lattice with all of the baseline errors listed in Tab. 2.1.6
5	Additionally perturb the property to be analyzed
6	Apply the SVD orbit correction algorithm
7	Save this perturbed lattice
8	Track particles through, and save statistics at all undulators
9	Reset the lattice
10	Repeat steps 4-9 N times

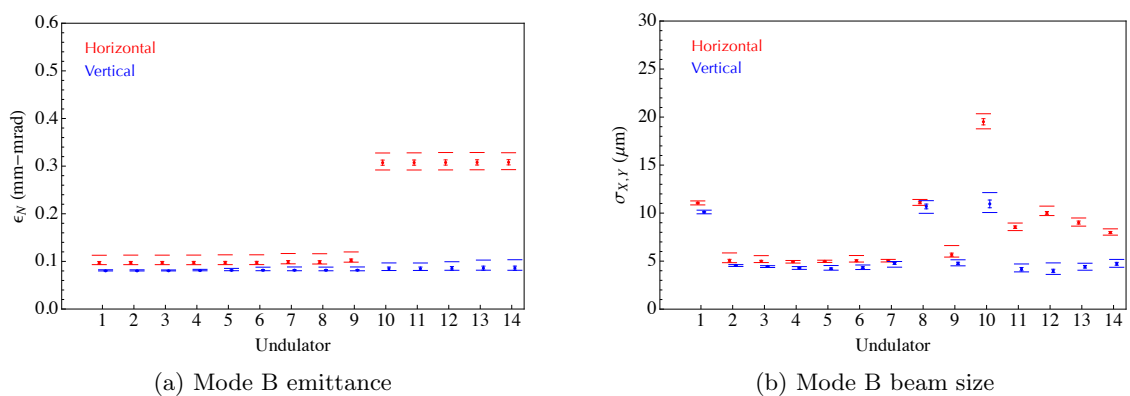


Figure 2.1.59: Statistics for $N = 100$ randomly misaligned ERL lattices, after orbit correction, at all of the undulators. Mean values are shown as dots, with attached error bars at one standard deviation. The maximum and minimum values encountered are shown as separated long bars. It is apparent that the standard errors hardly damage the emittance.

Full simulation

Table 2.1.8: Relevant start to end simulation parameters.

Parameter	mode A	mode B	mode C	unit
$\epsilon_{N,x}$ injected	0.29	0.11	0.19	mm mrad
$\epsilon_{N,y}$ injected	0.24	0.10	0.14	mm mrad
σ_z/c injected	2.11	1.52	1.00	ps
σ_δ injected	1.66	0.66	1.17	10^{-4}
ϕ_{rf} for LA and LB	0	0	6.6	degree

To perform full simulations for the ERL, favorable particle distributions are chosen from Fig. 2.1.11 to represent realistic bunches at the end of the first cryomodule in LA. Some relevant properties of these bunches are listed in Tab. 2.1.8. Note that these properties deviate somewhat from the design values in Tab. 1.3.1.

For modes A and B, particles are then tracked through the remainder of the machine with Bmad using a misaligned (and orbit and dispersion corrected) lattice, according to the baseline errors in Tab. 2.1.6. Mode C is tracked using an unperurbed lattice, because the full error analysis for this mode is not yet complete. The resulting emittance and bunch durations at all undulators are shown in Fig. 2.1.60.

In particular, the plot in Fig. 2.1.60a is consistent with Fig. 2.1.59, and shows that the emittance growth is well controlled everywhere except for the CE section between undulators 9 and 10. For modes A and B, the usage of the more ‘realistic’ bunches from GPT incur no additional effects over the more simple Gaussian bunches used in the orbit correction and tolerance simulations. The compressed bunch duration of mode C particles in Fig. 2.1.60b is approximately 120 fs, but this is likely can be shortened to 100 fs by minor changes in r_{56} and/or the accelerating phase, as suggested in §2.1.10. Figure 2.1.61 shows the transverse phase space at the center of the first undulator for the emittance sensitive modes A and B.

Finally, it must be checked that these particles have an acceptable energy spread after deceleration, just prior to the demerger before the beam stop. Figure 2.1.62 shows δ distributions for all three modes, all of which have an rms energy spread of $\sigma_\delta \approx 3\%$. All particles simulated lie completely within $\delta = \pm 15\%$.

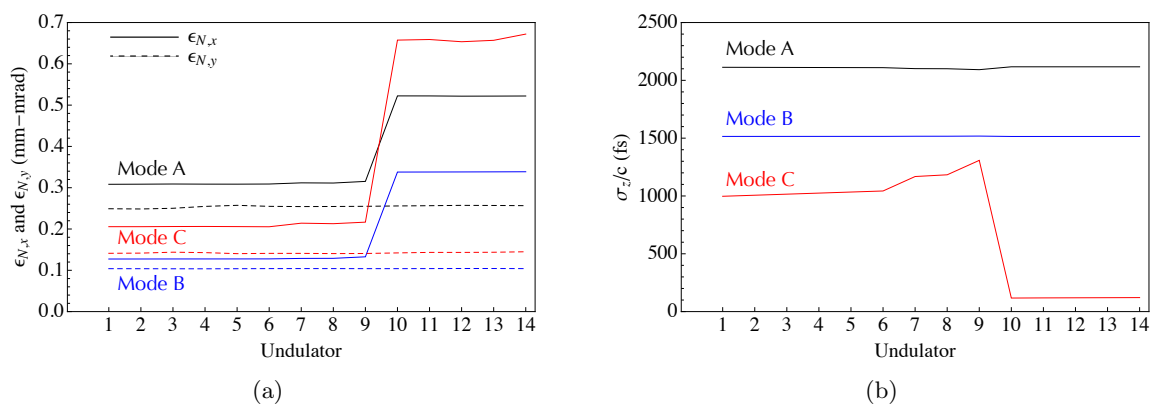


Figure 2.1.60: Emittances and bunch durations for all of the ERL operating modes. Particles are generated from the laser pulse on the cathode, and simulated through the end of the first LA cryomodule using the code GPT (see §2.1.4). These particles are then imported into Bmad, with properties listed in Tab. 2.1.8, and tracked through a lattice that has been misaligned (and orbit and dispersion corrected) according to the baseline errors in Tab. 2.1.6.

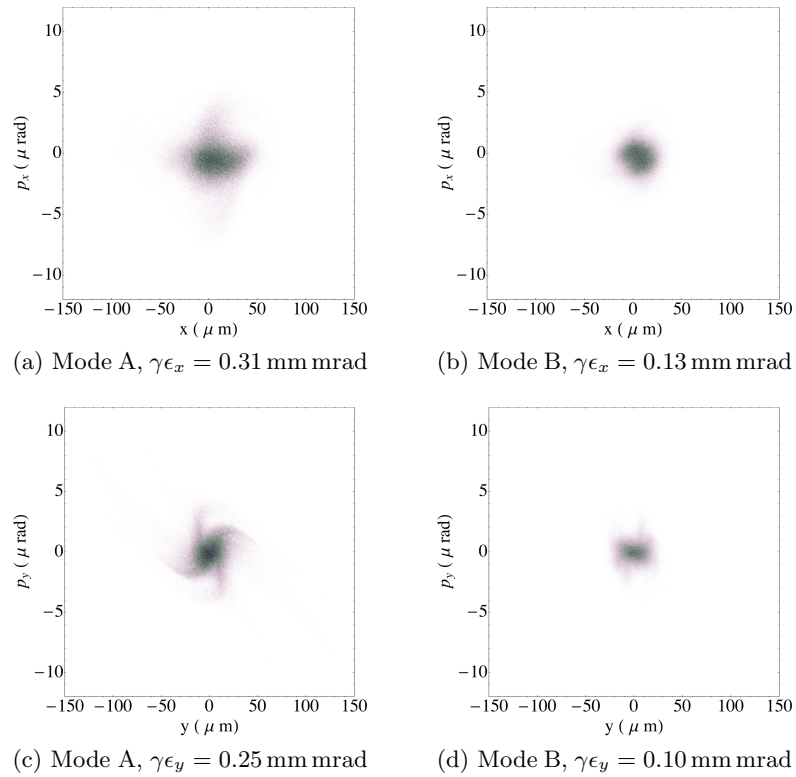


Figure 2.1.61: Transverse phase-space distributions at the center of undulator 1 for modes A and B. These plots are the result of splicing the 200,000 particle output of GPT (with parameters listed in Tab. 2.1.8) with a misaligned and orbit corrected Bmad lattice.

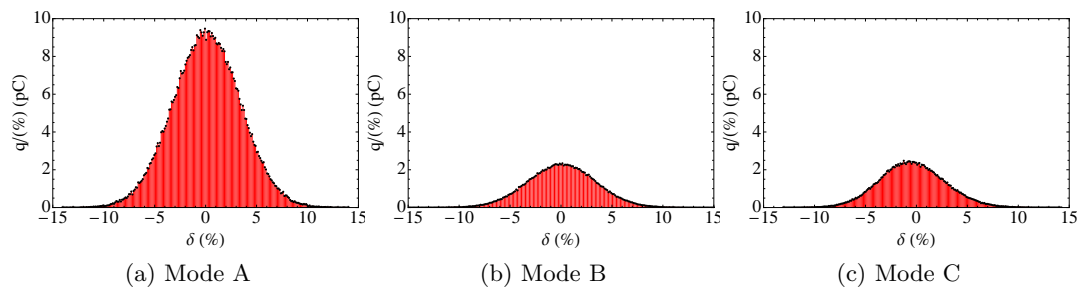


Figure 2.1.62: Final relative energy distributions just prior to demerger before the beam stop. The reference energy is 10 MeV. The standard deviation of δ for all modes is approximately 3%.

2.1.16 Beam instabilities

Introduction

Beam-breakup (BBU) instabilities of several varieties impose operational current limitations on energy recovery Linacs and other types of recirculating linear accelerators. In recent years the continuous-wave theory for recirculating Linacs [46] has been extended to energy-recovery Linacs and quantitative studies of mitigating effects have been published [47].

Transverse dipole BBU

Transverse dipole BBU instabilities arise from the one-turn T_{12} term coupling beam displacement and kick in the RF cavities. Like the longitudinal and quadrupole instabilities described below, the transverse dipole instability thresholds have been calculated using the detailed lattice analysis and design software package Bmad developed at Cornell for CESR and other projects. An approximation to the threshold current in the case of a single HOM in a single cavity is given by

$$I_{\text{th}} = -\frac{\omega_\lambda}{e \left(\frac{R}{Q}\right)_\lambda Q_\lambda} \frac{1}{T_{12}^* \sin \omega_\lambda t_r} T_{12}^* = T_{12} \cos^2 \theta_\lambda + \frac{T_{14} + T_{32}}{2} \sin 2\theta_\lambda + T_{34} \sin^2 \theta_\lambda \quad (2.1.19)$$

where $(R/Q)_\lambda$ is the shunt impedance, Q_λ is the quality factor, θ_λ is the polarization angle from the x direction, ω_λ is the HOM frequency, t_r is the bunch return time, e is the elementary charge and the matrix \mathbf{T} describes how transverse momentum is transported to a transverse displacement after one turn.

A validation of the Bmad tracking calculation for a simplified case of the ERL optics is described in [48]. The Bmad tracking code is used to compute the BBU threshold current for the HOMs of a preliminary cavity design, shown in Tab. 2.1.9. The frequency spread for HOMs of different cavities must be made as large as $\sigma_f = 10$ Mhz to obtain the large threshold currents shown in Fig. 2.1.63. To obtain a trustworthy estimate of the threshold current, we compute it for 120 random seeds for the HOM frequency spread and use the average and rms values of the results as judgement criteria. The average single-turn instability threshold is $I_{\text{th}} = 1083$ mA with an rms spread of $\sigma_{I_{\text{th}}} = 127$ mA. The worst case of 700 mA provides a factor of seven margin over the ERL design current. Subsequently we varied the cavity geometry to further increase a) the threshold current and b) the insensitivity to cavity production errors.

Table 2.1.9: Higher-order-mode parameters from the optimized cavity design, used in the BBU threshold modeling

HOM	f_λ (MHz)	Q_λ	R/Q (Ω/cm^2)
1	1708.4	826	5.7932
2	1856.3	2781	2.8852
3	1870.8	3539	4.0064
4	2552.3	1579	7.7736
5	3078.9	93360	0.3617

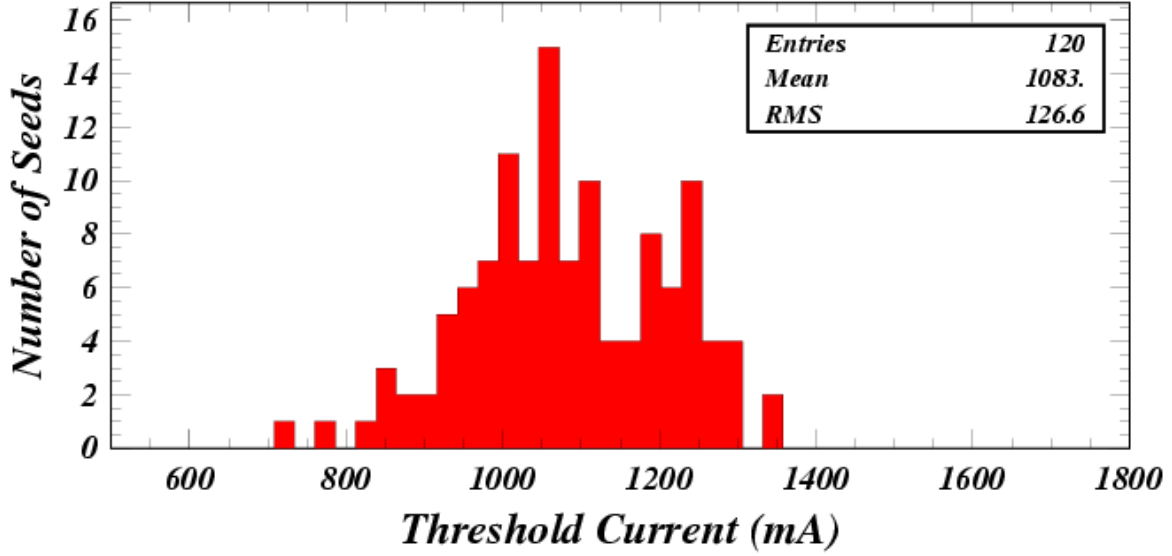


Figure 2.1.63: Modeled BBU instability thresholds for the case of the five HOMs in Tab. 2.1.9 excited in each cavity of the full ERL 7.4 optics. A HOM frequency spread of 0.33% was introduced, re-randomized for each of the calculations.

The resulting optimized cavity shape is shown in §2.4. With realistic, cylindrically-symmetric construction errors of up to 1/8 mm, this cavity design shows a threshold current of 450 mA. For these simulations, the HOM parameters are implemented in all cavities, and a randomized HOM frequency spread of 0.33% of the HOM frequency is applied to each calculation.

One means of mitigating the beam breakup effect even further is to introduce an X-Y coupling in the optics and to polarize the HOMs in the cavities. To calculate the degree of improvement which can be obtained, a coupling element was introduced between the Linacs and polarized HOMs were implemented in each cavity. For the cavities used in this study, X-Y coupling increased the threshold current from about 400 mA to 2200 mA [47]. This means of BBU instability mitigation can provide an additional margin of about a factor of five. No specific plan to implement such a mitigation technique is being developed, since the BBU instability limit is sufficient without it, polarized cavities are more difficult to produce, and there is little operational experience with such cavity designs.

Transverse quadrupole BBU

Quadrupole HOMs can be excited by beams with a nonzero quadrupole moment. Their effect is to distort the linear optics by providing additional focusing. The threshold current due to a quadrupole kick at position 1 acting at position 2 for a single HOM with frequency ω_λ , shunt impedance $\frac{R}{Q}_\lambda$ and quality factor Q_λ in a single cavity can be approximated by

$$I_{th} = - \frac{\omega_\lambda \gamma E_e}{2 \frac{ec}{r_0^4} \left(\frac{R}{Q} \right)_\lambda Q_\lambda \epsilon_n} \frac{1}{(\beta_{x1} \beta_{x2} \sin 2\Delta\psi_x + \beta_{y1} \beta_{y2} \sin 2\Delta\psi_y)} \frac{1}{\sin \omega_\lambda t_r} \quad (2.1.20)$$

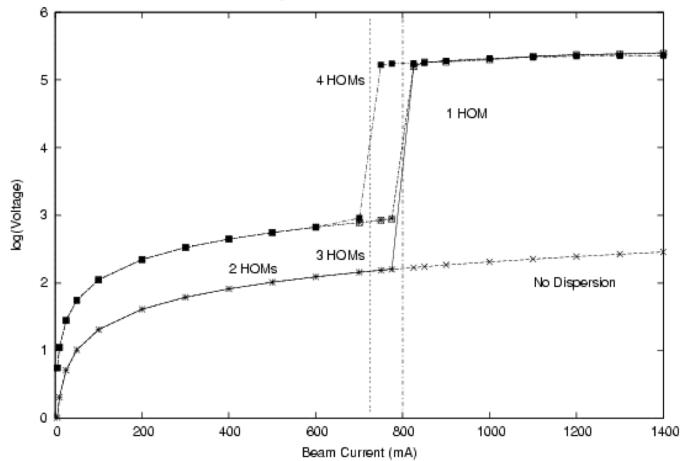


Figure 2.1.64: B.1 49: Longitudinal higher-order mode excitation voltage versus beam current as calculated in [50]

where E_e is the beam energy, ε_n is the normalized emittance, and r_0 is the radius where $\left(\frac{R}{Q}\right)_\lambda$ is measured. The $\Delta\psi$ values are the differences in betatron phase and t_r is the time difference between positions 1 and 2.

Such instabilities have been studied in [49] for typical HOM parameters and for the beam quadrupole moment derived from the difference of horizontal and vertical beta functions in the ERL linear optics. The instability threshold current was found to be above 200 mA as long as the HOM Q_λ is less than about half of the cavity Q_0 for the fundamental mode.

Longitudinal BBU

Longitudinal instabilities can be caused by excitation of longitudinal higher-order modes (HOMs) in the RF cavities by the beam bunches. The time-of-flight term r_{56} plays an important role in the excitation of such instabilities, since the main effect of the longitudinal HOM is to change the bunch energy. These instabilities have been studied in [50]. Figure 2.1.64 shows the limits obtained for various HOM configurations in an ERL lattice model. The conclusion of this study is that instability threshold level will far exceed the ERL design operating current of 100 mA as long as the magnitude of r_{56} is well below 10 m. The threshold current is inversely proportional to r_{56} and increases with HOM frequency spread in the cavities as well. For nominally isochronous lattice of the recirculating arc ($r_{56} \approx 0$ for all operating modes), the longitudinal BBU poses no threat.

2.1.17 Collimation

During operation of any high-energy accelerator, particles are lost along the beam transport. There are several processes that produce beam halo and electron loss in the Cornell ERL. Two dominant and unavoidable mechanisms are Touschek scattering and electron scattering off residual gas nuclei. Of the two, Touschek scattering is by far the dominant process but rest-gas scattering dominates losses in the vertical plane. Although the fraction of electrons lost is typically less than 5×10^{-6} , this loss has non-trivial consequences.

The beam loss due to these mechanism has been simulated to place collimators effectively to perform two essential functions. One is to protect areas occupied by personnel or sensitive equipment, and the other is to protect insertion devices. The 5 GeV electrons intercepted by the collimators generate an electron-photon cascade, and the energetic neutrons and photons produced in the cascade create a radiation hazard. Accordingly, the design of collimators is such as to reduce the resulting radiation field as much as possible in the vicinity of the lost particles. This in turn ensures that shielding walls of a reasonable thickness can be used to reduce radiation exposure in areas occupied by personnel to safe workplace levels. Based on 2000 hours of occupancy per year, these are 100 mrem/y for visitors, and 500 mrem/y for radiation workers (see §4.6.4).

Protection criteria for insertion devices are based on 5000 hours of operation per year, and are discussed in more detail below. The design of the various collimators was evaluated using the extended many particle Monte Carlo code MCNPX v.27d [51] and further details are discussed in [52].

Touschek scattering

Collisions among particles within a bunch can change their trajectories so much that they are transported to large amplitudes and constitute a beam halo, or are lost at the vacuum pipe. This loss mechanism is referred to as Touschek scattering. Bremsstrahlung is produced when the particles collide with the beam pipe, and collimators have therefore been designed to avoid radiation hazards to hardware and personnel. These collimators are placed in the tunnel and away from x-ray user regions. Relatively small losses can damage the permanent magnets of undulators and a protector device is therefore placed in front of every undulator.

To determine where collimators are to be placed, Touschek scattering has been simulated and the trajectories of scattered particles were followed to their loss point. These simulations are based on [53] and [54], which has been validated in storage-ring-lifetime measurements [55]. Following scattered particles shows where a collimator will intercept most particles which would otherwise be lost in sensitive regions, and it was also studied where these particles have scattered so that the beam optics in these regions can be changed to minimize Touschek scattering.

2.1.18 Gas scattering

Residual-Gas Scattering (RGS) refers to a beam-loss process resulting from electron collisions with residual gas molecules in the beam pipe. To avoid that resulting loss of beam particles along the chamber walls pose a hazard to hardware or personnel, it has been studied whether the ERL's collimators manage these losses adequately. It is found that RGS contributes about

Table 2.1.10: Touschek losses for protectors P and collimators M shown in Fig. 2.1.65

Protector	P2	P3	P4	P5	P6	P7	P8	P9	P10	P11	P12	P13	P14
I(pA)	0	0	0.01	0.37	0.18	46	147	58	1360	0.01	0.04	0.09	0.14
Collimator	M1	M2	M3	M4	M5	M6							
I(nA)	31.7	7.85	110	163	136	2.17							

0.2% of the total flux of lost particles, while Touschek-losses contribute 99.8% [56] for ERL parameters. However, while Touschek scattering leads to particle losses in the horizontal plane, rest-gas scattering produces losses in every direction. This is due to the fact that rest-gas scattering changes the electron trajectory with equal likelihood in any direction, whereas Touschek scattering mostly changes the energy of scattered particles, and particles with change energy are bent incorrectly in the horizontal plane by subsequent magnets.

RGS is well-understood and experimental observations in storage rings are documented at [57, 58]. Equations for the scattering cross-section are available at [59]. These show that even at the very low pressures of the ERL beam pipe, the rate of collisions between beam particles and gas particles will be high enough to require detailed studies. A simulation was used that generated scattered particles according to the rest-gas scattering cross section at every step along the accelerator and follows these particles to where they are lost. This shows whether collimators are suitably placed and whether protectors shield undulators adequately.

It is worth noting that the simulation methods and collimation techniques applied to RGS have much in common with those used for Touschek losses. Both RGS and Touschek losses are due to single-event scattering processes that change the phase-space coordinate of the colliding particles, resulting in particle loss downstream of the scattering event. Both processes can be succinctly described by distribution functions that give the rate at which particles with perturbed phase-space coordinates are generated. Finally, the primary method for mitigating the detrimental effects of each process is the strategic placement of collimators. We therefore employ a unified method to model halo production and collimation that can be extended to further processes that add to the beam halo.

Another method for mitigating RGS would be a lowering of the gas pressure to below the average rate of 1 nTorr that has been used for this report. Additional vacuum pumps would have to be installed in regions where the scattering rate is high.

Collimator layout

The overall layout of the collimators in the ERL as determined by simulation is shown in Fig. 2.1.65. The Touschek-current intercepted by each of these collimators is given in Tab. 2.1.10. The ‘P’ collimators protect undulators, while the ‘M’ collimators remove larger currents. The two types of collimators are discussed separately. A typical probability distribution of Touschek particles as a function of position incident on a protector/collimator is shown in Fig. 2.1.66

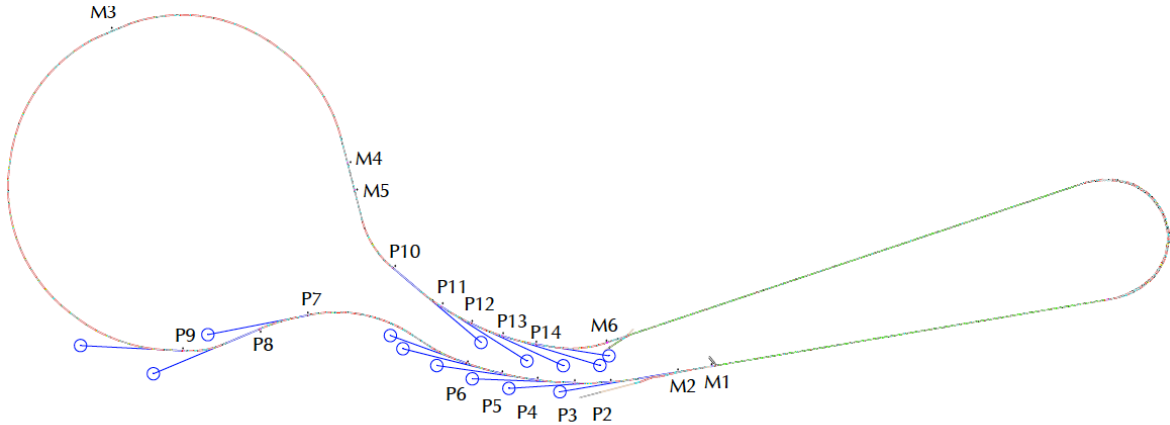


Figure 2.1.65: ERL protector and collimator layout

Undulator protectors

Undulator protectors P2 through P6 are in the south arc, while P11 through P14 are in the north arc. (See Fig. 2.1.65.) In the south arc the protectors are located in the space bounded by shielding walls, while in the north arc (NA), the space is bounded by a shielding wall and the hillside to the north. The maximum current loss in this region is less than 0.37 pA. Undulator protectors P7 and P9 are located within a space bounded by shielding walls inside the Wilson Lab experimental hall. Undulator protector P9 is located within the CESR tunnel, and P10 is located in the underground tunnel joining CESR and the north arc.

Undulator protector design

The radiation field in the vicinity of the protector is dominated by bremsstrahlung. Accordingly, the general design criteria for the undulator protectors (and collimators) are based on the following. In passing through matter, electrons lose energy by radiation in collisions with atomic nuclei and electrons, and by ionizing collisions with atoms. At energies greater than the critical energy, E_c , energy loss by radiation dominates. E_c is approximately given by [60]

$$E_c = \frac{800}{Z + 1.24} \text{ MeV} \quad (2.1.21)$$

where Z is the pertinent atomic number. In the high energy limit, where the initial electron energy E_o is very much greater than the electron rest mass, $m_e c^2$, the electron energy is reduced by a factor of $1/e$ in a distance X_o , called the radiation length, and given by [60]

$$X_o = \frac{716 A}{Z(Z + 1) \log(287 Z^{1/3})} \text{ g/cm}^2 \quad (2.1.22)$$

and where Z and A are the atomic number and weight. Most of the energy is carried away by energetic photons. These have large pair production cross-sections, and the photon energy is shared equally by the electron and positron produced. The electrons and positrons in turn

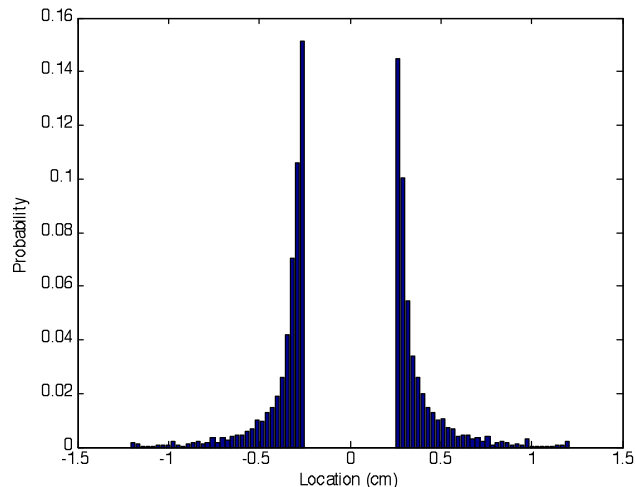


Figure 2.1.66: Typical probability distribution of Touschek particles as a function of position incident on a protector/ collimator

create more photons, which again produce electron positron pairs, and the process keeps on cascading until emission of energetic photons and pair creation can no longer take place.

The cascade process takes place in the same way in all materials if the thickness is measured in units of the radiation length X_o . For an initial electron energy E_o , the shower reaches a maximum at X_{max} where [61]

$$X_{max} = 1.01 \left[\log \left(\frac{E_o}{E_c} \right) - 1 \right] X_o. \quad (2.1.23)$$

The angular spread of the cascade shower is not large since at high energies both photon emission and pair production are directed forward, along the direction of the incident electron. The Moliere radius X_M characterizes the radial distribution of the cascade shower. X_M is given by[60]

$$X_M = \sqrt{\frac{4\pi}{\alpha}} \left(\frac{m_e c^2}{E_c} \right) X_o \quad (2.1.24)$$

where α is the fine structure constant.

In a given material characterized by radiation length X_o , 99% of the electron energy is deposited in a cylinder that is infinitely long, and $7X_M$ in diameter. [62] Accordingly, the diameter of the basic collimator is taken as $7X_M$. The collimator length depends on several factors. For 5 GeV electrons, the shower maximum ranges from $3.6X_o$ to $5.4X_o$ for the materials listed in Tab. 2.1.11. The distance traversed by an electron in order to reduce its energy from 5 GeV to E_c ranges from $4.6X_o$ to $6.3X_o$ for the same materials. Finally, the most penetrating photon shower component has energies near the Compton minimum ($E_{Compt.min}$) in the photo-absorption cross section. Again, for the materials listed in Tab. 2.1.11, the mean free path for these energetic photons ranges from $1.9X_o$ to $3.8X_o$. Based on these considerations one would expect a collimator length of $10-15X_o$ to be reasonable.

Table 2.1.11: General properties of possible shielding materials. Note that X_o and $X_{\text{showermax}}$ are measured here in cm.

Property	Element						Unit
	Al	Fe	Cu	Ta	W	Pb	
Density	2.70	7.87	8.96	16.65	19.3	11.35	g/cm^3
E_c	51.0	27.4	24.9	10.4	10.2	9.51	MeV
X_o	8.9	1.76	1.44	0.41	0.35	0.56	cm
$X_{\text{showermax}}$	32	7.5	6.2	2.1	1.8	3.0	cm
$\left(\frac{\mu}{\rho}\right)_{\text{Compt.min}}$	0.0215	0.0296	0.0304	0.0399	0.0403	0.0419	g/cm^2
$E_{\text{Compt.min}}$	22	9.0	8.4	3.7	3.7	3.6	MeV

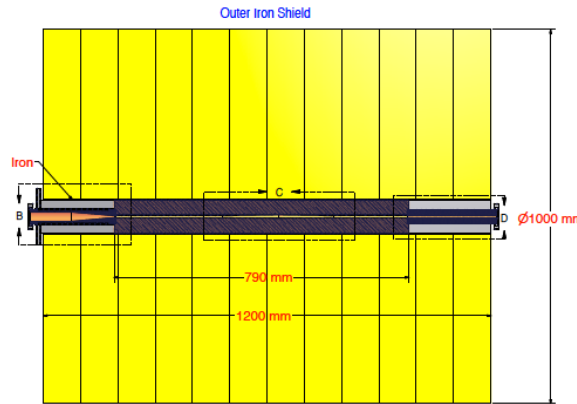


Figure 2.1.67: Cross section of protector

However, attenuation of photons is not the only concern. Energetic bremsstrahlung photons interacting with matter can also produce neutrons, protons, μ^\pm , and π^\pm mesons. Of particular shielding concern are photo-neutrons produced by 10–20 MeV photons via the giant dipole resonance mechanism.

The choice of collimator material thus depends not only on how well it attenuates photons and neutrons, but also on its activation tendency by neutrons, determined by the pertinent neutron reaction energy thresholds, neutron cross sections and resulting radionuclide half-lives. Attenuation of both photons and neutrons adds considerable mass to the basic collimator design. General properties of various possible shielding materials are shown in Tab. 2.1.11

A number of undulator protector designs were investigated. The undulator protectors are of the general form shown in Fig. 2.1.67.

Neutron and gamma shielding properties of the protector were investigated using MC-NPX. The input geometry is cylindrically symmetric, of cross sections and dimensions shown in Fig. 2.1.68. 5 GeV electrons with the probability distribution shown in Fig. 2.1.66 and directed along the x-axis of the collimator specified the incident particle source. In the calculations, particle tracks were terminated at 4.7 MeV for electrons, and 1.0 MeV for photons.

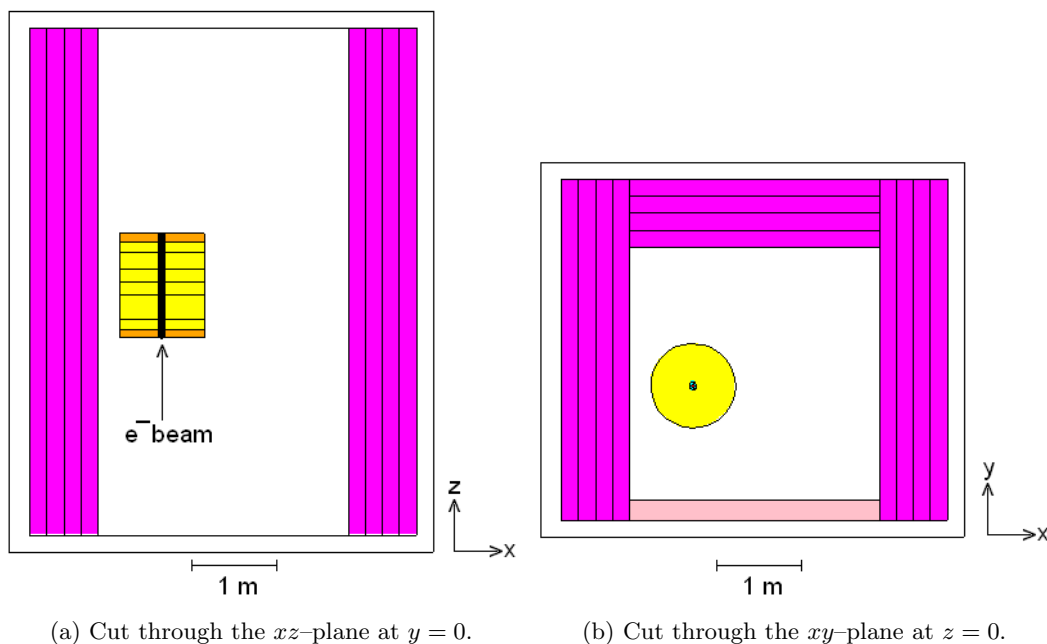


Figure 2.1.68: MCNPX input geometry to calculate neutron and photon dose rates. The center of the protector is at $(x, y, z) = (0, 0, 0)$. The electron beam propagates in the $+z$ -direction. Yellow is iron, orange is lead, purple is heavy concrete, and pink is ordinary concrete.

Neutrons were followed down to 0.001 MeV. Typically, 5×10^5 particles were run to provide a relative tally error of less than 0.10. Standard flux and mesh tally data (normalized per starting particle) provided the required information. In MCNPX, the standard F2 tally records the number of particles of all energies (either photons, neutrons, or electrons) that cross a given surface, and tallies the average fluence (particles/cm²/incident particle). Similarly, the F6 tally records the energy deposited by particles averaged over a cell (MeV/g/incident particle).

In addition to the standard tallies, the mesh tally capability of MCNPX provides a means for graphically displaying particle flux, dose or other quantities on a rectangular, cylindrical or spherical mesh overlaid on the protector/collimator geometry. (To get the dose, the flux is modified by an energy dependent dose function.) The dose functions used for neutrons and photons in these calculations are the ICRP-21 1977 values. A more detailed comparison of the different and more recent AMSI/ANS standard dose functions will be carried out later.

Personnel protection

Figure 2.1.68 shows outlines of the MCNPX input geometry. Figure 2.1.69 and Fig. 2.1.70 show the neutron dose rate contours (rem/h)/(el/s) in the xz - and xy - planes through the center of the protector at $(x, y, z) = (0, 0, 0)$. From the figure, the contour at the outer surface of the 80 cm thick, heavy concrete shielding wall is 1.0×10^{-14} (rem/h)/(el/s), and similarly for the photon dose rate, Fig. 2.1.71 and Fig. 2.1.72. The largest current, 0.37 pA, lost in

the north and south arc areas is on protector P5. For 2000 hours/year occupancy in the immediate vicinity of the shielding wall, this corresponds to a total annual dose of 0.1 mrem due to neutrons and gammas.

Protector P8 intercepts 147 pA, and for 2000 hours/year occupancy gives a total annual dose of 37 mrem due to neutrons and gammas. Protectors P7 and P8 give a total annual dose of 12 and 15 mrem due to neutrons and gammas. Protector P10 which intercepts the largest current, 1360 pA, is located in the tunnel between CESR and the north arc, and as such does not pose a hazard to personnel.

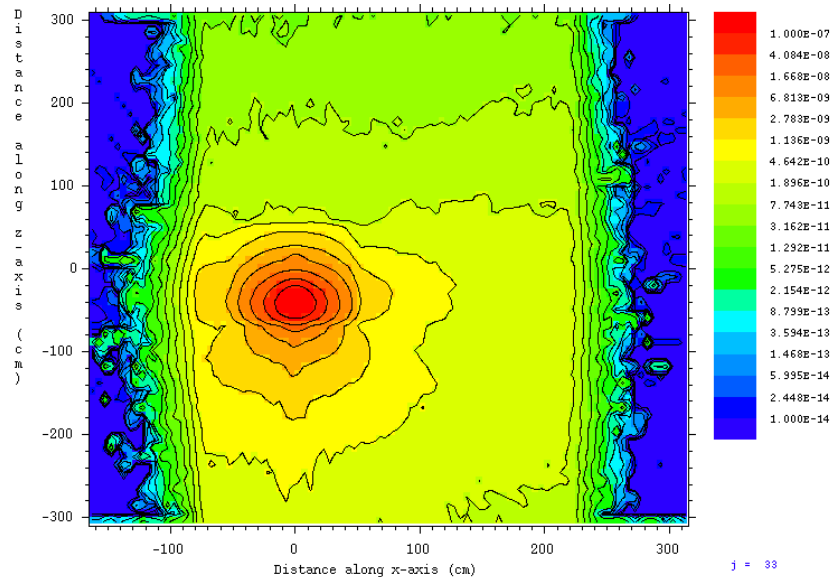


Figure 2.1.69: Neutron dose rate contours in (rem/h)/(el/s) in the xz -plane at $y = 0$, (electron beam line), through the undulator protector. Electron beam enters from the bottom of the figure.

Undulator protection

The undulators (described in §2.7) are located 0.72 m downstream from each protector. The dose rates in the xy -plane at 0.72 m are 3×10^{-11} (rem/h)/(el/s) for neutrons, and 10^{-12} (rem/h)/(el/s) for photons (except for the intense central plume ≈ 20 cm wide which has a peak value of 3×10^{-10} (rem/h)/(el/s)) (see Fig. 2.1.71). All attempts to reduce this plume by various collimator designs proved unsuccessful (the plume is due to small angle electron and photon scattering in the vicinity of the 5 mm diameter collimator hole).

Protector P10 intercepts 1360 pA. Assuming 5000 h of operation per year, this corresponds to a neutron dose of 1300 rem/y. Outside the plume the gamma dose is 43 rem/y, however, in the vicinity of the beam line it is 13,000 rem/y.

The intervening space between the protector and undulator contains drift regions, a gate valve, slits, and a weak dipole magnet. The effect of the forward gamma radiation ‘plume’ on the NdFeB magnets in the undulator was modeled as shown in Fig. 2.1.73 A section of the delta undulator NdFeB permanent magnet assembly is represented by a 1 m long cylinder,

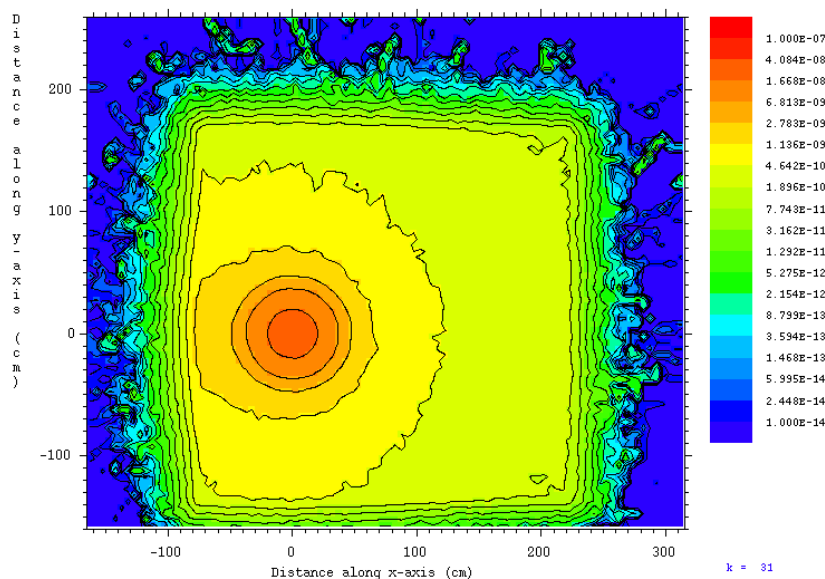


Figure 2.1.70: Neutron dose rate contours in (rem/h)/(el/s) in the xy -plane at $z = 0$ through the undulator protector.

2.54 cm in diameter with a 0.5 cm diameter hole through it. The cylinder is broken up into 10 cells, each 10 cm long, and MCNPX tally 6 is used to calculate the MeV/g/electron deposited by neutrons and photons in each cell.

An average value of 7.6×10^{-6} MeV/g is deposited by photons in the first 20 cm long section of the undulator magnets, and the energy deposited decreases by a factor of ten in each subsequent 10 cm section. The largest current intercepted by protector P10 is 1360 pA. This corresponds to 6.45×10^4 Mev/g/s, or 1.03×10^{-5} J/kg/s. In 5000 hours of operation, to 186 J/kg or, an annual dose of 1.86×10^4 rad in the first 10 cm of the NdFeB magnet assembly. The neutron dose is a factor of 2400 times smaller.

Demagnetization of NdFeB permanent magnet material by radiation is of concern in the design of insertion devices. However, the change in the magnetic moment of the material as a function of dose depends very much on the quality of the material. For example, [63] has measured only 1% demagnetization dose of 11.3Mrad in V block type, N40SH NdFeB permanent magnet material. Thus, assuming a 20 year lifetime of the insertion device and an annual dose of 18.6krad, the total dose over the first 20 cm or so of the device over the lifetime is well within the 1% demagnetization limit.

M type collimators

Collimators M1 through M6 remove larger Touschek losses. M1 and M2 are located in the tunnel near the entrance to the south arc, M3 is located in CESR, M4 and M5 are in the tunnel joining CESR to the north arc and M6 is in the tunnel near the injector. Due to their location, these collimators do not present a direct hazard to personnel; however, the intense radiation fields pose a problem to electronics in the vicinity, and appropriate steps

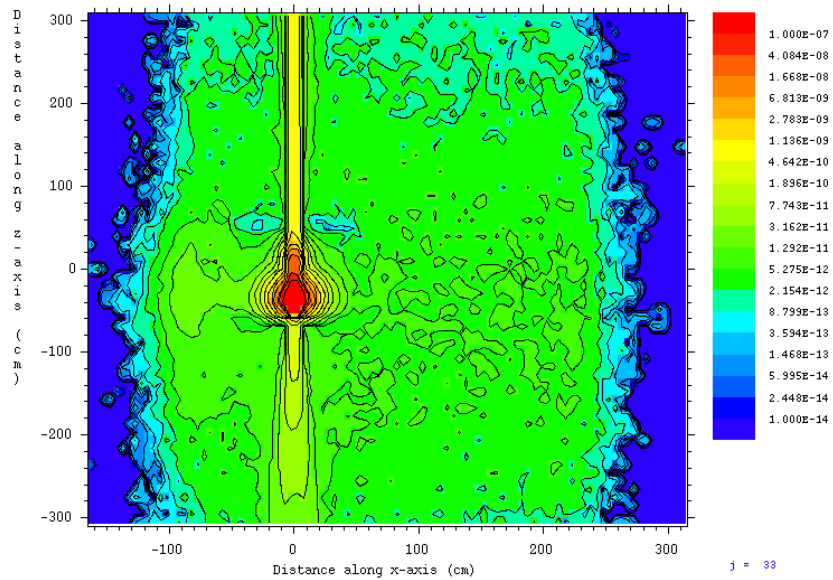


Figure 2.1.71: Photon dose rate contours in (rem/h)/(el/s) in the xz -plane at $y = 0$, (electron beam line), through the undulator protector. Electron beam enters from the bottom of the figure.

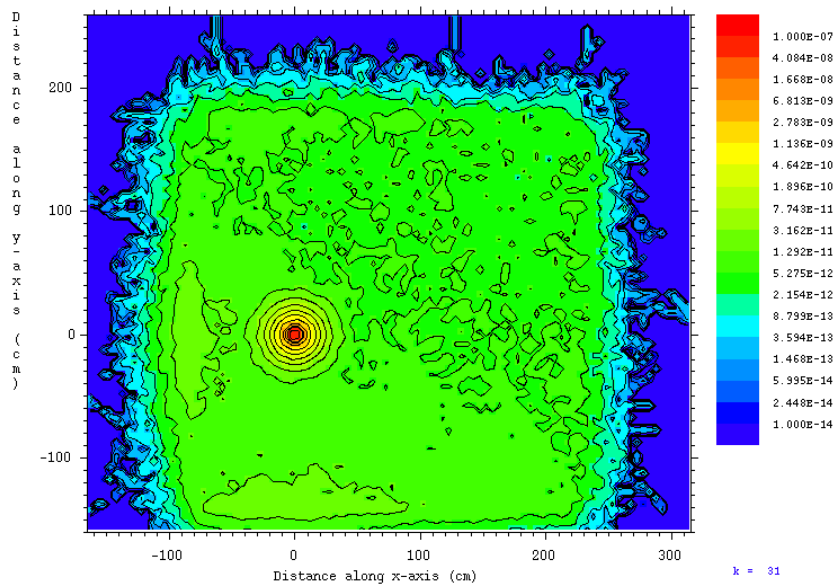


Figure 2.1.72: Photon dose rate contours in (rem/h)/(el/s) in the xy -plane at $z = 0$ through the undulator protector.

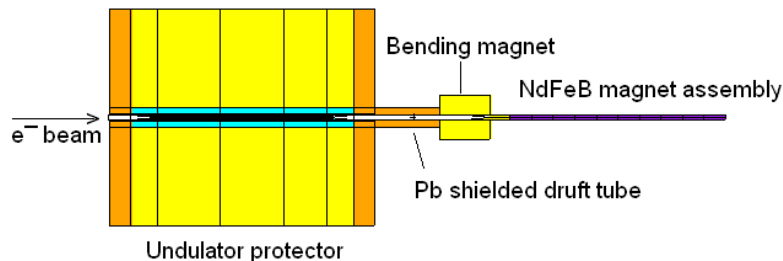


Figure 2.1.73: MCNPX input geometry to calculate the dose to NbBFe permanent magnets in the undulator. The beam pipe between the protector and the the weak solenoid is shielded with lead. an iron cylinder represents the weak bend magnet in front of the undulator magnet assembly

to shield the electronics will be taken. The collimator design is shown in Fig. 2.1.74 (see also §2.2.4 for details). The neutron and photon dose rates were calculated using MCNPX as described above for undulator protectors. The collimator in the tunnel input geometry is shown in Fig. 2.1.75 and the resulting dose rate contours are similar to those shown in Fig. 2.1.69 through Fig. 2.1.72. The calculated neutron dose rate 1 m downstream from

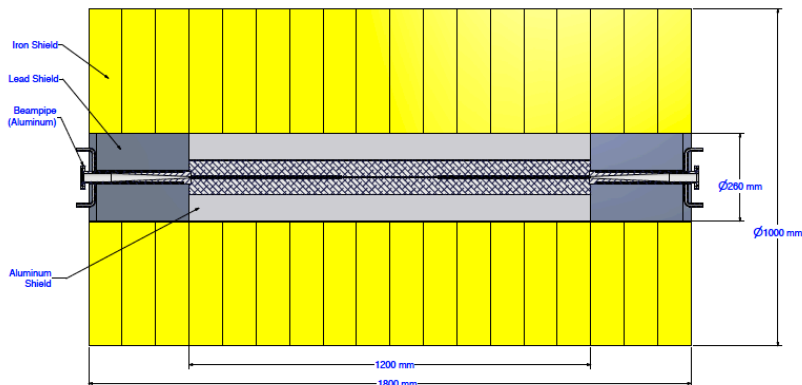


Figure 2.1.74: M type collimator. The top picture shows the overall collimator with iron shield (yellow),

the M collimator in the xy -plane is 7×10^{-12} (rem/h)/(el/s). Collimator M4 intercepts the largest current, 163 nA. Assuming 5000 h of operation per year, this corresponds to a total annual dose of 36,000 rem. Similarly the average photon dose rate 1 m downstream from the M collimator in the xy -plane is 4×10^{-13} (rem/h)/(el/s), and 2.5×10^{-10} (rem/h)/(el/s) in the central, 20 cm wide plume. Again, assuming 5000 hours of operation per year, the total annual dose is 2040 rem outside the plume and 1.3×10^6 rem in the plume.

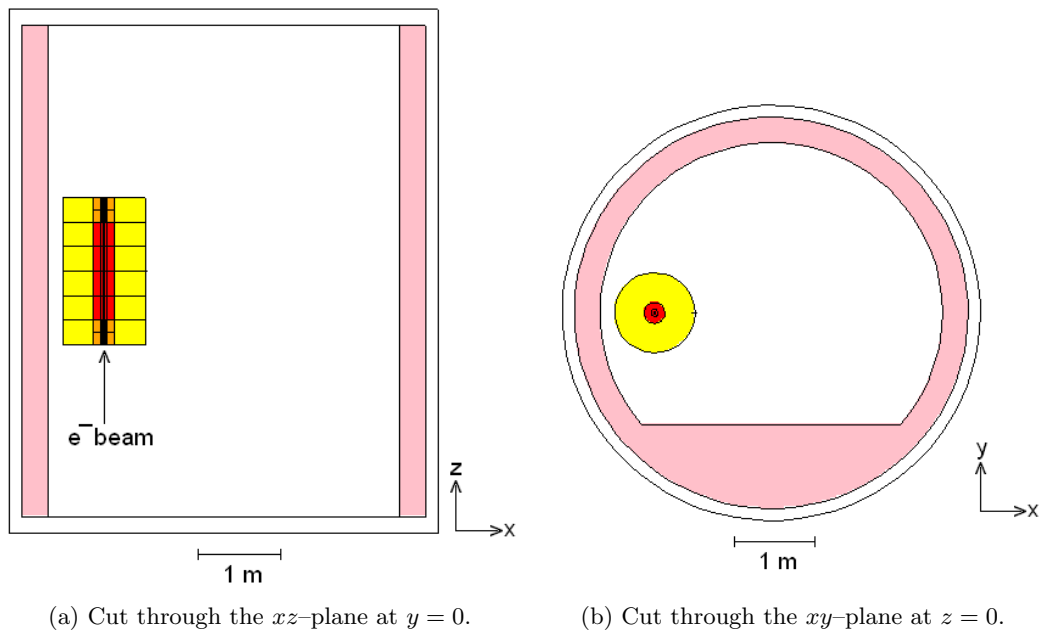


Figure 2.1.75: MCNPX input geometry to calculate neutron and photon dose rates for the M-type collimators. The center of the collimator is at $(x, y, z) = (0, 0, 0)$. The electron beam propagates in the $+z$ -direction. Yellow is iron, red is aluminum, orange is lead, and pink ordinary concrete.

Activation of collimators

Activation of collimators and collimator shielding materials is mostly due to neutrons produced in photonuclear reactions. Possible neutron reactions that can produce radioisotopes in collimator materials of interest are (n, γ) , $(n, 2n)$, $(n, {}^3\text{He})$, (n, α) and (n, d) reactions. The bulk of the collimator is made from aluminum, copper, and iron. Most of the radioisotopes produced have half-lives in the minute, hour, and day range. A few have half-lives in the 0.5-5 year range. Possible long-lived radio-isotopes that can be produced include ${}^{26}\text{Al}$, $T_{1/2} = 7.2 \times 10^5$ y, ${}^{54}\text{Mn}$, $T_{1/2} = 312$ y, and ${}^{63}\text{Ni}$, $T_{1/2} = 100$ y. The radio-nuclides decay by β^\pm emission and electron capture either to excited states followed by γ emission, or to the ground state. The thick iron shell used in both the protector and collimator designs to slow down energetic neutrons is also an effective shield against the radiations emitted by the decaying radionuclides produced in the inner $7X_M$ diameter cylinder.

Bremsstrahlung produced in the 25 m long undulator

A preliminary estimate of bremsstrahlung produced by residual gas in the 25 m long undulator was obtained as follows: A 25 m long column of air at atmospheric pressure, irradiated at one end by 5 GeV electrons, was contained in a 0.866" ID, 1.0" OD aluminum tube, surrounded by a 30 cm diameter, 52.5 m long evacuated space. This represents the inner 25 m long undulator space plus a 27.5 m beam line from the end of the undulator to the experimental hutch shielding wall (A more realistic calculation using a 25 m long 5 mm diameter residual gas column surrounded by NdFeB material will be carried out). At 1.0 nTorr, there is a very low probability of electrons interacting with the gas. Accordingly, the calculation was done at atmospheric pressure, and the results scaled linearly to 1 nTorr [64]. That is, the calculated contours have to be multiplied by $1.0 \times 10^{-9} \text{ Torr}/760 \text{ Torr} = 1.316 \times 10^{-12}$.

The cylindrically symmetric photon dose rate (rem/h)/(el/s) as a function of x (or y) perpendicular to the electron beam at 27.5 m downstream from the end of the 25 m long beam pipe containing air at 1 nTorr is shown in Fig. 2.1.76. For a peak value of 10^{-18} (rem/h)/(el/s), over a 1 cm diameter hole, 100 mA corresponds to a dose rate of 0.62 rem/h.

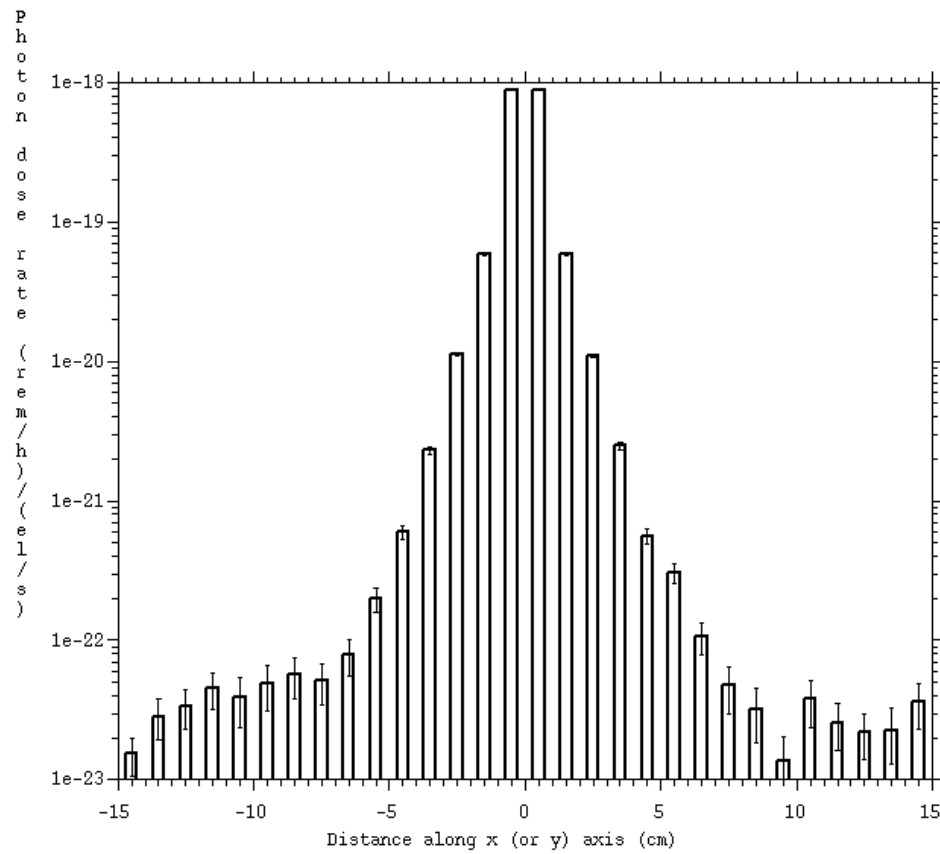


Figure 2.1.76: Photon dose rate (rem/h)/(el/s) as a function of x (or y) 27.5 m downstream from the end of the 25 m long undulator containing air at 1 nTorr

2.1.19 Ion effects

Residual gas in the beam pipe is ionized by the passage of the electron beam. The resulting positive ions can become trapped by the negative potential well of the electron beam. These trapped ions form a charged column along the beam path. This ion column can perturb the motion of the beam by exerting a nonlinear focusing force, and coupled oscillations between the column and the beam can blow-up the effective size of the beam.

Ion phenomena are routinely observed in storage rings, where they manifest as an increase in beam size along the bunch train. Ions are typically dealt with in a storage by using a clearing gap. A clearing gap is a periodic gap that allows accumulated ions to drift out of the beam path. Because of the energy-recovery mechanism in an ERL, a sufficiently long clearing gap is not easily produced [65], reduces the average current, and limits flexibility of the operation.

Other rings eliminate ions by clearing electrodes where their effectiveness as mitigating ion effects has been proven [66]. It has therefore been decided to employ ion-clearing electrodes approximately every 20 m along the electron-beam transport, based on simulations of the equilibrium ion density that is established between ion production by scattering and ion propagation toward clearing electrodes [67].

Section 2.2.4 describes the design for ion-clearing electrodes for the ERL. These counteract the production of ion beams, which are dominated by H₂ and have an ion build-up time on the order of several seconds. To overcome the steep potential of the ERL's ultra-low emittance beams, 1.9 kV across a 2.5 cm aperture is needed. To avoid component heating by image charges, those electrodes are designed to have very low impedances.

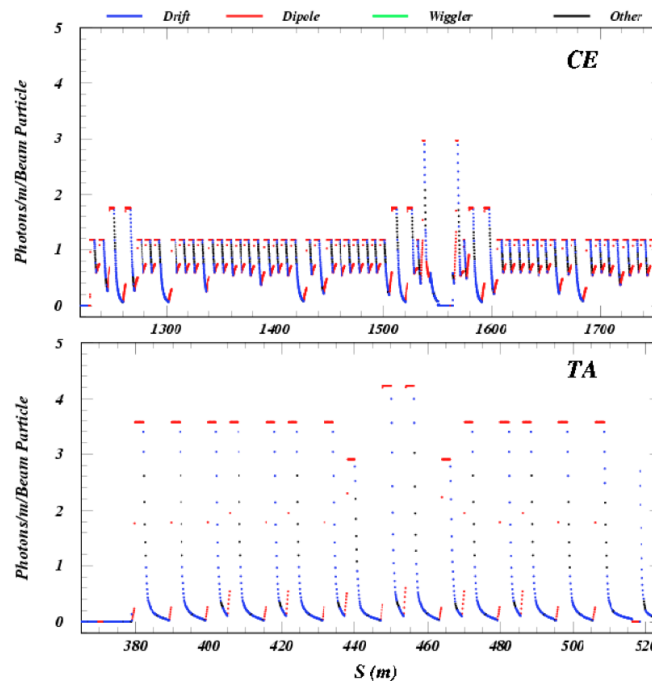


Figure 2.1.77: Synchrotron radiation patterns in the ERL sections CE and TA as calculated for the ERL 8.1 lattice using the Bmad SYNRAD utility.

2.1.20 Electron-cloud effects

The production of low-energy electron clouds via synchrotron-radiation-induced photoeffect on the vacuum chamber walls in synchrotrons has been under active study since the 1990's, when it was determined to be a limiting factor at KEKB [6].

Among various cloud-related instabilities are single-bunch head-tail instabilities, multibunch instabilities associated with the wakes of disturbed clouds, resonant effects relating vacuum chamber transit times and bunch spacing. In addition, the transverse cloud shape, density and time development can distort the linear optics via its space-charge field. While many of these effects are of concern primarily for positively-charged beams, since they attract the cloud electrons, intense clouds can build up in electron accelerators as well. In this section we summarize calculations of electron cloud development in the Cornell ERL, obtaining estimates of the equilibrium density, transverse shape, space-charge field gradients, and address the consequences of gaps in the cloud-repelling bunch train.

This study consists of two calculation steps. First, the ERL 8.1 lattice is analyzed with the SYNRAD utility in Bmad to determine the rate of photons from synchrotron radiation in the various beamline element types in each of the sections of the ERL. Second, the 2D particle-in-cell simulation code ECLOUD employs the beam parameters and photon rates determined in the first step to calculate the time development of the cloud in the ERL sections and element types in which the cloud effects are strongest.

Figure 2.1.77 shows the radiation pattern in 1-cm steps for the CE section, color-coding the radiation in the drift and dipole regions, as well as for the section with the highest av-

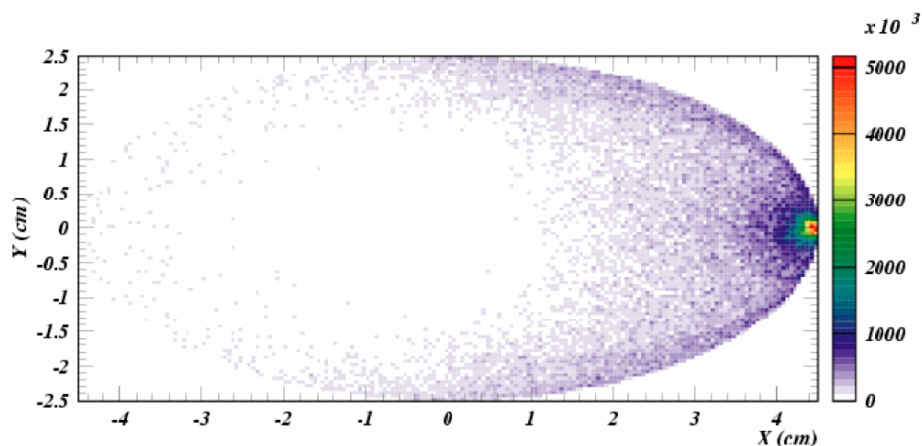


Figure 2.1.78: Snapshot of the cloud profile in a field-free region of the CE section two bunch spacings following the 150th bunch. The vacuum chamber surface is aluminum.

erage photon rate, TA. While the average photon rate is higher in the TA due to its smaller bending radius, the electron cloud simulation accounts for a large suppression due to the effectiveness of the antechamber in absorbing the direct synchrotron radiation and trapping the photoelectrons.

The input parameters for the ECLOUD calculation can be categorized in four types: numerical parameters, beam characteristics, photoelectron production, and the secondary yield model for cloud electrons. Many of the parameters used here have been developed in the context of the CESR Test Accelerator project (CesrTA) [68], for which measurements of coherent tune shifts were successfully modeled for electron and positron beam energies ranging from 1.9 to 5.3 GeV and bunch populations between 6.4×10^9 and 1.9×10^{10} [69, 70].

The secondary yield model is made up three contributions, varying with the energy and angle of the cloud electron incident on the beampipe wall. At low energy, the predominant production mechanism is an elastic reflection off the wall with an average charge yield factor of about 0.5. This value largely determines the cloud decay rate in the absence of beam and agrees well with the CesrTA tune shift measurements. The “true secondary” component is the main source of runaway cloud development, since its yield value peaks at 1.8 at an incident energy of 310 eV, so if such high incident energies are present, as can be caused by the beam kicks, exponential growth is possible. It can be generally stated that the beam kicks to be expected from the ERL bunch population are well below this threshold. These true secondaries are produced with only a few eV of energy, independent of the incident energy. Finally, the third contribution to the secondary yield is comprised of “rediffused” electrons, which can carry a substantial fraction of the incident energy, but with a charge yield of only 0.2, independent of the incident energy. These parameters for the secondary yield model were found to accurately reproduce the CesrTA (aluminum vacuum chamber) coherent tune shift measurements. The ECLOUD results were also thoroughly cross-checked using independent calculations with the POSINST software package.

For reasonable parameters, the electron-cloud buildup is simulated following the start of an electron beam. Figure 2.1.78 shows a snapshot of the cloud profile in the CE beampipe two

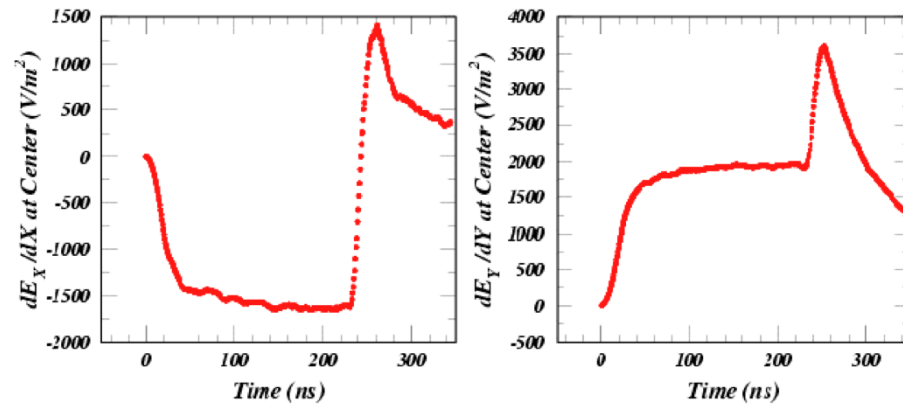


Figure 2.1.79: ECLLOUD calculations of the horizontal and vertical space-charge field gradients at the center of the vacuum chamber during the cloud buildup in the field-free regions of the CE section.

bunch spacings following the 150th filled bunch. The cloud model consists of 123k macroparticles each carrying 1.8×10^9 electrons. The buildup curve shows the cloud after production and decay have largely equilibrated. No relevant cloud density has reached the center of the beam pipe. This fact can also be seen in the field-gradient time dependence shown in Fig. 2.1.79 if one considers that Gauss's law for a charge free region requires that the horizontal and vertical field gradients must add to zero. Figure 2.1.79 shows that the increase in magnitude of the field gradients stops after about 50 ns at a value less than 2000 V/m^2 . The equivalent focusing strength of a quadrupole magnet is about $7 \times 10^{-6} \text{ T/m}$. Since the total length of the quadrupoles in the CE is 43.6 m, compared to the total length of field-free regions of 117 m, we can conclude that the relative distortion of the linear optics due to the electron cloud will not exceed 2×10^{-6} . In the case of a gap in the bunch train, the vertical field gradient will begin to increase, as shown in Fig. 2.1.79, but the cloud decay time of less than 100 ns will prevent any appreciable distortion of the linear optics. Figure 2.1.79 also shows that if there is a gap in the bunch train, the vertical field gradient will increase by about a factor of two as the cloud collapses, but will decay away over a time period of about 50 ns.

References

- [1] Tigner, M. *A Possible Apparatus for Electron Clashing-Beam Experiments*. Nuovo Cimento, **37**, pages 1228–1231 (1965).
- [2] Mayes, C. and G. Hoffstaetter. *Exact 1D model for coherent synchrotron radiation with shielding and bunch compression*. Phys. Rev. ST Accel. Beams, **12** (2), page 024401 (Feb 2009). doi:10.1103/PhysRevSTAB.12.024401.
- [3] Wiedemann, H. *Particle Accelerator Physics I*. Springer Verlag, Berlin, second edition (1999).
- [4] Sagan, D. *Bmad: A relativistic charged particle simulation library*. Nucl. Instrum. Methods Phys. Res., Sect. A, **558**, pages 356–359 (2006).
- [5] Bazarov, I. V., et al. *Benchmarking of 3D space charge codes using direct phase space measurements from photoemission high voltage dc gun*. Phys. Rev. ST AB, **11** (100703) (2008).
- [6] Bazarov, I. V., B. M. Dunham, and C. K. Sinclair. *Maximum Achievable Beam Brightness from Photoinjectors*. Phys. Rev. Lett., **102** (104801) (2009).
- [7] Bazarov, I. V., et al. *Thermal emittance and response time measurements of negative electron affinity photocathodes*. Journal of Applied Physics, **103** (5) (2008).
- [8] Carlsten, B. *New Photoelectric injector design for the Los Alamos National Laboratory XUV FEL accelerator*. Nucl. Instr. and Meth. A, **285** (1-2), pages 313–319 (1989).
- [9] Flottman, K. *ASTRA: a space charge tracking algorithm*. DESY (2000).
- [10] Bazarov, I. V. and C. K. Sinclair. *Multivariate optimization of a high brightness dc gun photoinjector*. Phys. Rev. ST AB, **8** (2005).
- [11] Slade, P. G. *The vacuum interrupter: theory, design, and application*. CRC Press (2008).
- [12] Bazarov, I. V., et al. *Efficient temporal shaping of electron distribution for high-brightness photoemission electron guns*. Phys. Rev. ST AB, **11** (4) (2008).
- [13] Karkare, S. and I. Bazarov. *Effect of nano-scale surface roughness on transverse energy spread from GaAs photocathodes*. Applied Physics Letters, **98** (2011).
- [14] Litvinenko, V., R. Hajima, and D. Kayran. *Reduction of field emission dark current for high-field gradient electron gun by using a molybdenum cathode and titanium anode*. Nucl. Instr. and Meth. A, **557** (1), pages 165–175 (2006).
- [15] Bazarov, I. and T. Miyajima. *Calculation of Coherent Synchrotron Radiation in General Particle Tracer*. In *Eleventh European Particle Accelerator Conference, EPAC08*, pages 118–120. EPAC08, Genoa, Italy (2008).
- [16] Venturini, M. and M. Reiser. *rms Envelope Equations in the Presence of Space Charge and Dispersion*. Phys. Rev. Lett., **81** (1), pages 96–99 (1998).

-
- [17] Miyajima, T. and I. V. Bazarov. *Simulation study of Cornell L0 beamline*. Report ERL 11-02, Cornell (2011).
- [18] Bazarov, I. and G. Hoffstaetter. *Lattice options for a 5 GeV light source at Cornell*. In *PAC03*. Portland/OR (2003).
- [19] Bazarov, I., G. Krafft, and L. Merminga. *Linac Optics for Energy Recovery Linac*. In *PAC01*. Chicago/IL (2001).
- [20] Douglas, D. *Design Considerations for Recirculating and Energy Recovering Linacs*. Report JL-TN 00-0027, Jefferson Lab (2000).
- [21] Hoffstaetter, G. H. and Y. H. Lau. *Compensation of wakefield-driven energy spread in energy recovery linacs*. PRST, **11**, page 070701 (2008).
- [22] Sagan, D., *et al.* *Extended one-dimensional method for coherent synchrotron radiation including shielding*. Phys. Rev. ST Accel. Beams, **12** (4), page 040703 (Apr 2009). doi: 10.1103/PhysRevSTAB.12.040703.
- [23] Meseck, A., *et al.* *FELs as x-ray sources in ERL facilities*. In *Proceedings of PAC11* (2011).
- [24] Colella, R. and A. Luccio. Opt. Commun., **50**, page 41 (1984).
- [25] *A proposal for an x-ray free-electron laser oscillator with and energy recovery linac*. Phys. Rev. Lett., **100**, page 244802 (2008).
- [26] *Tunable optical cavity for an x-ray free-electron-laser oscillator*. Phys. Rev. ST Accel. Beams, **12**, page 030703 (2009).
- [27] Lindberg, R. R. and K.-J. Kim. *Mode growth and competition in the x-ray free-electron laser oscillator start-up from noise*. Phys. Rev. ST Accel. Beams, **12**, page 070702 (2009).
- [28] Billing, M. *et al.* *Effect of wakefields in an energy recovery linac*. In *Particle Accelerator Conference PAC2009, Vancouver, Canada* (2009).
- [29] Chin, H. *User's Guide for ABCI Version 9.4*. Technical Report KEK Report 2005-06, KEK (2005).
- [30] Novokhatski, S. *The Computer Code NOVO for the Calculation of Wake Potentials of Very Short ultra-relativistic bunches*. Technical Report SLAC-PUB-11556, SLAC (2005).
- [31] MAFIA Collaboration. *MAFIA manual*. Technical report, CST GmbH, Darmstadt (1997).
- [32] Novokhaski, A. *et al.* *Single Bunch Energy Spread in the TESLA Cryomodule*. Technical Report DEST-TESLA-1999-16, DESY (1999).
- [33] Schwinger, J. *On Radiation by Electrons in a Betatron*. In K. A. Milton, editor, *A Quantum Legacy: Seminal Papers of Julian Schwinger*, pages 307–331. World Scientific, Singapore (1945). Also in Report LBNL-39088.

- [34] Agoh, T. and K. Yokoya. *Calculation of coherent synchrotron radiation using mesh*. Phys. Rev. ST Accel. Beams, **7** (5), page 054403 (May 2004). doi:10.1103/PhysRevSTAB.7.054403.
- [35] Mayes, C. *Energy Recovery Linear Accelerator Lattice Design & Coherent Synchrotron Radiation*. Ph.D. thesis, Cornell University, Ithaca, NY (May 2009). <http://hdl.handle.net/1813/13477>.
- [36] Hoffstaetter, G., M. Billing, and Y. Lau. *Wake-field compensation in Energy Recovery Linacs*. In *Proceedings EPAC08*. Genoa/IT (2008).
- [37] Singh, O. and G. Decker. *Beam Stability at the Advanced Photon Source*. In *Proceedings of PAC05, Knoxville* (2005).
- [38] Zhang, L., L. Farvacque, *et al.* *Electron Beam Stabilization Experiences at the ESRF*. Presentation, Advanced ICFA Beam Dynamics Workshop on Nanometre-Size Colliding Beams, Lausanne (2002).
- [39] Bulfone, D., R. D. Monte, *et al.* *Status of the ELETTRA Global Orbit Feedback Project*. In *Proceedings of EPAC06*. Edinburgh (2006).
- [40] Tanaka, H., H. Aoyagi, *et al.* *Beam Orbit Stabilization at the SPring-8 Storage Ring*. In *Proceedings of the 7th International Workshop on Accelerator Alignment*. SPring-8 (2002).
- [41] Streun, A., M. Boege, *et al.* *Beam Stability and Dynamic Alignment at SLS*. In *SSILS01*. Shanghai (2001).
- [42] Boege, M., B. Keil, *et al.* *Orbit Stability at the SLS*. Technical report (2003). PSI Scientific Report 2003, Vol. VI.
- [43] Schilcher, T., *et al.* *Global Orbit Feedback System for the SLS Storage Ring*. In *Proceedings of ICALEPCS99*. Trieste (1999).
- [44] Chao, Y.-C. and V. Mertens. *Analysis and Optimisation of Orbit Correction Configurations Using Generalised Response Matrices and its Application to the LHC Injection Transfer Lines TI 2 and TI 8*. Technical report (2001). LHC Project Report 470.
- [45] Song, C. and G. Hoffstaetter. *Magnetic Field Error Sensitivity in an Energy Recovery Linac*. Technical report, Cornell (2007). Report ERL-07-03.
- [46] Hoffstaetter, G. H. and I. Bazarov. *Beam-Breakup Instability Theory for Energy Recovery Linacs*. PRST, **7**, page 54401 (2004).
- [47] Hoffstaetter, G., I. Bazarov, and C. Song. *Recirculating Beam-Breakup Thresholds for Polarized Higher-Order Modes with Optical Coupling*. Phys. Rev. ST-AB, **10** (044401) (2007).
- [48] Crittenden, J. *Recent Progress on Beam-Breakup Calculation for the Cornell X-Ray ERL*. In *Proceedings of ERL09*. Ithaca, NY (2009).

-
- [49] Song, C. and G. Hoffstaetter. *Cornell Report ERL-07-10*. Technical report, Cornell (2007).
- [50] Song, C. and G. Hoffstaetter. *Cornell Report ERL-06-04*. Technical report, Cornell (2007).
- [51] Pelowitz, D. B., *et al.* *MCNPX 2.7.D Extensions*. Technical Report LA-UR-10-07031, Los Alamos National Laboratory, Los Alamos National Laboratory, Los Alamos, NM (October 2010).
- [52] Kostroun, V. *ERL Collimator Design*. CLASSE Technical Report ERL-RN-11-02, Cornell University (2011). In Preparation.
- [53] Piwinski, A. *The Touschek effect in strong focusing storage rings*. Technical Report DESY 98-179, DESY (1998).
- [54] Hoffsaetter, G. and M. Ehrlichman. *Touschek Losses in Linear Accelerators* (2011). In preparation.
- [55] Xiao, A. and M. Borland. *Touschek effect calculation and its application to a transport line*. In *twenty-second Particle Accelerator Conference*, pages 3453–3455. Albuquerque, New Mexico (2007).
- [56] Temnykh, A. B., M. P. Ehrlichman, and G. Hoffstaetter. *Beam losses due to intra-beam and residual gas scattering for Cornell’s energy recovery linacs*. In *eleventh European Particle Accelerator Conference, EPAC’08*, pages 214–216. Genoa, Italy (2008).
- [57] Bizek, H. M. *Some results of the Advanced Photon Source beam lifetime studies*. In *Proceedings of the 1997 Particle Accelerator Conference*, pages 1493–1495. Vancouver, B.C., Canada (1997).
- [58] Spencer, M., *et al.* *Lifetime contribution measurements at the Australian synchrotron*. In *twenty-second Particle Accelerator Conference*, pages 914–916. Albuquerque, New Mexico (2007).
- [59] Chao, A. W. and M. Tigner. *Handbook of Accelerator Physics and Engineering (3rd printing)* (2006).
- [60] Nakamura, K. and P. D. Group). *Review of Particle Physics*. Journal of Physics G: Nuclear and Particle Physics, **37**, page 075021 (2010). Chapter 27, Passage of particles through matter.
- [61] *Radiation Protection for Particle Accelerator Facilities*, volume NCRP Report No. 144. National Council on Radiation Protection and Measurements, National Council on Radiation Protection and Measurements, 7910 Woodmont Avenue, Suite 400/Bethesda, Maryland 20814-3095, 2005 edition (2003).
- [62] Neal, R. B., editor. *The Stanford Two-Mile Accelerator*. Benjamin, New York (1968). Chapter 26 Shielding and Radiation by H. De Staebler, T. M. Jenkins and W.R. Nelson.

- [63] Temnykh, A. B. *Measurement of NdFeB permanent magnets demagnetization induced by high energy electron radiation*. Nucl. Instrum. Methods Phys. Res., Sect. A, **587**, pages 13–19 (2008).
- [64] Ferrari, A., M. Pelliccioni, and P. Sala. *Estimation of fluence rate and absorbed dose rate due to gas bremsstrahlung from electron storage rings*. Nucl. Instr. and Meth. B, **83**, pages 518 – 524 (1993).
- [65] Hoffstaetter, G. H. and M. Liepe. *Ion clearing in an ERL*. Nuclear Instruments and Methods in Physics Research Section A: Accelerators, Spectrometers, Detectors and Associated Equipment, **557** (1), pages 205 – 212 (2006). ISSN 0168-9002. doi: DOI:10.1016/j.nima.2005.10.069. Energy Recovering Linacs 2005 - Proceedings of the 32nd Advanced ICFA Beam Dynamics Workshop on Energy Recovering Linacs.
- [66] Feikes, J. *et al.* *Commissioning and operation of the metrology light source*. In *Eleventh European Particle Accelerator Conference, EPAC08*, pages 2010–2012. EPAC08, Genoa, Italy (2008).
- [67] Hoffstaetter, G. H. and C. Spethmann. *Equilibrium ion distribution in the presence of clearing electrodes and its influence on electron dynamics*. Phys. Rev. ST Accel. Beams, **11** (1), page 014001 (Jan 2008). doi:10.1103/PhysRevSTAB.11.014001.
- [68] Palmer, M. *et al.* *The Conversion and Operation of the Cornell Electron Storage Ring as a Test Accelerator for Damping Rings Research and Development*. In *Proceedings of PAC09* (2009).
- [69] Crittenden, J. A. *et al.* *Studies of the Effects of Electron Cloud Formation on Beam Dynamics at CesrTA*. In *Proceedings of PAC09* (2009).
- [70] Calvey, J. R. *et al.* *Electron Cloud Modeling Considerations at the CESR Test Accelerator*. In *Proceedings of PAC09* (2009).